

**UCC Library and UCC researchers have made this item openly available.  
Please [let us know](#) how this has helped you. Thanks!**

<b>Title</b>	Laser-induced plasmas in air for pulsed broadband cavity-enhanced absorption spectroscopy
<b>Author(s)</b>	Keary, Bryan P.
<b>Publication date</b>	2020-01-07
<b>Original citation</b>	Keary, B. P. 2020. Laser-induced plasmas in air for pulsed broadband cavity-enhanced absorption spectroscopy. PhD Thesis, University College Cork.
<b>Type of publication</b>	Doctoral thesis
<b>Rights</b>	© 2020, Bryan P. Keary. <a href="https://creativecommons.org/licenses/by-nc-nd/4.0/">https://creativecommons.org/licenses/by-nc-nd/4.0/</a>
<b>Item downloaded from</b>	<a href="http://hdl.handle.net/10468/9867">http://hdl.handle.net/10468/9867</a>

Downloaded on 2021-11-27T14:24:17Z



# UCC

**University College Cork, Ireland**  
Coláiste na hOllscoile Corcaigh

NATIONAL UNIVERSITY OF IRELAND, CORK



UCC

University College Cork, Ireland  
Coláiste na hOllscoile Corcaigh

**Laser-Induced Plasmas in Air for  
Pulsed Broadband  
Cavity-Enhanced Absorption  
Spectroscopy**

by

Bryan Keary

A thesis submitted in partial fulfillment for the degree of  
Doctor of Philosophy

in the Department of Physics

Supervisor: Prof. Albert A. Ruth

Head of Department: Prof. John G. McInerney

2020

# Declaration of Authorship

This is to certify that the work I am submitting is my own and has not been submitted for another degree, either at University College Cork or elsewhere. All external references and sources are clearly acknowledged and identified within the contents. I have read and understood the regulations of University College Cork concerning plagiarism.

Signed: \_\_\_\_\_

Date: \_\_\_\_\_

External Examiner

Prof. Harold Linnartz – University of Leiden, The Netherlands

Internal Examiner

Dr. Dean Venables – University College Cork, Ireland

# *Abstract*

A pulsed laser-induced plasma (LIP) was generated in ambient air inside a high-finesse *near-concentric* optical cavity. The broadband optical plasma emission was successfully sustained within the cavity and the light leaking from the cavity was used to measure broadband absorption spectra of gaseous azulene through (i) time-dependent cavity ring-down (CRDS), and (ii) intensity-dependent incoherent broadband cavity-enhanced absorption spectroscopy (IBBCEAS) methodologies. Based on the broadband ring-down time of light within the cavity, cavity mirror reflectivities may be calibrated *in situ*, thus facilitating measurements of absolute absorption coefficients with the intensity-dependent (IBBCEAS) approach. Each of the two spectroscopic approaches are compared in terms of their overall performance and suitability to the experimental requirements.

The IBBCEAS approach was found to possess numerous advantages over the CRDS approach in terms of measurement speed, and achievable signal-to-noise ratios and minimum detectable absorption coefficients. However, the IBBCEAS approach is limited by the presence of an artificial offset in the measured absorption that arises due to the absorption of light occurring between LIP formation and the commencement of data collection. This delay prior to data collection is necessitated by the non-Lambert-Beer conditions during plasma equilibration. For the given experimental conditions, the cavity output typically takes  $\sim 1.5 \mu\text{s}$  to begin mono-exponential decay.

The time-dependence of the cavity output intensity was also investigated. Light propagating within the cavity is subject to direct absorption by the intra-cavity LIP, and a lensing effect ( $f \approx -3.1 \text{ cm}$ ) by the LIP as a result of a localised non-linear refractive index change induced by the high temperatures and strong electric fields associated with the LIP. This time-dependence was observed to be dependent on both the mirror separation and the pulse duration of the LIP formation laser. These dependencies come about as a consequence of the LIP lensing temporarily affecting both the cavity stability and the imaging of the light that is output from the cavity, with both of these aspects being dependent on the cavity geometry. In the case of fs-lasers, the increased pulse power density expectedly yields a more significant lensing effect when compared to LIP formation with ns-pulsed lasers.

# *Acknowledgements*

First of all, I have to thank my family for their support over the years, my parents Maxine and Tom, my siblings Elaine, David, and, of course, Deborah who provided extra motivation through the years thanks to our healthy “sibling rivalry”.

Special thanks to Hayret for her unwavering support throughout this decidedly protracted PhD, the book recommendations, being a travel companion, and of course being the light at the end of this thesis-writing tunnel.

I have to thank my fellow members of the Laser Spectroscopy Group - Karen, Satheesh, Krishna, Marc, Hemanth, and Stephen for their help and the fun we had over the last 5 years.

Thanks to all of the other physics postgraduate students - Danny, Anthony, Mark, Joe, Michael, Owen, Simon, Seb, and Declan, for the lunch breaks and all of the after work activities.

Finally, I have to thank my supervisor Andy. None of this would have been possible without his support and optimism.

Bryan Keary  
University College Cork  
October 2019

*“Anything worth dying for ... is certainly worth living for.”*

- Joseph Heller, *Catch-22*, 1961

# Contents

<b>Declaration of Authorship</b>	<b>i</b>
<b>Abstract</b>	<b>ii</b>
<b>Acknowledgements</b>	<b>iii</b>
<b>List of Abbreviations</b>	<b>viii</b>
<b>List of Figures</b>	<b>ix</b>
<b>List of Tables</b>	<b>xvi</b>
<b>1 Introduction</b>	<b>1</b>
1.1 Cavity ring-down spectroscopy . . . . .	3
1.1.1 Experimental principle . . . . .	4
1.2 Incoherent broadband cavity-enhanced absorption spectroscopy . . . . .	6
1.2.1 Experimental principle . . . . .	7
1.2.2 Performance considerations . . . . .	9
1.3 Laser-induced breakdown . . . . .	10
1.3.1 Experimental principle . . . . .	11
1.4 High-finesse optical cavities . . . . .	14
1.4.1 Optical cavity stability . . . . .	14
1.5 Cavity-enhanced absorption spectroscopy with laser-induced plasmas . . . . .	17
1.5.1 Experimental principle . . . . .	19
1.5.2 Influence of laser-induced plasmas on the propagation of light in optical cavities . . . . .	21
1.6 Thesis objectives and outline . . . . .	22
1.6.1 Thesis objectives . . . . .	22
1.6.2 Thesis outline . . . . .	23

<b>2</b>	<b>Experimental</b>	<b>25</b>
2.1	Experimental setup . . . . .	25
2.1.1	Light sources, detection system, and optics . . . . .	26
2.2	Cavity-enhanced absorption spectroscopy with laser-induced plasmas	31
2.2.1	Broadband cavity ring-down spectroscopy . . . . .	31
2.2.2	Incoherent broadband cavity-enhanced absorption spectroscopy	34
2.3	Laser-induced plasma formation . . . . .	35
2.3.1	Laser-induced breakdown process . . . . .	36
2.3.2	Energy-dependence of the LIP emission intensity . . . . .	39
2.3.3	Laser-induced plasma emission stability . . . . .	43
2.4	LIP-induced non-linear refractive index change . . . . .	45
2.4.1	Experimental setup . . . . .	46
2.5	Conclusion . . . . .	47
<b>3</b>	<b>Spectral properties of laser-induced plasmas</b>	<b>49</b>
3.1	LIP spectral properties . . . . .	50
3.1.1	Time-resolved LIP emission spectra . . . . .	50
3.1.2	Temporal evolution of the LIP broadband continuum emission	52
3.2	Determination of the LIP temperature . . . . .	56
3.2.1	Boltzmann analysis of the LIP temperature . . . . .	57
3.2.2	Temporal evolution of the LIP temperature . . . . .	58
3.3	Conclusion . . . . .	65
<b>4</b>	<b>Cavity-enhanced absorption spectroscopy with intra-cavity LIPs</b>	<b>66</b>
4.1	Azulene . . . . .	69
4.1.1	Preparation of the gaseous azulene samples . . . . .	69
4.2	Cavity output and reflectivity calibration . . . . .	71
4.2.1	Time-dependence of the cavity output from a near-concentric cavity . . . . .	71
4.2.2	<i>In situ</i> cavity mirror reflectivity measurement . . . . .	72
4.3	Broadband CRDS with LIPs as intra-cavity light sources . . . . .	75
4.3.1	Broadband CRDS of gaseous azulene . . . . .	75
4.3.2	CRDS baseline and SNR . . . . .	77
4.4	IBBCEAS with LIPs as intra-cavity light sources . . . . .	80
4.4.1	IBBCEAS of gaseous azulene . . . . .	80
4.4.2	IBBCEAS baseline and SNR . . . . .	81
4.5	Correction to measured IBBCEAS spectra . . . . .	83
4.5.1	Origin of the offset in IBBCEAS measurements . . . . .	84
4.5.2	Procedure for correcting IBBCEAS spectra . . . . .	87
4.6	Comparison between CRDS and IBBCEAS approaches . . . . .	91
4.6.1	Estimation of azulene mixing ratio and detection limits . . . . .	93
4.7	Conclusion . . . . .	96
<b>5</b>	<b>Influence of intra-cavity LIPs on the cavity output intensity</b>	<b>98</b>
5.1	Summary of observed cavity outputs . . . . .	100



5.2	Demonstration of the lensing effect induced by LIPs . . . . .	103
5.3	Effects of the LIP on the cavity output intensity . . . . .	108
5.3.1	Imaging of the cavity output . . . . .	108
5.3.2	Influence of the LIP on optical cavity stability . . . . .	111
5.4	Time-dependence of the cavity output intensity . . . . .	113
5.4.1	Cavity length dependence . . . . .	114
5.4.2	Time at which maxima occur in cavity output . . . . .	116
5.4.3	Difference in time-dependence between fs-, and ns-generated LIPs . . . . .	117
5.5	Conclusion . . . . .	119
<b>6</b>	<b>Summary and conclusion</b>	<b>121</b>
6.1	Summary . . . . .	121
6.2	Conclusion . . . . .	125

<b>Bibliography</b>	<b>127</b>
---------------------	------------

# List of Abbreviations

<b>BB</b>	Broadband
<b>CCD</b>	Charge-coupled device
<b>CEAS</b>	Cavity-enhanced absorption spectroscopy
<b>CESAS</b>	Cavity-enhanced self-absorption spectroscopy
<b>CRDS</b>	Cavity ring-down spectroscopy
<b>CW</b>	Continuous wave
<b>DDG</b>	Digital delay generator
<b>FWHM</b>	Full width at half maximum
<b>HR</b>	High reflectivity
<b>IBBCEAS</b>	Incoherent broadband cavity-enhanced absorption spectroscopy
<b>iCCD</b>	Intensified charge-coupled device
<b>ICLAS</b>	Intra-cavity laser absorption spectroscopy
<b>ICOS</b>	Integrated cavity output spectroscopy
<b>KDP</b>	Potassium dihydrogen phosphate
<b>LIBS</b>	Laser-induced breakdown spectroscopy
<b>LIP</b>	Laser-induced plasma
<b>LPM</b>	Litres per minute
<b>SNR</b>	Signal-to-noise ratio
<b>TEM</b>	Transverse electromagnetic
<b>TTL</b>	Transistor-transistor logic

# List of Figures

1.1	Illustration of the measurement principle of CRDS. The light leaking from the cavity with an absorbing species present (blue) decays at a faster rate than when there is no absorbing species present (red). $\tau$ and $\tau_0$ represent the exponential decay constants for each of these situations, respectively. . . . .	5
1.2	Experimental principle of IBBCEAS for a cavity of length $L$ , comprised of mirrors with a reflectivity $R(\lambda)$ . $I_0(\lambda)$ is the cavity output without an absorbing sample present in the cavity, while $I(\lambda)$ represents the measured cavity output <i>with</i> an absorbing sample present in the cavity. . . . .	8
1.3	Representative HR cavity mirror transmittance curve for a mirror with a nominal (manufacturer stated) on-axis reflectivity of $R = 0.9995$ , centred at 675 nm, measured with a spectrophotometer (Perkin Elmer Lambda 1050). Blue dashed lines indicate the HR range of the mirror. Inset: Zoomed in view of the HR range. . . . .	9
1.4	LIBS spectra recorded at three different delay times for an LIP formed in lab air, showing how the plasma emission changes with time. Note the different vertical scales for each spectrum. The spectra were recorded with a 50 ns integration window, accumulated over 100 LIP excitations. The red dashed lines indicate some of the emission lines from singly ionised nitrogen and oxygen, while the blue dashed lines indicate emission from neutral atoms. FWHM values for select lines are indicated on the plot. The dip in the spectra around 532 nm is due to a notch filter to protect the detection system from stray light from the laser pulse used for plasma formation.	13
1.5	Stability diagram for optical resonators with spherical mirrors. The shaded areas indicate stable cavity configurations, determined from the $g$ -parameters (Eqs. 1.7a and 1.7b). The dashed red line signifies symmetric cavity geometries, with three special cases highlighted: Concentric $(-1, -1)$ , confocal $(0, 0)$ , and plane-parallel $(1, 1)$ . . . . .	16
1.6	Ray-trace diagrams showing light propagation within concentric (upper) and confocal (lower) optical cavities. $r$ represents the cavity mirror radius of curvature, which is the same for both cavity mirrors in this example (i.e. a symmetric resonator). . . . .	17

---

2.1	Typical experimental setup for cavity based measurements. The Nd:YAG laser produces high power pulses which are focused by $L_1$ to the centre of the cavity formed by $M_1$ and $M_2$ , to produce an LIP. $M_2$ is mounted on a translational stage which allows the cavity length to be varied ( $\pm 4$ cm). A He-Ne laser is used for alignment of the optical cavity. $L_2$ : Achromatic lens to image the cavity output onto the aperture of a fibre bundle, with the notch filter, F, preventing any laser stray light from entering the detection system. BS: Beamsplitter to monitor laser pulse energy with an energy meter (EM) and oscilloscope ( $OSC_2$ ). SG: Signal generator to trigger the laser and, via a digital delay generator (DDG), the iCCD. The laser output is monitored with a photodiode (PD) and oscilloscope ( $OSC_1$ ). . . . .	27
2.2	<b>(a)</b> Cavity output spectrum measured for a number of delay times after plasma formation. Each spectrum corresponds to a $0.5 \mu\text{s}$ gate window accumulated over 500 plasma pulses, yielding a total integration time of $250 \mu\text{s}$ per spectrum. <b>(b)</b> Relative cavity output intensities at 631 nm (see dashed purple line in (a)). Ring-down times as a function of wavelength are determined from an appropriate fit to the exponentially decaying cavity output intensity. . . . .	33
2.3	<b>(a)</b> Cavity output spectrum measured by integrating over the cavity output decay from $1.5 - 10.5 \mu\text{s}$ after plasma formation, accumulated over 500 plasma pulses, yielding a total integration time of 4.5 ms. <b>(b)</b> Typical time-dependent cavity output intensity at an arbitrary wavelength. The shading indicates the time range over which the cavity output intensity is integrated to produce the spectrum shown in (a). . . . .	35
2.4	Illustration of the expected laser pulse intensity before (grey) and after (red) LIP formation, for a pulse with an energy far in excess of the breakdown threshold in air. Breakdown occurs when the laser intensity surpasses the threshold $I_{BD}$ , after which point the laser energy is absorbed by the LIP. . . . .	38
2.5	Energy dependent relative LIP emission spectra in air shown immediately after plasma formation (upper plot), and after a delay of 100 ns (lower plot). Both plots are normalised to the same vertical scale. The dip at $\sim 535$ nm is due to a notch filter used to protect the detection system from exposure to stray light from the plasma formation laser. . . . .	40
2.6	Relationship between the LIP emission intensity and the laser pulse energy, measured immediately after LIP formation. The LIP emission intensity is normalised to 100 at a pulse energy of 100 mJ. Red: Linear regression fit to the measured data points. . . . .	41
2.7	Relationship between the LIP emission intensity and the laser pulse energy, measured 100 ns after LIP formation. The LIP emission intensity is normalised to the same scale as in Fig. 2.6. Red: Linear regression fit to the measured data points. . . . .	41

---

2.8	Calculated exponential decay constant over the first 100 ns after LIP formation, as a function of laser pulse energy, determined from a combination of the two linear relationships presented in Fig. 2.6 and Fig. 2.7. . . . .	42
2.9	Relative LIP emission intensity measured for 100 consecutive plasma excitations for a laser pulse energy of 55 mJ, showing the LIP emission jitter around the mean, which is normalised to 100 (red line). The blue lines indicate $\pm 1$ standard deviation ( $\sigma$ ) around the mean. . . . .	43
2.10	Allan variance plot for the LIP emission intensity. $N_{\text{LIP}}$ represents the number of sequential plasma excitations over which the measured intensity has been accumulated. . . . .	44
2.11	Relative LIP emission intensity over time, from the point at which the laser is powered on, recorded immediately after plasma formation. The red line indicates the general upward trend in the LIP emission intensity from $\sim 140$ min onwards. . . . .	45
2.12	Schematic of experimental setup used to investigate the non-linear refractive index effects of the LIP. A probe beam from a He-Ne laser is focused through the LIP (generated as described above) by the lens $L_2$ ( $f = 3$ cm) such that the lens-plasma distance, $d_{\text{LP}}$ is less than the focal length, $f$ , of the lens. The transmitted probe beam is imaged onto a $200 \mu\text{m}$ pinhole, $P_1$ , and the time-varying intensity through the pinhole is monitored with the spectrometer and iCCD previously described. . . . .	47
3.1	<b>(a)</b> LIP emission spectrum shown in steps of 50 ns, from 0 to 200 ns after plasma formation. The dip at $\sim 535$ nm is due to a notch filter to protect the detection system from stray laser light. <b>(b)</b> Blue: Broadband LIP emission decay lifetime determined from a mono-exponential fit to the decaying spectra shown in (a) above. Red: $r^2$ -values for the mono-exponential fit. . . . .	51
3.2	<b>(a)</b> LIP emission spectrum measured for delay times of 750 ns, 1000 ns, and 1250 ns after plasma formation. The dip at $\sim 535$ nm is due to a notch filter used to protect the detection system from stray laser light. <b>(b)</b> Blue: Broadband LIP emission decay lifetime determined from a mono-exponential fit to the spectra shown above. Red: $r^2$ -values for the mono-exponential fit. . . . .	53
3.3	Semi-logarithmic plot of the relative LIP emission intensity from 0 – 1750 ns after plasma formation, measured at a wavelength of 631 nm. The blue and red lines indicate the time regions which were used to determine the LIP emission decay constants shown in Fig. 3.1 and Fig. 3.2, respectively. . . . .	53
3.4	Blackbody emission spectra, calculated from Eq. 3.1, for $T = 51300$ K and $34750$ K, which correspond to radiation temperatures 50 ns and 200 ns after plasma formation, respectively. The inset shows an expanded view of the region corresponding to the spectral range of the detector used for CEAS measurements, with the blue trace representing the ratio between the two spectra. . . . .	55

---

3.5	Red: Exponential decay lifetime between the two simulated black-body emission spectra shown in Fig. 3.4. Black: Decay lifetime of the measured LIP emission spectra showing the relative increase in the lifetime across the spectral range. To facilitate a comparison of the spectral dependence, the black spectrum has been normalised and scaled so that both spectra are equal at a wavelength of 610 nm.	56
3.6	LIP emission spectrum 150 ns after plasma formation, before (black) and after (blue) subtraction of the broadband continuum background (red-dashed). The numbers indicate the positions of the singly ionised nitrogen (black), and neutral oxygen (red), emission lines used to determine the plasma temperature. The assignments of these lines are listed in Tables 3.1 and 3.2. The green $\times$ indicates an example of an emission band that produces an erroneous area value when integrated due to a high density of O I emission lines.	60
3.7	Example Boltzmann plot for singly ionised (NII) nitrogen lines, measured 150 ns after LIP formation. The numbers indicate the identified emission line, according to Table 3.1. The green $\times$ is an obvious outlier corresponding to the emission peak at $\sim 444$ nm. A linear regression fit to the points (red line) yielded a plasma temperature of $38500 \pm 5000$ K.	62
3.8	Measured LIP temperature up to 1250 ns after LIP formation, determined from the Boltzmann plot method. For delays up to 450 ns the temperature is determined from singly ionised nitrogen (N II) lines, for delays of 500 – 750 ns a combination of N II and neutral oxygen (O I) lines are used. Temperatures for longer delay times are determined using only O I lines. Error bars were determined from the error in the slope of the Boltzmann plot. The green trace shows an exponential fit to the temperature from 50 – 1250 ns, with a decay constant of $440 \pm 45$ ns. Inset: Measured temperature at a delay time of 100 ns for a number of different laser pulse energies showing the weak correlation between the pulse energy and the LIP temperature. Blue trace: $T \propto E^{0.18}$ fit to the data points shown.	64
3.9	Temporal evolution of the linewidth (FWHM) of the N II emission line at 500.5 nm (line 2 in Fig. 3.6) after plasma formation. Significantly broadened lines at shorter delay times after plasma formation may contribute to increased errors due to overlapping emission lines.	64
4.1	Illustration of the typical time-dependence of the confocal cavity output observed in Ref. [6]. The blue shading indicates the portion of the cavity output which was accumulated for IBBCEAS measurements.	67
4.2	Chemical structure of azulene ( $C_{10}H_8$ ).	70

---

4.3	Semi-logarithmic plot of the measured cavity output intensity for a laser-induced plasma at the centre of a 79.3 cm cavity filled with air, measured at $\lambda = 631$ nm. The cavity output intensity was accumulated over 500 plasma pulses with a gate duration of 500 ns, giving a total integration time of 250 $\mu$ s for each data point. After the initial factor of $\sim 7$ decrease in intensity over the first 1.5 $\mu$ s, mono-exponential decay behaviour is observed with a corresponding ring-down time of 4.24 $\mu$ s. Red trace: Linear regression fit to the data points shown. . . . .	72
4.4	Black trace: Effective mirror reflectivity (left axis) calculated from the wavelength-dependent ring-down time of light leaking from the cavity (right-axis). Red trace: Fourth-order polynomial fit to the measured reflectivity spectrum. . . . .	73
4.5	Measured effective mirror reflectivity (black) shown with the coefficient of determination (red) of a mono-exponential fit to the data, indicating the decrease in fit quality around the spectral regions which exhibit long-lived emission lines. . . . .	74
4.6	Red trace: Broadband CRDS spectrum of azulene obtained from the ring-down time of light leaking from the cavity between 1.5 and 10.5 $\mu$ s after plasma formation. The ring-down time was measured in steps of 0.5 $\mu$ s accumulated over 500 plasma pulses (integration time of 250 $\mu$ s) per step. Blue trace: IBBCEAS spectrum of azulene (see Section 4.4.1) obtained by accumulating the cavity output for 500 plasma pulses from 1.5 to 10.5 $\mu$ s after plasma formation; total integration time of 4.5 ms. Determination of the extinction coefficient is based on the effective reflectivity shown in Fig. 4.4. Black trace: Arbitrarily scaled cavity ring-down absorption spectrum of jet-cooled azulene from [126] for comparison. Inset: Semi-logarithmic plot of the cavity output intensity showing the ring-down time measurements including the respective fit without and with azulene present in the cavity (red squares and dots respectively), measured at 631 nm (also compare Fig. 4.3). . . . .	77
4.7	CRDS absorption baseline (grey) determined from two separate ring-down measurements without azulene present within the cavity (see lower panel). Red trace: Cubic spline applied to the measured baseline. The grey shading indicates regions of the baseline that were excluded from SNR calculations due to the previously identified emission lines. . . . .	79
4.8	IBBCEAS absorption baseline (grey trace) determined from two separate accumulations (lower panel) of the cavity output without azulene present in the cavity. Red trace: Cubic spline applied to the measured baseline. The grey shading indicates regions that were not included in calculations of the SNR. . . . .	83

---

4.9	Measured IBBCEAS spectra of azulene for measurement delay times, $t_{\text{start}}$ , of 1.5 (black), 3.0 (red), and 4.5 (blue) $\mu\text{s}$ , with a measurement end-time, $t_{\text{end}}$ , of 10.5 $\mu\text{s}$ for each measurement. The increase in measured absorption with increasing delay time is due to the absorption of light that occurs prior to data collection. . . . .	85
4.10	Illustration of the source of error in pulsed IBBCEAS measurement with delayed (i.e. gated) data acquisition. $A(t)$ is the time-dependent cavity output intensity without (light green) and with (dark green) the sample. $I$ and $I_0$ (both dark grey) are the time-integrated intensities as measured in pulsed IBBCEAS during the gate time, i.e. $(t_{\text{end}} - t_{\text{start}})$ . $I'$ and $I_0'$ (both light grey) are the time-integrated intensities during an arbitrary delay time, $t_{\text{start}}$ , that needs to be accounted for. If not corrected, pulsed gated IBBCEAS will deliver absorption coefficients that are too high, depending on the gate delay. . . . .	86
4.11	Red trace: Broadband CRDS spectrum of gaseous static azulene in ambient air from Fig. 4.6. Blue traces: IBBCEAS spectra from Fig. 4.6 corrected using CRDS-based evaluation (1)-light blue ( $\varepsilon_{(1)}$ ), and CEAS-based evaluation (2)-dark blue ( $\varepsilon_{(2)}$ ). . . . .	90
4.12	Black: Absorption cross-section of azulene from Ref. [133]. Red: Vertically scaled CRDS spectrum of jet-cooled azulene from a previous study [126], for comparison. The point at 578.2 nm shows significant deviation from that expected from previous experimental results and has therefore been excluded from any calculations. . . . .	96
5.1	Relative cavity output intensity for an LIP generated by a ns-pulsed laser at the centre of a near-concentric cavity (upper plot), and a near-confocal cavity (lower plot). The factor of $\sim 2$ difference between the ring-down times ( $\tau$ ) is a consequence of the factor of 2 difference in cavity length. . . . .	101
5.2	Time-dependent cavity output intensity for three different cavity lengths showing how the time at which the maximum (indicated by dashed lines) in the output occurs changes with cavity length. A cavity length of 40 cm corresponds to a confocal cavity geometry. LIP generation was provided by a ns-pulsed laser. The three traces have been arbitrarily scaled for clarity. . . . .	102
5.3	Comparison of the typical time-dependence of the cavity output intensity for an LIP generated by a fs-pulsed laser (upper plot) and by a ns-pulsed laser (lower plot). In both cases the cavity was in a (quasi-) confocal arrangement with a length of $\sim 40$ cm. . . . .	103
5.4	Schematic illustration of the effect of the LIP on the probe beam, shown at four different stages: <b>(a)</b> before LIP formation, <b>(b)</b> immediately after LIP formation, <b>(c)</b> during LIP expansion, <b>(d)</b> after plasma expansion and cooling. The expected behaviours during each of these stages are described in the main body of the text. . . . .	104



5.5	Red trace: Relative probe beam intensity measured through a $200\ \mu\text{m}$ pinhole after being focused through an LIP. The spike in intensity is due to the lensing effect of the LIP. Black trace: Scaled time-dependent emission from the LIP. The shaded regions indicate the 4 regimes outlined in the text. . . . .	106
5.6	Relative intensity of a collimated He-Ne probe beam as a percentage of the unattenuated beam intensity (red trace, left-axis) passing through the LIP formation region showing the time-dependent absorption by the LIP. The total (integrated over all accessible wavelengths) emission intensity of the LIP (black trace) is shown for comparison. . . . .	107
5.7	Illustration (not to scale) of the imaging of the cavity output for the emission from an LIP formed at the centre of a confocal cavity. Blue lines represent the emission from the LIP that initially propagates in the left direction, while red lines represent light travelling to the right. The two different directions yield different focal positions for the imaged light, separated by a distance $\Delta f$ . . . . .	110
5.8	Illustration (not to scale) of the imaging of the cavity output for an LIP formed at the centre of a concentric cavity. Blue lines represent light emission from the LIP that initially propagates in the left direction, while red lines represent light travelling to the right. The point at which the cavity output is imaged is the same for light travelling in both directions. . . . .	110
5.9	Time at which the maximum occurs in the cavity output intensity as a function of the mirror separation for near-confocal arrangements ( $L \geq 40\ \text{cm}$ ), measured for an LIP generated with a ns-pulsed laser. . . . .	115
5.10	Simulation of the intra-cavity beam diameter of light propagating (5 mm step-size) within a quasi-confocal cavity showing the time required for light to reach a stable mode of propagation. . . . .	117
5.11	<b>(a)</b> Emission spectrum from an LIP generated by a fs-pulsed laser, measured in steps of 30 ns from immediately after plasma formation. The dip at $\sim 535\ \text{nm}$ is due to a notch filter to filter out stray laser light. <b>(b)</b> Black: LIP emission decay lifetime determined from a mono-exponential fit to the measured spectra. Red: $r^2$ values for the mono-exponential fit. . . . .	119

# List of Tables

2.1	Spectral resolution and spectral range of the spectrometer and iCCD combination for each of the three available gratings, measured with an entrance slit width of 100 $\mu\text{m}$ , at a wavelength of 632 nm. . . . .	29
3.1	Relevant quantities for the singly ionised nitrogen (N II) lines used to determine the LIP temperature. All data has been retrieved from the NIST ASD [116]. . . . .	60
3.2	Relevant quantities for the neutral oxygen (O I) lines used to determine the LIP temperature. All data has been retrieved from the NIST ASD [116]. . . . .	60
4.1	Comparison of the figures of merit for both the CRDS and IB-BCEAS approaches to CEAS with intra-cavity LIPs. . . . .	92
4.2	Values for the absorption cross-section of azulene within the mirror HR range, from Ref. [133]. . . . .	95

# Chapter 1

## Introduction

Since its development in 2003 [1], incoherent broadband cavity-enhanced absorption spectroscopy (IBBCEAS) has inspired a number of different experimental implementations for spectroscopic applications [2–5]. However, the sensitivity of IBBCEAS for trace gas monitoring is limited by the generally low coupling efficiency of incoherent light to the high-finesse optical cavities that are typically employed. Efforts to overcome this limitation have motivated the development of a new approach to IBBCEAS which relies on replacing the normal incoherent light source with a high-temperature thermal emission source in the form of a laser-induced plasma, generated by a short pulse laser, which is placed inside the optical cavity [6].

In this approach, the laser-induced plasma (LIP) represents a broadband, pulsed, incoherent light source that possesses an emission spectrum which stretches deep into the ultraviolet and into the infrared. Generating the light source inside an optical cavity acts to eliminate the need to couple incoherent light into the cavity through one of the cavity mirrors; one of the principle difficulties of the standard approach to IBBCEAS. As the LIP is generated *between* the cavity mirrors, some fraction of the optical emission from the LIP will be incident upon the surface of the cavity mirrors, assuming that the LIP emits in all directions, and this light will be sustained within the cavity. The collection efficiency of the LIP emission is

dictated by the mirror surface area and the separation between the cavity mirrors and the LIP, with shorter cavities yielding a higher collection efficiency. While it is anticipated that the LIP will present a significant optical loss within the cavity, it will be shown that, despite this loss, light is sustained within the cavity well beyond the emission lifetime of the LIP, thus allowing absorption measurements of the neutral gas that is within the cavity, using the light that is resonant within the cavity.

With this experimental implementation, intensity-dependent (i.e. IBBCEAS) absorption measurements are achievable by integrating the light that is output from the cavity, which contains information on absorption by the neutral gas species that are present within the cavity volume. In addition to this, by taking advantage of the pulsed nature of the LIP emission, broadband time-dependent (i.e. broadband cavity ring-down spectroscopy) absorption measurements are also facilitated by monitoring the time-dependence of the broadband cavity output intensity both with, and without, an absorbing species present in the cavity. Each of these two approaches to cavity-enhanced absorption spectroscopy measurements with LIPs provide their own advantages and drawbacks which will be discussed in Chapter 4.

This chapter will provide an introduction to the theory and experimental principle behind the two different cavity-enhanced absorption spectroscopy techniques used in this study: cavity ring-down spectroscopy (CRDS), and IBBCEAS. This is followed by a brief introduction to the phenomenon of laser-induced breakdown, and some information on high-finesse optical cavities, which will be of some relevance to the work presented in this thesis. The use of laser-induced plasmas as intra-cavity light sources for cavity-enhanced absorption spectroscopy is introduced in Section 1.5, along with a brief description of the anticipated experimental approach. The influence of the LIP on the propagation of light through the plasma region due to lensing effects will be discussed along with how this may affect the measured cavity output intensity.

This chapter concludes with a summary of the objectives of the work presented in this thesis, followed by a brief outline of the remaining chapters in this thesis.

## 1.1 Cavity ring-down spectroscopy

Cavity ring-down spectroscopy (CRDS), first demonstrated in 1988 [7], is a time-dependent CEAS<sup>1</sup> technique in which the absorption of a species is determined based on how its presence within a high-finesse optical cavity affects the rate of decay of a pulse of light that is resonant within the cavity. CRDS is a relatively simple, robust technique that offers high-sensitivity measurements applicable over a large spectral range, from the deep-ultraviolet [8] to the far-infrared [9], with a high measurement rate. As a result, CRDS has found extensive use in a number of areas, including reaction kinetics [10], atmospheric trace gas monitoring [11, 12], spectroscopy of radical compounds of astrophysical interest [13, 14], and medical analysis [15]. While initially employed for gas-phase measurements, the use of CRDS has subsequently been demonstrated for flames [16], aerosols [17], plasmas [18, 19], and in the condensed phase [20, 21].

While CRDS had exclusively made use of pulsed lasers in its early implementations, CRDS has subsequently been demonstrated using continuous wave (CW) lasers via a number of approaches [22–24]. The use of CW lasers further improved the resolution of CRDS through the much narrower line widths that they possess when compared to pulsed lasers.

Further developments saw the principle of CRDS being applied to broadband absorption measurements. This was achieved through a number of methods, including using a rotating mirror to disperse the cavity output onto a 2-dimensional detector array [25], a spectrometer with a clocked CCD [11], through use of a Fourier transform spectrometer [26], and using a gated CCD to temporally resolve broadband ring-down transients [27], although as this final approach relies

---

<sup>1</sup> In this thesis CEAS refers to all spectroscopic techniques which utilise optical cavities, regardless of the detection scheme employed.

on a series of independently measured spectra, it may introduce shot-to-shot noise from the light source into the measured ring-down transients. These broadband methods eliminated the need to scan the wavelength of a narrow-band laser for broadband measurements, however, this came at the expense of lower resolution measurements (limited by the detection system) and a general increase in experimental complexity in comparison to standard CRDS.

### 1.1.1 Experimental principle

In the simplest approach to CRDS, light from a pulsed laser is injected into a stable high-finesse optical cavity, through one of the cavity mirrors, along the optical axis. The light resonates within the cavity, with a small amount of light being transmitted through the cavity mirrors at each reflection, with the amount transmitted depending on the reflectivity of the mirrors<sup>2</sup>. This results in a diminishing pulse intensity inside the cavity over time, decaying at a rate dictated by the cavity round-trip losses experienced by the light in the cavity. Hence a time-dependent decrease in the intensity of the transmitted light is detected. A detector (typically a photo-diode) placed outside the second cavity mirror will see an exponentially decaying cavity output, where, if we assume an empty, otherwise loss-less cavity, the cavity output intensity at a time  $t$ ,  $I(t)$ , is described by the mono-exponential decay shown in Eq. 1.1. In Eq. 1.1,  $I(0)$  represents the measured cavity output intensity at  $t = 0$ , and the decay constant  $\tau_0$  is the characteristic *ring-down time* of the light in the cavity, which can be determined from an appropriate fit to the cavity output decay.

$$I(t) = I(0) e^{-\frac{t}{\tau_0}} \quad (1.1)$$

The ring-down time,  $\tau_0$ , is related to the cavity mirror reflectivity,  $R$ , according to Eq. 1.2, where  $L$  and  $c$  represent the cavity length and speed of light, respectively.

---

<sup>2</sup>  $A + T + R = 1$ , where  $A$ ,  $T$ , and  $R$  represent the fractional absorbance, transmission, and reflectivity of the mirror, respectively

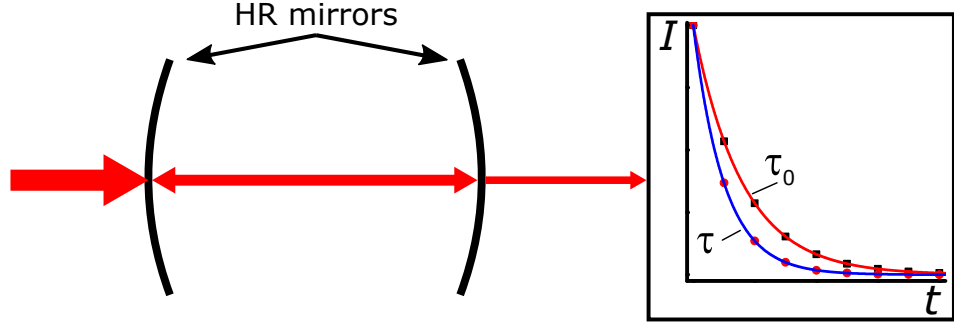


FIGURE 1.1: Illustration of the measurement principle of CRDS. The light leaking from the cavity with an absorbing species present (blue) decays at a faster rate than when there is no absorbing species present (red).  $\tau$  and  $\tau_0$  represent the exponential decay constants for each of these situations, respectively.

$$R = 1 - \frac{L}{c\tau_0} \quad (1.2)$$

In the presence of an absorbing sample across the full length of the cavity, the resonant light will be subject to further losses due to absorption, yielding a decreased ring-down time,  $\tau$  (see Fig. 1.1). As the absorption strength of the sample, and the mirror reflectivity vary with wavelength, both  $\tau$  and  $\tau_0$  are inherently wavelength-dependent. Based on the ring-down time of light within the cavity both with ( $\tau$ ), and without ( $\tau_0$ ), an absorbing species present, the extinction coefficient of the absorbing species,  $\varepsilon(\lambda)$ , can be determined using Eq. 1.3, where  $c$  represents the speed of light.

$$\varepsilon(\lambda) = \frac{1}{c} \left( \frac{1}{\tau(\lambda)} - \frac{1}{\tau_0(\lambda)} \right) \quad (1.3)$$

A full derivation of Eq. 1.3 is provided in Ref. [28].

As the measurement principle of CRDS is based on the rate of decay of a cavity signal, rather than the intensity of the signal itself, measurements via this approach are inherently immune to any fluctuations in the intensity of the light source employed. Additionally, absorption measurements carried out via CRDS yield absolute extinction coefficients without the need to first directly measure the cavity mirror reflectivity. As the ring-down time of the cavity serves as a measure of the mirror reflectivity (see Eq. 1.2), CRDS measurements are also unaffected by changes in the effective mirror reflectivity which may arise due to

drifts in the cavity alignment. As will be seen in Section 1.2, this is in contrast to IBBCEAS measurements which require an independent calibration of the cavity mirror reflectivity in order to measure extinction coefficients.

## 1.2 Incoherent broadband cavity-enhanced absorption spectroscopy

In the 15 years that followed its development in 1988 [7], cavity-based spectroscopy exclusively made use of coherent light sources due to a long-held belief that utilising temporally/spatially incoherent light sources would not provide any advantages due to their significantly lower emission intensity in comparison to lasers, along with their generally low coupling efficiency to high-finesse optical cavities [29]. Despite these apparent shortcomings, incoherent broadband light sources remained an attractive possibility due to the benefits that they provide over lasers for cavity-enhanced spectroscopy. The principle advantage of incoherent broadband sources is that wavelength selection takes place *after* the optical cavity which eliminates the need for wavelength scanning and enables multiplexed absorption measurements.

In a first step towards IBBCEAS, direct attenuation based CEAS was first demonstrated in 1998 by O’Keefe [30]. In this technique, labeled integrated cavity output spectroscopy (ICOS), the transmitted output of the cavity was simply integrated to provide a wavelength-dependent absorption spectrum. Following on from this, the use of incoherent light sources for CEAS was then demonstrated in 2003 when a short-arc xenon lamp was used to measure the  $\gamma$ -band of molecular oxygen and the  $S_1 \leftarrow S_0$  absorption spectrum of gaseous azulene [1]. IBBCEAS has subsequently been demonstrated with halogen lamps [31], high-power light emitting diodes [32], and supercontinuum lasers [33], enabling spectroscopic measurements over wavelengths ranging from the ultraviolet to the near-infrared.



### 1.2.1 Experimental principle

In conventional absorption spectroscopy the incident,  $I_0(\lambda)$ , and transmitted,  $I(\lambda)$ , light intensity through a sample of length  $d$  are measured and related to the extinction coefficient,  $\varepsilon(\lambda)$ , according to the Lambert-Beer law, as shown in Eq. 1.4. As the observed absorption, and hence, the measurement sensitivity, is dependent on the optical path length, the goal is generally to maximise this value. Maximisation of the path length beyond the size limitations of the experimental setup is generally achieved through the use of a variety of multi-pass cells [34–36].

$$\frac{I(\lambda)}{I_0(\lambda)} = e^{-\varepsilon(\lambda)d} \quad (1.4)$$

In CEAS, the optical path length through the absorbing sample is greatly increased by employing a high-finesse optical cavity formed by two high reflectivity (HR) dielectric mirrors (typically  $R > 0.999$ ) around the sample. For the experiments presented in this thesis, the cavity mirrors used had a nominal on-axis reflectivity of  $R = 0.9997$ . The cavity finesse,  $\mathcal{F}$ , represents a figure-of-merit for the cavity and is defined as:

$$\mathcal{F} = \frac{\pi\sqrt{R}}{(1-R)} \quad (1.5)$$

For a cavity of length  $L$ , the HR mirrors result in an effective cavity length,  $L_{\text{eff}} = L/(1-R)$ . Taking the effect of the mirrors into account, and assuming small losses (absorption) per pass of the light through the cavity, and approximating  $R \rightarrow 1$ , yields the standard IBBCEAS equation shown in Eq. 1.6, where  $I(\lambda)$  and  $I_0(\lambda)$  respectively represent the light transmitted through the optical cavity with, and without, an absorbing sample present, as shown in Fig. 1.2. A detailed derivation of Eq. 1.6 is provided in Ref. [1].

$$\varepsilon(\lambda) = \frac{1-R(\lambda)}{L} \left( \frac{I_0(\lambda)}{I(\lambda)} - 1 \right) \quad (1.6)$$

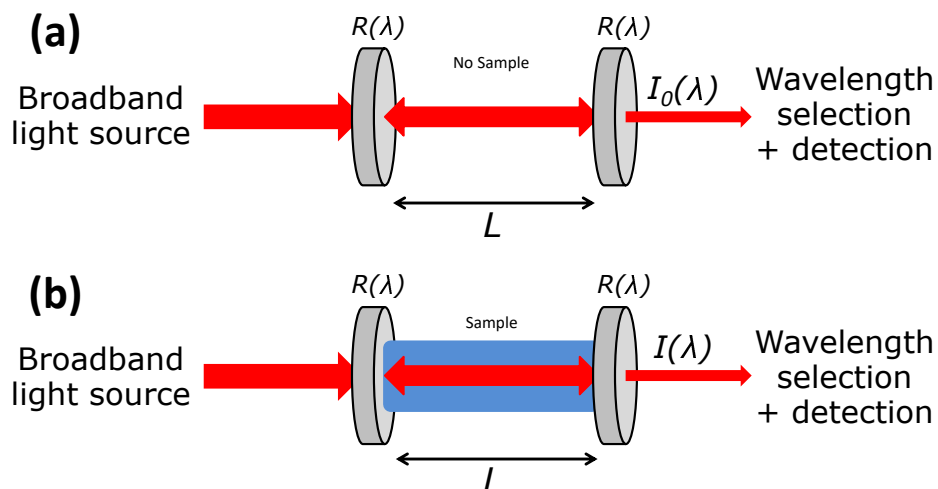


FIGURE 1.2: Experimental principle of IBBCEAS for a cavity of length  $L$ , comprised of mirrors with a reflectivity  $R(\lambda)$ .  $I_0(\lambda)$  is the cavity output without an absorbing sample present in the cavity, while  $I(\lambda)$  represents the measured cavity output *with* an absorbing sample present in the cavity.

In contrast to CRDS (see Section 1.1 above), the measurement principle of IBBCEAS is dependent on the wavelength-dependent cavity mirror reflectivity,  $R(\lambda)$ , being accurately known. Hence, measurements of absolute extinction coefficients via this approach first require the mirror reflectivity to be measured. Cavity mirror reflectivities are generally determined by measuring the optical loss from a known concentration of an absorbing species [37, 38], based on the wavelength-dependent ring-down time of broadband light in the cavity [39, 40], or via the known Rayleigh scattering cross-sections of two gases [41, 42].

For CEAS with broadband light, appropriate optical filters may be used to remove the optical frequencies that are outside the HR range of the cavity mirrors (see Fig. 1.3 for an example of a HR mirror reflectivity curve), if necessitated by the spectral range of the detection system. The light output from the cavity is coupled to a detection system which typically consists of a dispersive spectrometer in conjunction with a charge-coupled device (CCD), providing typical spectral resolutions of  $\sim 0.1$  nm to  $\sim 1$  nm. In the case of Fourier transform IBBCEAS (FT-IBBCEAS) [43], the cavity output is imaged into an interferometer, and spectra are retrieved from the Fourier transform of the recorded interferogram. This approach provides improved spectral resolutions typically between  $0.02$   $\text{cm}^{-1}$  and  $4$   $\text{cm}^{-1}$ .

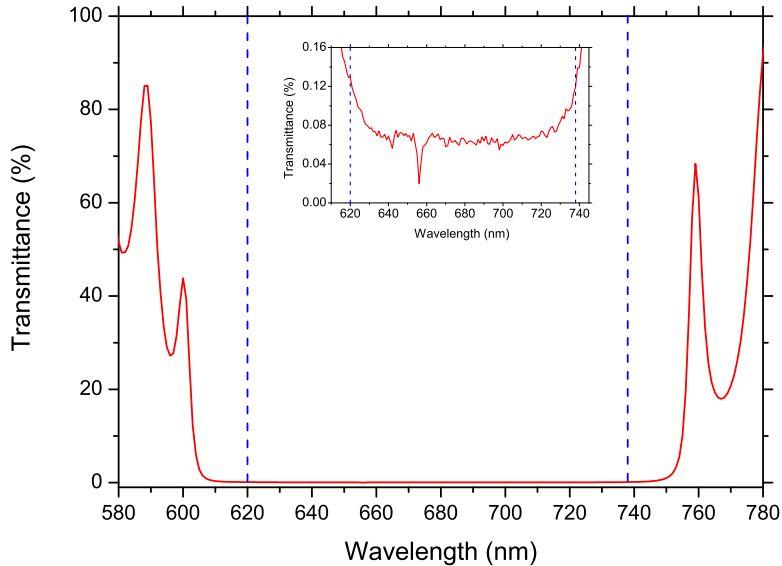


FIGURE 1.3: Representative HR cavity mirror transmittance curve for a mirror with a nominal (manufacturer stated) on-axis reflectivity of  $R = 0.9995$ , centred at 675 nm, measured with a spectrophotometer (Perkin Elmer Lambda 1050). Blue dashed lines indicate the HR range of the mirror. Inset: Zoomed in view of the HR range.

[3, 44], at the expense of greatly increased measurement times.

## 1.2.2 Performance considerations

In general, the performance of an absorption spectroscopy technique is assessed based on its signal-to-noise ratio (SNR), which is strongly dependent on the effective optical path length over which light can interact with a sample. CEAS methods, as shown above, have the advantage of possessing a significantly larger effective path length than conventional single-pass absorption spectroscopy techniques. However, they can be limited by the low coupling efficiency of light to optical cavities, although this issue is generally less severe for narrow-band lasers which can be mode-matched to the cavity to increase light throughput [29]. In the case of incoherent broadband light, mode-matching techniques can not be applied, although the light will, at any one time, contain light that corresponds to a large number of the cavity modes, hence, some of the light will always couple to

the cavity. The overall amount of coupled light is however greatly diminished in comparison to the narrow-band case, resulting in a reduced sensitivity, thus necessitating longer integration times to achieve the desired sensitivity. IBBCEAS integration times from less than one second [45] to multiple hours [43] have been reported.

Over time the cavity length continuously fluctuates (due to vibrations, thermal expansion, etc.) which results in a constantly changing cavity mode structure and, in turn, the frequencies of light that couple to the cavity. As a result, a portion of the incident light will always couple to the cavity and provided that the detection resolution is sufficiently low, no mode-structure will be observed in the detected cavity output. Therefore, the resolution of an IBBCEAS setup can be considered to be dependent only on the resolution of the light detection system. This fact, combined with the large spectral range, provide an experimentally simple means of multi-component detection.

### **1.3 Laser-induced breakdown**

The phenomenon of laser-induced breakdown was first demonstrated by Brech and Cross [46] in 1962, not long after the development of the laser [47], when they observed plasma emission from a metal target using a ruby maser. This phenomenon is based on the formation of a small, hot plasma when a high-power laser pulse is focused onto a sample, thus atomising and/or ionising a minute quantity of it. This laser-induced breakdown process was subsequently demonstrated in both the liquid and the gas phase and in aerosols [48, 49].

Laser-induced breakdown spectroscopy (LIBS) [50] is an atomic emission spectroscopy technique in which the laser-induced plasma (LIP) formed by this breakdown process yields an atomic/ionic emission spectrum which is characteristic of the composite elements of the sample, thus providing an elemental analysis of the sample. LIBS has been primarily applied to analysis of solid samples [51–53], but has also seen applications in gases [50], liquids [54], and aerosols [55].

### 1.3.1 Experimental principle

In the basic implementation of LIBS, a short duration laser pulse (typically ca. 10 ns) from a high-power laser is focused onto/into a sample, vaporising and exciting it to form a hot plasma, which occurs due to the electric field at the focus exceeding the dielectric strength of the medium. In general, a pulse power density greater than  $10^{10}$  W cm<sup>-2</sup> is required for plasma formation by this method, depending on the target material in question [56–58]. The plasma formation process is discussed in detail in Ref. [59]. The LIP goes through a number of phases as it expands and cools. A brief description of the main phases in the temporal evolution of the LIP are described below [60–62]:

- (i) The initial LIP (< 100 ns after formation) is hot and dense and is characterised by high electron and ion densities ( $10^{15} - 10^{19}$  cm<sup>-3</sup>) [60]. The emission spectrum from the LIP at this point features a broad continuum (i.e. blackbody) emission which arises due to strong collisions between free electrons and excited ions and atoms in the plasma. A number of ionic and atomic emission lines are overlaid on the broadband continuum, with these lines being broadened due to contributions from a number of processes. Descriptions of the main broadening processes that pertain to LIPs, including Doppler, Stark, and collisional broadening, are provided in Ref. [63].
- (ii) After the initial high-density phase, the plasma expands rapidly [61] and begins to cool. During this cooling and expansion ( $100 \text{ ns} < t < \sim 1 \mu\text{s}$ ) the broadband emission decays rapidly, with the emission lines becoming narrower and also reducing in intensity.
- (iii) For longer delay times (typically  $> 1 \mu\text{s}$ ), emission lines from ionised species are mostly absent, with the emission spectrum at this point being mainly comprised of emission lines from neutral atoms and molecules.

The emission behaviour in the three phases during plasma evolution are illustrated in Fig. 1.4, which depicts the LIBS spectra of an LIP formed in lab air, measured

for three delay times,  $t_d$ , of 0, 0.5, and 1.9  $\mu\text{s}$  after plasma formation. The spectra shown in Fig. 1.4 were measured with a 50 ns integration window, accumulated over 100 LIP excitations. For comparison, a selection of emission lines from both ionised species and neutral atoms are indicated in Fig. 1.4.

In general, the shot-to-shot reproducibility of an LIP, and hence the precision of LIBS measurements, are hampered by variations in the laser pulse power or changes in ambient conditions of the plasma formation region. The factors which may influence the precision of elemental analysis with LIBS, including laser stability, ambient humidity, and the presence of aerosols, have been comprehensively studied [64–66].

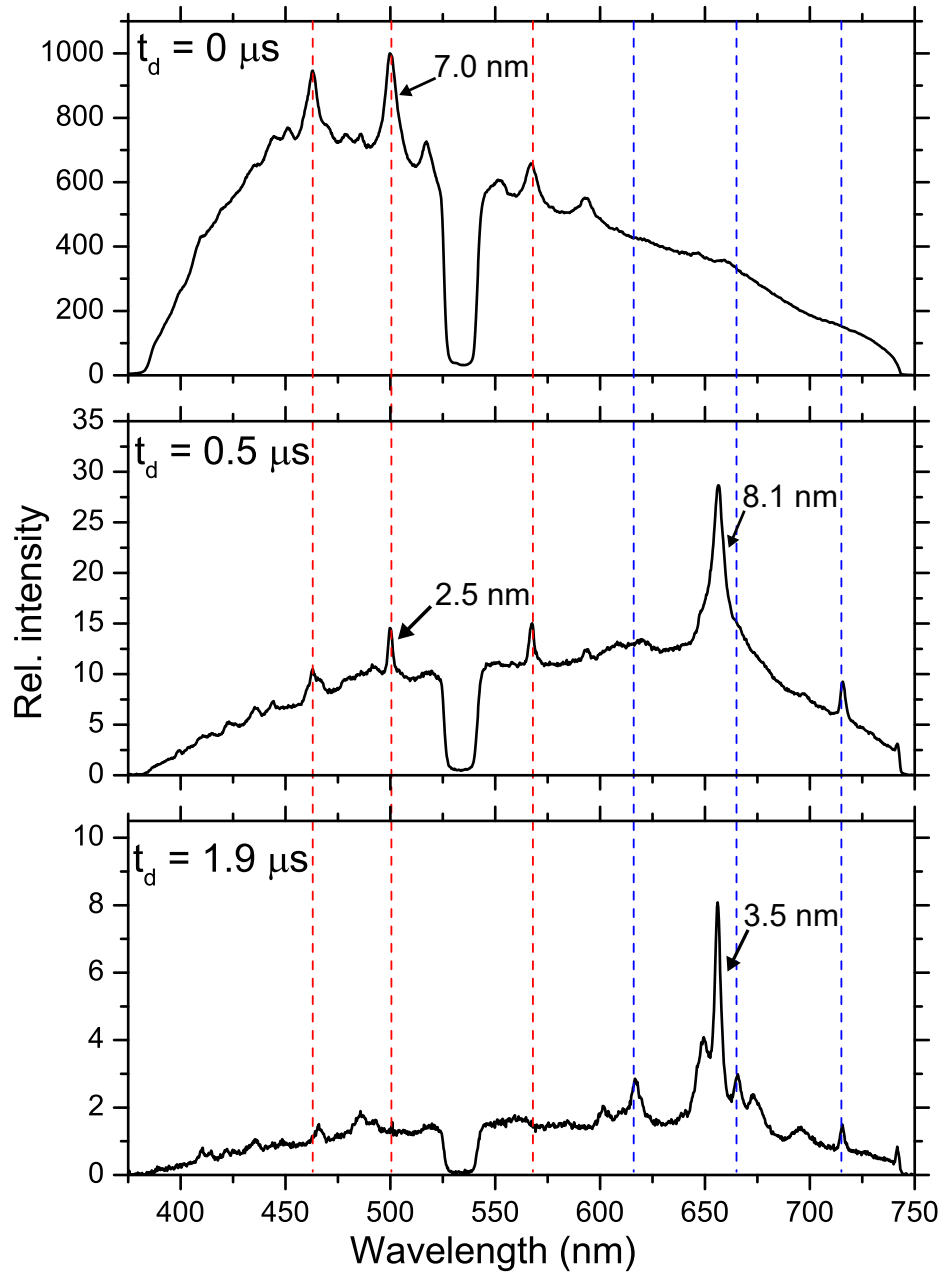


FIGURE 1.4: LIBS spectra recorded at three different delay times for an LIP formed in lab air, showing how the plasma emission changes with time. Note the different vertical scales for each spectrum. The spectra were recorded with a 50 ns integration window, accumulated over 100 LIP excitations. The red dashed lines indicate some of the emission lines from singly ionised nitrogen and oxygen, while the blue dashed lines indicate emission from neutral atoms. FWHM values for select lines are indicated on the plot. The dip in the spectra around 532 nm is due to a notch filter to protect the detection system from stray light from the laser pulse used for plasma formation.

## 1.4 High-finesse optical cavities

Below is a brief overview of optical cavities, and the cavity stability criterion, with particular emphasis on the two cavity geometries which are relevant to this study: symmetric confocal and concentric resonators. A far more comprehensive explanation of optical cavities can be found in Refs. [67–69].

Cavity-enhanced absorption techniques typically make use of high-finesse, linear optical cavities comprised of two opposing HR mirrors (reflectivity,  $R$ ) separated by some distance,  $L$ . For CEAS measurements linear optical cavities are mostly used as part of flow cells [70], static cells [71], or as part of vacuum chambers for low pressure measurements [72]. CEAS has also been performed with more elaborate cavity arrangements, including prism-based cavities [4, 73], folded-cavities including internal-reflection optics [74], and in multiple mirror ring-cavities [75], along with a number of different micro-scale cavity implementations [76–78]. The information below is not concerned with these alternative cavity arrangements, focusing only on the linear 2-mirror cavities which are relevant to this work.

### 1.4.1 Optical cavity stability

For a given cavity geometry (cavity length, and mirror curvature), the cavity is said to be stable if the  $g$ -parameters,  $g_1$  and  $g_2$ , shown in Eqs. 1.7a and 1.7b, satisfy the stability criterion given in Eq. 1.8. In these equations,  $L$  represents the mirror separation (cavity length), while  $r_1$  and  $r_2$  represent the radii of curvature of the two cavity mirrors. Cavities in which both mirrors have the same radius of



curvature, i.e.  $r_1 = r_2$ , and hence,  $g_1 = g_2$ , are said to be *symmetric resonators*.

$$g_1 = 1 - \frac{L}{r_1} \quad (1.7a)$$

$$g_2 = 1 - \frac{L}{r_2} \quad (1.7b)$$

$$0 < g_1 g_2 < 1 \quad (1.8)$$

Fig. 1.5 shows  $g_1$  vs.  $g_2$  with the range of  $g$  values that correspond to stable cavity geometries indicated with blue shading. Also indicated are three special cases of symmetric cavity, which are described below:

- Concentric**      Cavity mirrors have the same centre of curvature, i.e.  $L = 2r$ , ( $g_1 = g_2 = -1$ ). See Fig. 1.6.
- Confocal**        Cavity mirrors have the same focal point, i.e.  $L = r$ , ( $g_1 = g_2 = 0$ ). See Fig. 1.6.
- Plane-parallel**    Cavity mirrors are both plane mirrors, i.e.  $r = \infty$ , ( $g_1 = g_2 = 1$ ).

For each of these three cases the cavity is at the limit of stability, and, in all three cases the cavity is prone to increased losses due to any variations in the cavity alignment. As a consequence of this tenuous stability, in most practical scenarios the cavity length will generally be slightly off that required for a true concentric/confocal geometry, and these cavities are therefore referred to as near-(or quasi-) concentric/confocal.

This sensitivity to the cavity geometry is most notable for the confocal cavity in which significant losses are observed for variations in cavity length  $> 1\%$  [79]. Despite this sensitivity, near-confocal cavities are generally less sensitive to small

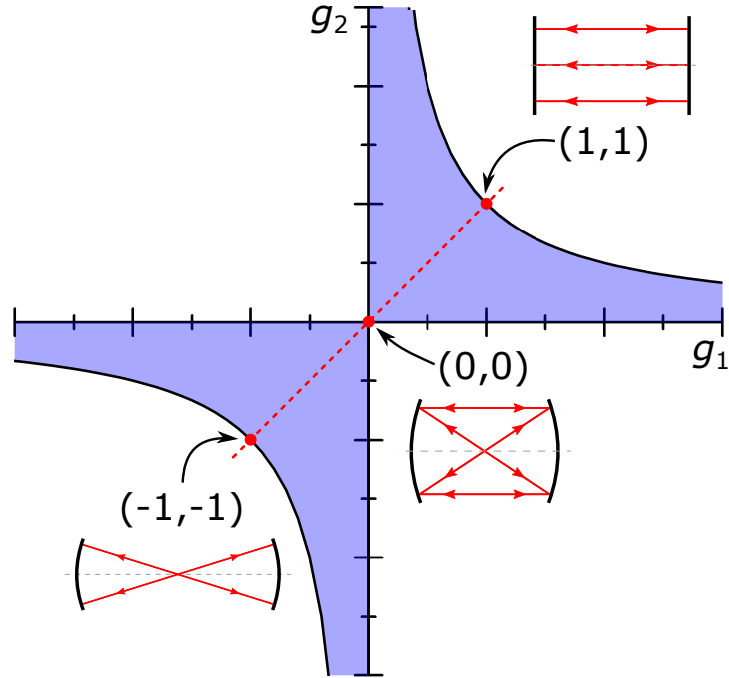


FIGURE 1.5: Stability diagram for optical resonators with spherical mirrors. The shaded areas indicate stable cavity configurations, determined from the  $g$ -parameters (Eqs. 1.7a and 1.7b). The dashed red line signifies symmetric cavity geometries, with three special cases highlighted: Concentric  $(-1, -1)$ , confocal  $(0, 0)$ , and plane-parallel  $(1, 1)$ .

misalignments of the cavity mirrors when compared to other stable optical cavities [79], and Fiedler et al. found that symmetric confocal resonators provide the optimal imaging efficiency of the light output from the cavity [80]. As a result, the near-confocal cavity remains a desirable cavity geometry for CEAS experiments.

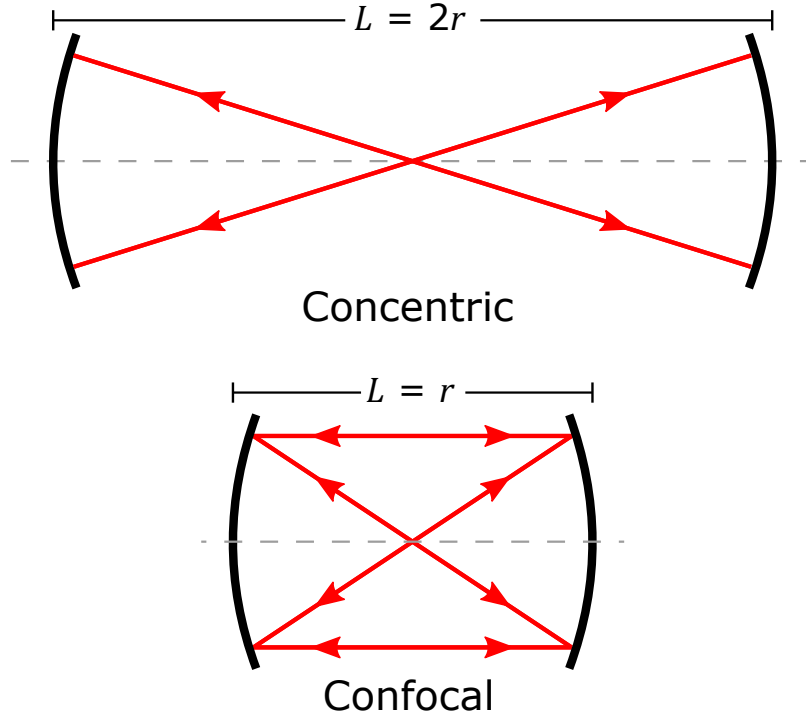


FIGURE 1.6: Ray-trace diagrams showing light propagation within concentric (upper) and confocal (lower) optical cavities.  $r$  represents the cavity mirror radius of curvature, which is the same for both cavity mirrors in this example (i.e. a symmetric resonator).

## 1.5 Cavity-enhanced absorption spectroscopy with laser-induced plasmas

As outlined in Section 1.2.2, the main limitation of IBBCEAS is the generally low coupling efficiency of incoherent light into high-finesse optical cavities, which acts to reduce the overall SNR of IBBCEAS measurements. This low coupling efficiency has motivated the development of an experimental approach in which the principles of laser-induced breakdown (see Section 1.3) are applied to generate light within a high-finesse optical cavity in the form of a laser-induced plasma [6]. Generating a plasma within an optical cavity aims to avoid the losses incurred when injecting light into a cavity through one of the cavity mirrors by allowing the optical emission from the plasma to be collected by the cavity mirrors without having to first pass through one of the cavity mirrors.

The motivation behind this approach is to increase the overall amount of light

inside the optical cavity without applying the principle of intra-cavity laser absorption spectroscopy (ICLAS) (also known as ICAS) [81]. ICLAS is an established spectroscopic technique in which an absorbing species is included in a laser cavity together with a laser gain medium whose broadened gain exceeds the absorption linewidth of the absorbing species. Measuring the optical losses due to the absorbing species before the laser reaches the lasing threshold yields an absorption spectrum. This approach also differs from the method of cavity-enhanced self-absorption spectroscopy (CESAS), as described by Walsh et al. [72, 82]. CESAS eliminates the need for an external light source by making use of the light emission from an absorbing plasma discharge or flame within a high-finesse cavity to measure the self-absorption of the plasma/flame itself.

LIPs in air have previously seen use as light sources for (single pass) absorption and scattering measurements due to their high-intensity ultraviolet emission [83–85], however the use of LIPs as intracavity light sources for cavity-enhanced absorption measurements was not demonstrated until 2015, when Ruth et. al [6] used an LIP, generated by a 200 fs pulsed Nd:glass laser, at the centre of a quasi-confocal (see Section 1.4) optical cavity to measure part of the  $S_1 \leftarrow S_0$  absorption spectrum of gaseous azulene, as well as the strongly forbidden  $\gamma$ -band in molecular oxygen.

This combination of LIPs with IBBCEAS provides information on absorption by the sample within the optical cavity, while also having the potential to provide a simultaneous elemental analysis of the sample gas by monitoring the direct emission from the LIP, as in standard LIBS. However, in the case of trace gases, direct LIBS measurements are not always viable due to the low concentration of the absorbing sample in the carrier gas, with LIBS detection limits for elemental analysis of trace gases vary from  $\sim 5$  parts-per-billion (ppb) to  $\sim 75$  parts-per-million (ppm), depending on the particular trace gas, and the carrier gas [86, 87].

### 1.5.1 Experimental principle

In this experimental approach, a LIP, which is generated at the centre of a high-finesse optical cavity, acts as a pulsed broadband thermal (blackbody) light source. While the broadband emission from the LIP is utilised as a pulsed light source for CEAS measurements of an absorbing sample inside the cavity, additional information on the laser-induced breakdown process of the sample gas may, in principle, also be obtained by applying the principles of LIBS.

In the typical approach to these experiments the LIP is formed by a short pulse from a high-power laser focused to the centre of a high-finesse optical cavity, on the optical axis. A portion of the broadband optical emission from the LIP is collected by the mirrors and is sustained in the cavity where it is absorbed by an absorbing species present in the cavity, and the light leaking through one of the cavity mirrors is monitored with a spectrometer and iCCD, as in standard IBBCEAS. If the LIP is assumed to emit isotropically, then the collection efficiency,  $\eta$ , of the plasma emission is dictated by the mirror surface diameter,  $d_m$ , and the cavity length,  $L$ , as shown in Eq. 1.9.

$$\eta = \frac{1}{2} \left( \frac{d_m}{L} \right)^2 \quad (1.9)$$

While Eq. 1.9 suggests that minimising the cavity length, within the limits of cavity stability (see Fig. 1.5), will maximise the collection efficiency, this is not always desirable. In experimental systems of this nature, the reflectivity of the cavity mirrors may be prone to degradation due to deposition of particles formed in the LIP, and therefore, the cavity length must be chosen so as to maximise both the collection efficiency of light, along with the longevity of the system. A small purge flow over the cavity mirrors may help to protect them from particle deposition, although this is not always an option for static gas applications.

For applications in CEAS, there are a number of aspects which are unique to this approach, in particular, upon plasma generation, a strong optical loss is present

within the cavity for a duration determined by the lifetime of the plasma. While the emission lifetime of the LIP is typically of the order of 100 ns, the plasma expansion, cooling, and charge recombination take significantly longer. As the plasma lifetime is markedly longer than the light round-trip time in the cavity ( $\sim 6.7$  ns for a 1 metre cavity, where a round-trip is defined as one pass back-and-forth through the cavity), the light within the cavity will experience a time-dependent loss due to the plasma. This time-dependence arises due to contributions from three different time-regimes in the LIP process:

1. Initially, when the gas within the cavity is far away from equilibrium, the LIP acts as a significant loss within the cavity, reabsorbing a large portion of the light that is incident upon it.
2. As the LIP cools and expands (approaches equilibrium), it becomes increasingly transparent, however, the hot plasma acts as a non-linear medium, which distorts the propagation of light through/near the plasma region.
3. Eventually, the LIP will have cooled sufficiently that the gas in the cavity will have returned to equilibrium and light may propagate freely within the cavity.

The extent to which the non-linear properties of the expanding LIP affect the propagation of light within the cavity, and hence, the measured time-dependent intensity of the light leaking from the cavity, will be discussed in Chapter 5.

As the LIP acts as a pulsed broadband light source, this experimental approach facilitates both intensity-dependent (IBBCEAS) measurements by integrating the cavity output, and time-dependent (BB-CRDS) measurements by spectrally dispersing, and temporally resolving the broadband ring-down transients with a gated iCCD, as demonstrated by Czyzewski et al. [27]. The application of this approach to each of these spectroscopic techniques will be discussed in Chapter 2.

## 1.5.2 Influence of laser-induced plasmas on the propagation of light in optical cavities

As previously mentioned, the presence of the LIP affects the propagation of light through the plasma formation region due to lensing effects of the LIP that arise due to the high temperatures and strong electric fields around the LIP. These act to produce a localised non-linear refractive index change around the plasma formation region. In the context of light resonant within an optical cavity, these lensing effects lead to increased losses of light from the cavity while also affecting the imaging efficiency of the light that is output from the cavity. This yields an unusual time-dependence in the measured cavity output intensity, characterised by a rapid decrease in output intensity due to loss of light through absorption by the LIP and reduced cavity stability due to the lensing effects. As will be seen in Chapter 5, this is, in some cases, followed by a subsequent increase in the cavity output intensity as the lensing effects diminish, thus allowing the resonant light to return to a stable resonance in the optical cavity. Similar effects of localised refractive index changes within optical cavities have been previously documented in the case of absorption spectroscopy of flames [88–90], however the effects are expectedly much more significant when considering laser-induced plasmas. For absorption measurements (See Chapter 4), this behaviour of the light within the cavity necessitates a delay, typically 1 – 2  $\mu\text{s}$ , between LIP formation and data collection as the resonant light must first reach a stable resonance. This delay results in a decreased measured signal intensity, thus yielding a decreased SNR, whilst also imparting a measurement offset into IBBCEAS measurements. Details of this offset will be provided in Section 4.5.

As will be seen in Chapter 5, the time-dependence of the cavity output intensity is influenced by the particular cavity geometry used (i.e. confocal, concentric, or otherwise). This dependence on cavity geometry arises due to differences in how resonant light propagates within cavities of differing geometry, with certain configurations being less sensitive to the effects of the LIP.

The LIP-induced local refractive index change has been demonstrated through a simple experiment designed to observe the effects of the LIP on the propagation of a probe laser beam through the LIP formation region. This experimental approach is described in Section 2.4, with the results of the experiment, and how they pertain to the propagation of light within an optical cavity, outlined in Chapter 5.

## 1.6 Thesis objectives and outline

The following provides a brief overview of the objectives of the work presented in this thesis followed by a short summary of the outline of the thesis.

### 1.6.1 Thesis objectives

#### **LIP characterisation**

As it is to be used as a light source for cavity-based absorption spectroscopy methods, the emission from an LIP generated by a nano-second pulsed laser must first be characterised in terms of its broadband emission spectrum, stability, and decay rate, so as to determine its suitability as a light source.

#### **CEAS with intra-cavity LIPs**

Subsequently, the work in this thesis will demonstrate the use of an LIP as a light source for two different approaches to cavity-based absorption spectroscopy:

- (i) Intensity-dependent IBBCEAS measurements, relying on the integrated cavity output spectrum.
- (ii) Time-dependent broadband CRDS, which utilises the decay rate of the cavity output intensity to determine a broadband absorption spectrum.

These two approaches are to be compared in terms of performance and experimental complexity.



The nature of the IBBCEAS measurement principle using a pulsed LIP results in inaccuracies in the measured absorption spectra which are positively offset from the true value. The source of this offset will be identified and a numerical correction procedure which accounts for the offset will be presented.

The pulsed nature of the LIP also facilitates a simple means of determining effective cavity mirror reflectivities *in situ*, thus enabling the measurement of absolute extinction coefficients with the IBBCEAS approach. This calibration process will be expanded on and demonstrated in this thesis.

### **Influence of LIPs on light propagation in cavities**

Finally, the first CEAS experiments that utilised an LIP as an intra-cavity light source yielded an unusual time-dependent behaviour of the cavity output intensity, which came about due to the effects of the LIP on light that is resonant within the optical cavity. Part of the work presented in this thesis is motivated by the objective of identifying and quantifying the factors that contribute to this observed behaviour. Particular attention will be paid to the time-varying lensing effects of the LIP on light that propagates through the plasma medium, and the influence that these have on the cavity stability.

### **1.6.2 Thesis outline**

The outline of the remainder of this thesis is as follows:

*Chapter 2* provides details of the main experimental equipment used, including light sources, detectors, and optics, along with descriptions of the experimental approaches, and relevant aspects of using LIPs as intra-cavity light sources for both CRDS and IBBCEAS. In addition to this, the laser-induced plasma formation process is outlined and its suitability as a light source for absorption spectroscopy measurements is investigated. The final section of Chapter 2 deals with the experimental approach to demonstrate the lensing effects of the LIP.

*Chapter 3* presents further information on the spectral properties of the broadband continuum emission from the LIP, and also provides an analysis of the temperature of the LIP, which is of relevance to the emission spectrum of the LIP.

*Chapter 4* presents the results, and all relevant details, of utilising LIPs as intracavity light sources for both time-dependent (CRDS), and intensity dependent (IBBCEAS), cavity-enhanced absorption spectroscopy measurements, with particular attention paid to the issue of the measurement offset observed in IBBCEAS measurements. A comparison is made between the two approaches, comparing the relevant advantages and drawbacks of each.

*Chapter 5* deals with the influence of the lensing effects of the LIP on the propagation of light within optical cavities and how this impacts the measured cavity output intensity, thus affecting the performance of CEAS measurements. The results of the experiments to demonstrate the lensing effects of the LIP are provided, along with discussions on how the significance of the effects of the LIP on the time-dependence of the cavity output intensity are dependent on the particular cavity geometry.

A brief summary concludes the thesis in *Chapter 6*.

# Chapter 2

## Experimental

This chapter presents an overview of the practical experimental aspects of the work presented in this thesis. Section 2.1 provides a description of the experimental setup used in cavity-based absorption experiments with intra-cavity LIPs, along with details of the main experimental devices and apparatus used in these experiments, including light sources, the detection system, and optics. Section 2.2 outlines the experimental process when applying this experimental setup to time-dependent (CRDS), and intensity-dependent (IBBCEAS) absorption measurements. Section 2.3 deals with the laser-induced formation process, including the stability of the broadband continuum emission from the LIP. The final section provides a description of the experiments that were used to investigate the non-linear refractive index change induced by the LIP.

### 2.1 Experimental setup

This section provides a description of the experimental system, including all experimental apparatus, used for cavity-based absorption measurements using a laser-induced plasma as an intra-cavity light source.

Fig. 2.1 shows a schematic of the typical experimental setup used for cavity-enhanced absorption measurements with utilise an LIP as an intra-cavity light source. The high power pulses from a Nd:YAG laser are focused by the fused-silica lens  $L_1$  ( $f = 3$  cm) to the centre of the optical cavity formed by the mirrors  $M_1$  and  $M_2$ . The short focal length of the lens helps to produce a small LIP at the centre of the cavity, which allows a greater collection efficiency of the emitted light. A beamsplitter (BS) is inserted into the laser beam with the small portion of the beam that is split off being sent to a pyroelectric energy meter (EM, Molelectron J9-453) which, via an oscilloscope (Tektronix TDS220), monitors the laser pulse energy. The light that leaks through one of the cavity mirrors is focused with an achromatic lens,  $L_2$ , ( $f = 8$  cm) onto the aperture of a fibre bundle which guides the light to the entrance slit of the detection system. A notch filter (F) centred at 533 nm (FWHM = 17 nm) in front of the fibre acts to prevent any stray laser light from entering the detection system. Triggering of the system is facilitated by a signal generator (SG, TTI TG1010) which provides transistor-transistor logic (TTL) pulses at a frequency of 9.7 Hz which trigger the Nd:YAG laser and, via a digital delay generator (DDG), the iCCD. A fast photodiode (Thorlabs DET200) which detects stray light from the laser is monitored with an oscilloscope (LeCroy Waverunner LT372) to enable tuning of the DDG such that  $t = 0$  for the iCCD coincided with LIP formation. The trigger frequency of 9.7 Hz (less than the maximum laser repetition rate of 10 Hz) was chosen as it represents the maximum measurement frame rate possible with the current detection system.

### 2.1.1 Light sources, detection system, and optics

The following provides details on the light sources used for LIP formation, the detection system, and the optical cavity mirrors used in the experiments that are described below. Brief descriptions of any additional optics used are also provided.

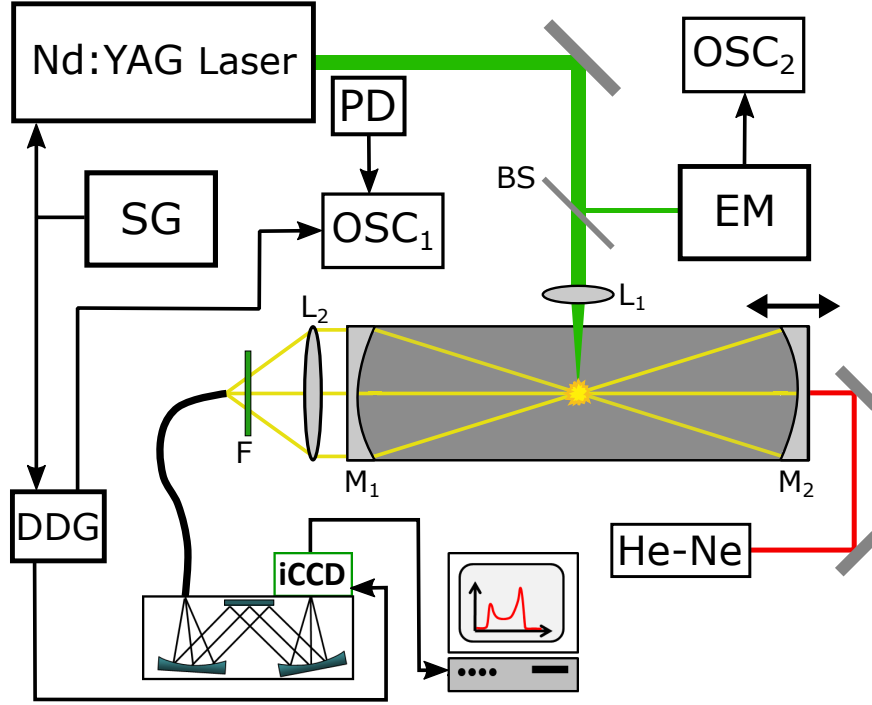


FIGURE 2.1: Typical experimental setup for cavity based measurements. The Nd:YAG laser produces high power pulses which are focused by  $L_1$  to the centre of the cavity formed by  $M_1$  and  $M_2$ , to produce an LIP.  $M_2$  is mounted on a translational stage which allows the cavity length to be varied ( $\pm 4$  cm). A He-Ne laser is used for alignment of the optical cavity.  $L_2$ : Achromatic lens to image the cavity output onto the aperture of a fibre bundle, with the notch filter,  $F$ , preventing any laser stray light from entering the detection system. BS: Beamsplitter to monitor laser pulse energy with an energy meter (EM) and oscilloscope (OSC<sub>2</sub>). SG: Signal generator to trigger the laser and, via a digital delay generator (DDG), the iCCD. The laser output is monitored with a photodiode (PD) and oscilloscope (OSC<sub>1</sub>).

### 2.1.1.1 Lasers

#### Nanosecond-pulsed laser

Most experiments in this thesis were performed using an actively Q-switched ns-pulsed neodymium-doped yttrium aluminium garnet (Nd:YAG) laser (Lumonics HY400). This laser provided pulses with an energy that could be varied between 5 and 132 mJ, with a shot-to-shot energy fluctuation of  $\pm 3$  %. The laser pulses had a full-width at half-maximum (FWHM) duration of  $\sim 10$  ns, and could be delivered at repetition rates between 1 and 10 Hz, with a timing jitter of  $\pm 200$  ns between pulses. The typical parameters used for these experiments were a laser pulse energy of 55 mJ, which corresponded to a peak power per pulse of  $\sim 5.5$  MW,

at a repetition rate of 9.7 Hz, which corresponded to the maximum frame rate of the detection system used, details of which are provided below.

The emission from the laser resonator at 1064 nm was frequency doubled via a thermalised potassium dihydrogen phosphate (KDP) crystal, with both the fundamental wavelength (1064 nm) and the second harmonic (532 nm) present in the output light, with an 85%/15% energy split between the fundamental and the second harmonic.

### **Femtosecond-pulsed laser**

For LIP formation with femtosecond pulses, the laser used was a neodymium-doped glass (Nd:glass) laser (Light Conversion Ltd. TWINKLE), which used an active-passive mode-locked negative-feedback controlled master oscillator, a stretcher, a Nd:glass regenerative amplifier, and a compressor. Active-passive mode-locking of the laser is achieved through the use of a saturable absorber comprised of a laser dye (No. 3274y) dissolved in methanol stabilised with tartaric acid and modulation of the cavity losses by means of a Pockels cell. This laser provided pulses with an energy of  $\sim 2.6$  mJ, at a repetition rate of 27 Hz, with a shot-to-shot energy stability of approximately 10% and a timing jitter of  $\pm 20$  ns between pulses. The laser pulses had a duration of 900 fs, and were further compressed, with a KDP crystal using a pre-delay between pulses of orthogonal polarisation, to 200 fs. This corresponded to a peak power per pulse of  $\sim 13$  GW. More details of the laser used are provided in Refs. [91, 92].

Both the fundamental wavelength of 1055 nm, and the frequency doubled second harmonic at 527 nm were present in the laser output.

#### **2.1.1.2 Detection system**

The detection system consisted of a spectrometer in conjunction with an intensified charge-coupled device (iCCD). The spectrometer (Andor Shamrock 303i), operated in a Czerny-Turner [93] arrangement, with an entrance slit width of 100  $\mu\text{m}$ ,

which corresponded to the diameter of the individual strands of a circular-to-rectangular fibre bundle which was used to guide light to the detection system. The spectrometer had three available holographic gratings: 150, 600, and 1800 lines/mm. The corresponding measured spectral resolutions for each of these gratings, which were determined using the emission from a low pressure neon Pen-Ray lamp (Quantum Design), are listed in Table 2.1. The same Pen-Ray lamp was also used for the wavelength calibration of the detector. The medium dispersion grating (600 lines/mm) provided a sufficient spectral range to cover the high reflectivity range of the cavity mirrors used (see Section 2.1.1.3) in the absorption experiments presented in this thesis.

The output from the spectrometer was detected by the iCCD (Andor iStar DH740\_18mm) which had 2048 x 512 pixels of 13 x 13  $\mu\text{m}^2$ , with a sensitivity across the visible range. The detector was cooled to  $-10\text{ }^\circ\text{C}$  via a thermoelectric cooler, so as to reduce the dark current in the iCCD. The iCCD could be temporally gated with a minimum gate width of 100 ps, and a minimum gate step of 25 ps, allowing the iCCD to monitor temporally dynamic processes. The iCCD recorded spectra with a maximum frame rate of 9.7 Hz.

<b>Grating (lines/mm)</b>	<b>Resolution (nm)</b>	<b>Spectral range (nm)</b>
150	1.56	$\sim 300$
600	0.34	$\sim 90$
1800	0.095	$\sim 22$

TABLE 2.1: Spectral resolution and spectral range of the spectrometer and iCCD combination for each of the three available gratings, measured with an entrance slit width of 100  $\mu\text{m}$ , at a wavelength of 632 nm.

### 2.1.1.3 Optical cavities

For optical cavity based measurements, the cavity was comprised of two plano-concave high reflectivity (HR) mirrors (Layertec GmbH) which had a surface diameter of 4 cm, and a radius of curvature of 40 cm, with a nominal on-axis reflectivity of  $R > 0.9997$ , over the spectral range 580 – 635 nm, according to the manufacturer data sheet. Based on the 40 cm radius of curvature, confocal cavity geometries would require a cavity length (mirror separation) of 40 cm, with a cavity length of 80 cm utilised for concentric cavity geometries (see Section 1.4 for more details on optical cavities).

The cavity mirrors were mounted in kinematic mirror holders separated by the distance dictated by the desired cavity geometry (i.e. concentric, confocal, or otherwise) with one of the mirror holders mounted on a translational stage which facilitated fine-tuning of the cavity length. An unstabilised helium-neon laser (JDSU 1137) was used to define the optical axis of the cavity, and for alignment of the two cavity mirrors.

### 2.1.1.4 Additional optics

Along with the cavity mirrors above, a number of additional optics were used throughout the experimental work, a brief description of each follows.

In the experimental studies described below, three principle lenses were used. LIP formation was provided by a 30 mm focal length fused-silica lens. More details of this lens and the LIP formation process are provided in Section 2.3.1 below. For CEAS measurements, an N-BK7/SF2 achromatic doublet with a focal length of 80 mm was used to image the cavity output onto the fibre bundle of the detection system. The diameter of this lens was 5 cm which was in excess of the 4 cm cavity mirror diameter, thus ensuring collection of all of the light output from the optical cavity. The final lens, which was only used for the experiments investigating the non-linear refractive index changes induced by the LIP (see Section 2.4 below), was also a fused-silica lens of 30 mm focal length.



Due to its low absorption and high damage threshold, an uncoated calcium fluoride ( $\text{CaF}_2$ ) window with a thickness of 2 mm was placed, at an angle, in the path of the laser and split off 5.8% of the incident laser beam, which was sent to a power meter to facilitate monitoring of the laser pulse energy. The thin window caused minimal deviation of the transmitted light.

In all cases, a dielectric notch filter centred at 533 nm (FWHM = 17 nm) was placed in front of the fibre of the detection system to prevent stray light from the LIP-formation laser, which would pose a risk of damage to the iCCD, from entering the detection system. Even in the case of cavity-based experiments, in which the spectrometer was tuned such that the laser light was outside its spectral range, the notch filter was still used, as the risk of damage from internal reflections of “out of range” stray light is still present.

## **2.2 Cavity-enhanced absorption spectroscopy with laser-induced plasmas**

This experimental setup described above was applied to two different approaches to CEAS with intra-cavity LIPs. Broadband CRDS measurements are carried out by spectrally and temporally resolving the decaying cavity output after plasma formation using the gating features of the iCCD. Measurements of IBBCEAS spectra are also achieved by integrating over a large portion of the broadband cavity output after plasma formation. Full descriptions of how this experimental setup is applied to each of these CEAS techniques are provided in this section.

### **2.2.1 Broadband cavity ring-down spectroscopy**

For broadband CRDS measurements the LIP is generated in the centre of a high-finesse optical cavity, as described above, and the broadband cavity output spectrum is temporally and spectrally monitored with the spectrometer and iCCD

combination described in Section 2.1.1.2. The *ringing-down* of the light that leaks from the cavity can be visualised as a number of spectra with a decreasing intensity over time. These spectra are recorded by varying the delay time of the gated iCCD. Fig. 2.2 shows an example of the time-dependent cavity output spectrum measured in steps of 1  $\mu\text{s}$  from 1.5 to 5.5  $\mu\text{s}$  after plasma formation, along with an example of the time-dependent cavity output decay at 631 nm.

This measurement yields a range of time-dependent intensities,  $I(\lambda, t)$ , measured at each wavelength, which decay exponentially, in the form described by Eq. 2.1, where  $\tau(\lambda)$  represents the *ring-down time*, and  $I_0(\lambda)$  is the cavity output intensity at  $t = 0$ . An appropriate linear regression fit to the natural log of  $I(\lambda, t)$  yields the corresponding cavity ring-down times with the slope of the fit given by  $-\frac{1}{\tau(\lambda)}$  (see Eq. 2.2). Methods of analysis of exponential decays have been extensively reviewed by Istratov and Vyenko [94].

$$I(\lambda, t) = I_0(\lambda) e^{-\frac{t}{\tau(\lambda)}} \quad (2.1)$$

$$\ln [I(\lambda, t)] = \ln [I_0(\lambda)] - \frac{1}{\tau(\lambda)} t \quad (2.2)$$

Through this analysis procedure, absorption spectra are obtained based on measurements with, and without, an absorbing species present in the cavity, according to the analysis procedure outlined in Section 1.1.

This step-wise approach to broadband CRDS is similar to the technique of cavity ring-down spectrography described by Czyzewski et al. [27].

As the ring-down times are determined from a number of independent measurements of the time-dependent cavity output spectrum, each requiring accumulation of a number of plasma pulses so as to improve SNR, CRDS measurements via this approach are inherently slow. For a measurement using an Nd:YAG laser operating at a typical frequency of 10 Hz, the required number of steps through the time-dependent cavity output to yield a satisfactory fit to the data, along with the

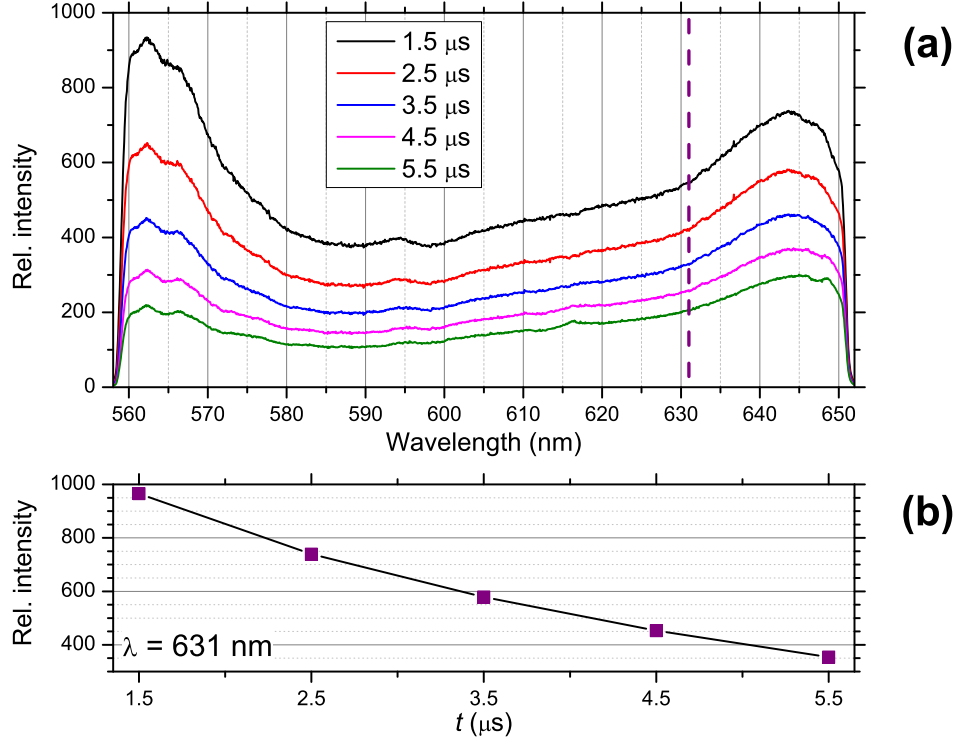


FIGURE 2.2: **(a)** Cavity output spectrum measured for a number of delay times after plasma formation. Each spectrum corresponds to a  $0.5 \mu\text{s}$  gate window accumulated over 500 plasma pulses, yielding a total integration time of  $250 \mu\text{s}$  per spectrum. **(b)** Relative cavity output intensities at  $631 \text{ nm}$  (see dashed purple line in (a)). Ring-down times as a function of wavelength are determined from an appropriate fit to the exponentially decaying cavity output intensity.

necessary accumulations per step (to reduce noise), results in measurement times of many minutes. Consequently, these protracted measurement periods make this method susceptible to any changes in the plasma emission intensity, and generally unsuitable for measurements that require a high time-resolution.

As the cavity output intensity is expectedly 0 after  $50 \mu\text{s}$ , measurements of this nature could in principle be performed at a repetition rate in the kHz range, thus greatly decreasing measurement time. However, practical limitations in achievable pulse energies result in a far lower maximum measurement rate. LIBS measurements have been demonstrated up to a maximum rate of  $100 \text{ Hz}$  [95], albeit using lasers with lower pulse energies than is standard.

## 2.2.2 Incoherent broadband cavity-enhanced absorption spectroscopy

As in the case of broadband CRDS, for IBBCEAS measurements the LIP is generated in the centre of a high-finesse cavity, as shown in Fig. 2.1. While CRDS measurements require the cavity output spectrum to be temporally resolved, for the intensity-dependent IBBCEAS measurements the cavity output spectrum is simply integrated over a large portion of the cavity output decay, as shown in Fig. 2.3. This figure shows the spectrum obtained by integrating the cavity output spectrum from  $1.5 - 10.5 \mu\text{s}$  after plasma formation. Repeating this measurement procedure with an absorbing sample present in the cavity allows an absorption spectrum to be determined based on the standard IBBCEAS analysis outlined in Section 1.2.

In comparison to the step-wise broadband CRDS approach described above, the IBBCEAS method is significantly faster as the cavity output spectrum is measured in one single accumulation. In contrast, the CRDS approach requires that the cavity output spectrum be accumulated  $N$  times, where  $N$  represents the number of data points in the ring-down transient used to determine  $\tau$ . As both approaches are limited to the repetition rate of the LIP formation laser, a CRDS spectrum will take a factor of  $N$  longer to measure than an IBBCEAS spectrum. In addition to this longer measurement time, if each step of the ring-down transient is accumulated over the same number of plasma pulses as the IBBCEAS measurement, it will then suffer from a significantly lower SNR, as a result of the reduced integration times per step. This greatly increased measurement rate renders the IBBCEAS approach more favourable for rapid measurements. The increased integration times yield improved SNRs, although this is at the expense of leaving the measurement system more sensitive to fluctuations in the LIP emission intensity. However, when compared to the CRDS approach, the advantages of the IBBCEAS approach in terms of measurement speed and simplicity come at the expense of the inability to measure absolute absorption coefficients without first determining the cavity mirror reflectivity.

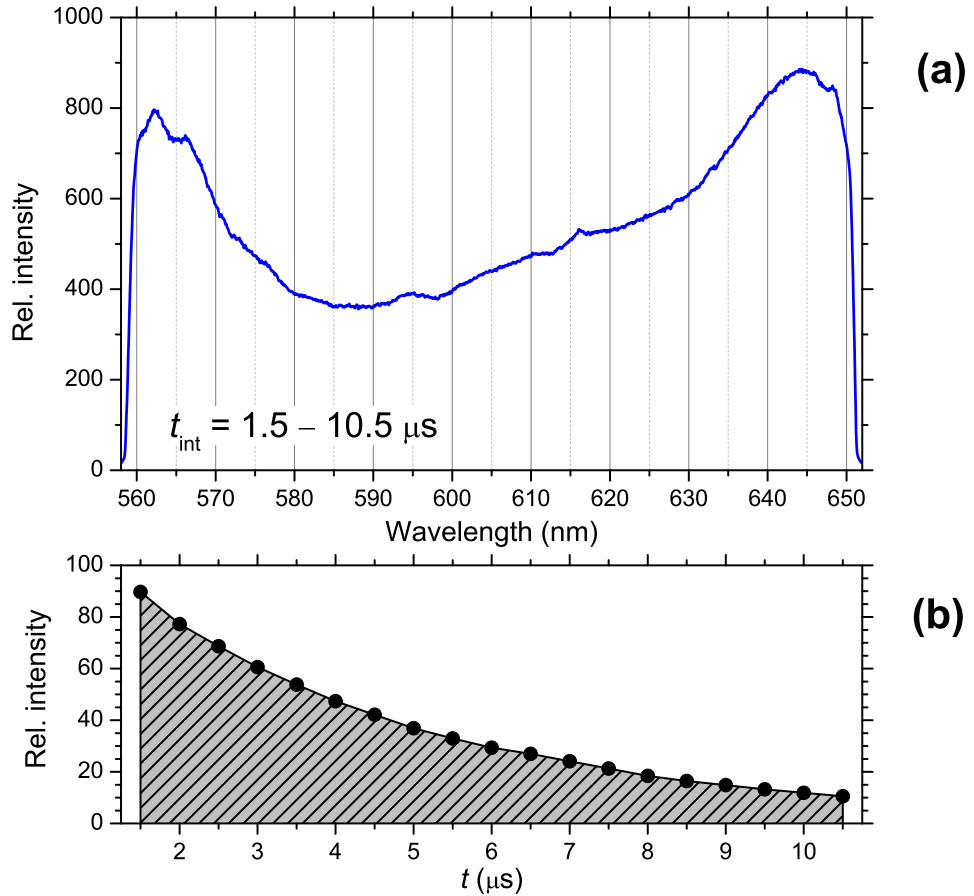


FIGURE 2.3: **(a)** Cavity output spectrum measured by integrating over the cavity output decay from  $1.5 - 10.5 \mu\text{s}$  after plasma formation, accumulated over 500 plasma pulses, yielding a total integration time of 4.5 ms. **(b)** Typical time-dependent cavity output intensity at an arbitrary wavelength. The shading indicates the time range over which the cavity output intensity is integrated to produce the spectrum shown in (a).

## 2.3 Laser-induced plasma formation

It is generally accepted that there are two mechanisms which lead to LIP formation in air: multi-photon ionisation [96], and cascade ionisation [97, 98]. Multi-photon ionisation is the simultaneous absorption, by a neutral atom, of a number of incident photons, the combined energy of which exceed the ionisation potential of the atom. An LIP is then produced through ionisation of a large number of atoms through this mechanism. Alternatively, cascade ionisation is a classical description of the breakdown mechanism in which free electrons gain sufficient energy to ionise atoms through absorption of energy from the electric field of the laser beam

upon elastic collisions with neutral atoms. Upon the ionisation of an atom, more electrons are released, which are then also available for the process to repeat, leading to exponential growth of the electron density. It is accepted that, in general, the multi-photon ionisation process better describes LIP formation at *low* pressures, with ultra-short laser pulses and short wavelengths. Meanwhile, for *higher* pressures, longer wavelengths, and nanosecond-scale pulses, LIP formation is best described by the cascade ionisation mechanism [98–101]. A comprehensive review of the theoretical background to laser-induced gas breakdown has been provided by Smith and Meyerand [102].

The following provides information on the laser-induced breakdown process with the Nd:YAG laser described previously, assuming that cascade ionisation is the dominant LIP formation mechanism. Also included is a brief analysis of the performance of the LIP in terms of the energy-dependence of the LIP emission intensity, along with the overall shot-to-shot stability of the LIP itself. Information on the spectral properties of the LIP will be provided in the next chapter.

### 2.3.1 Laser-induced breakdown process

For the experiments outlined in this thesis, LIPs are generated by way of a fused-silica lens which focuses the pulses from the Nd:YAG laser described above sufficiently so that the energy density is large enough to initiate breakdown of air. Based on the lens focal length of 3 cm, and an estimated laser beam divergence of 1 mrad, the beam is estimated to have a radius,  $r_0$ , of  $\sim 15 \mu\text{m}$  at the lens' focal distance. A short focal length lens was utilised for LIP formation due to the correspondingly smaller beam waist which should contribute to producing a smaller and more intense LIP. The latter is of benefit to the performance of cavity-based spectroscopic measurements.

The typical pulse energy of the Nd:YAG laser,  $E$ , of 55 mJ with a pulse width,  $\Delta t$ , of 10 ns corresponds to a power density,  $I$ , of  $\sim 7.8 \times 10^{11} \text{ W/cm}^2$ , according to Eq. 2.3.

$$I = \frac{E}{\Delta t} \frac{1}{\pi r_0^2} \quad (2.3)$$

By varying the laser pulse energy, LIP formation was found to occur for all laser pulse energies above 24.5 mJ, below which the power density at the focus of the plasma-formation lens is insufficient to consistently produce breakdown of air. Assuming a beam waist of 30  $\mu\text{m}$ , 24.5 mJ corresponds to a power density of  $\sim 3.5 \times 10^{11}$  W/cm<sup>2</sup> at the lens' focal distance, which represents the breakdown threshold,  $I_{\text{BD}}$ . Fig. 2.4 illustrates the expected temporal profile of a laser pulse before and after LIP formation. Plasma formation does not occur prior to the laser intensity reaching the required threshold,  $I_{\text{BD}}$ , as a result, the beginning of the laser pulse with  $I < I_{\text{BD}}$  passes through the plasma formation region and is lost. After this threshold is reached, LIP formation begins and the subsequent light from the laser pulse is absorbed by the increasingly opaque plasma, heating and ionising it.

$$I_{\text{BD}} \text{ (W/cm}^2\text{)} = \frac{8 \times 10^{-10}}{P\lambda^2\Delta t} (1 + 4.5 \times 10^6 P^2\lambda^2) (1 + 2 \times 10^8 \Delta t) \quad (2.4)$$

Eq. 2.4 [103] provides an expression for the breakdown threshold of nitrogen as a function of pressure (in atmospheres),  $P$ , the laser wavelength (in nm),  $\lambda$ , and the pulse duration (in ns), derived from the cascade ionisation theory of plasma formation. For the laser parameters stated above, and treating the laser as operating only at 1064 nm, this equation yields a value for the breakdown threshold of  $\sim 2.1 \times 10^{11}$  W/cm<sup>2</sup>, which agrees reasonably well with the measured value, especially if we allow for the fact that 15% of the laser energy is comprised of light at 532 nm, and that there may be some loss (ca. 5 %) of light at the focusing lens. It should be noted that 24.5 mJ is the lowest measured energy at which all laser pulses produce an LIP. Plasma formation was observed, with a diminishing success rate, for energies as low as 19.5 mJ, which corresponds to a power density of  $\sim 2.75 \times 10^{11}$  W/cm<sup>2</sup>.

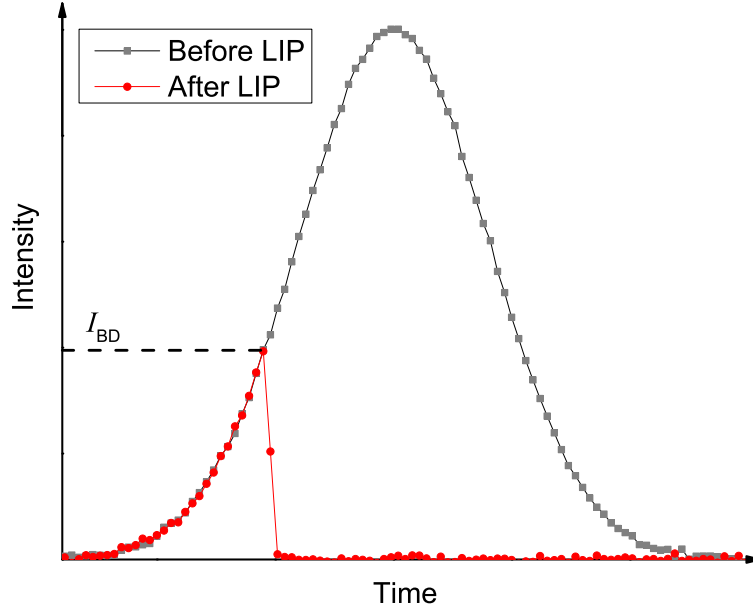


FIGURE 2.4: Illustration of the expected laser pulse intensity before (grey) and after (red) LIP formation, for a pulse with an energy far in excess of the breakdown threshold in air. Breakdown occurs when the laser intensity surpasses the threshold  $I_{BD}$ , after which point the laser energy is absorbed by the LIP.

Difficulties arise when comparing the measured breakdown threshold of ambient air to literature values due to significant variation in the reported values, with a number of studies reporting different values ranging from  $2 \times 10^{10}$  W/cm<sup>2</sup> to approximately  $4 \times 10^{12}$  W/cm<sup>2</sup> for laser-induced breakdown at 1064 nm [56, 104–107]. This variation in reported values is attributed not only to differences in pulse length (which varies from 2.5 to 10 ns in the previously listed studies), but also the dependence of the breakdown threshold on factors including the laser beam quality, beam dimensions, and focal length of the plasma-formation lens. Inconsistencies in the definition of the breakdown threshold also contribute to this uncertainty, with some studies determining the threshold to be as low as the power density that corresponds to a 25% plasma formation success rate [105]. The lowest energy at which LIP formation occurred in this study was 19.5 mJ, corresponding to an energy density of  $2.75 \times 10^{11}$  W/cm<sup>2</sup>. Therefore, depending on the definition employed, the measured breakdown threshold can be taken to be somewhere in



the range of  $(2.75 - 3.5) \times 10^{11}$  W/cm<sup>2</sup>. The work of Armstrong et al. [106], which measured the breakdown threshold of nitrogen (the breakdown threshold of nitrogen is expected to be similar to that of air) using a Nd:YAG laser operating at 1064 nm, with a pulse width of 10 ns, focused through a short focal length lens ( $f = 5.8$  cm), bears the strongest similarity to the experimental conditions in this study, and therefore serves as the best point of comparison. They determined the breakdown threshold to be  $\sim 2.2 \times 10^{11}$  W/cm<sup>2</sup>, which compares quite favourably to both the value measured here, and that determined from Eq. 2.4.

### 2.3.2 Energy-dependence of the LIP emission intensity

As the laser pulse energy increases, the LIP absorbs more and more energy, resulting in an increasing plasma emission intensity with laser energy. The LIP emission spectra for five different laser pulse energies, measured with both a 0 ns, and a 100 ns, delay after LIP formation in ambient air are shown in Fig. 2.5.<sup>3</sup>

Fig. 2.6 shows the relative intensity of the LIP broadband continuum emission in the visible region, immediately after plasma formation (i.e. with a 0 ns delay between LIP formation and data collection), as a function of the laser pulse energy. The uncertainties in these values were taken to be  $\pm 3\%$  ( $x$ -axis), and  $\pm 13\%$  ( $y$ -axis), which represent the laser pulse energy jitter, and the LIP emission intensity jitter (see Fig. 2.9), respectively. The relative intensities shown were determined from an arithmetic mean of 10 individual points across the emission spectrum. The LIP emission intensity is linearly dependent on the laser pulse power above the air breakdown threshold of 24.5 mJ, below which the power density at the focus of the plasma-formation lens is insufficient to consistently cause breakdown of air. For comparison, Fig. 2.7 shows the LIP emission intensity at the same energies, measured 100 ns after plasma formation, with the emission intensities normalised to the same scale as that in Fig. 2.6. Similar to the previous figure,

---

<sup>3</sup> The non-equidistant energy values used in Fig. 2.5 are the result of a small non-linearity between the voltage applied to the laser flash lamps and the energy of the laser emission.

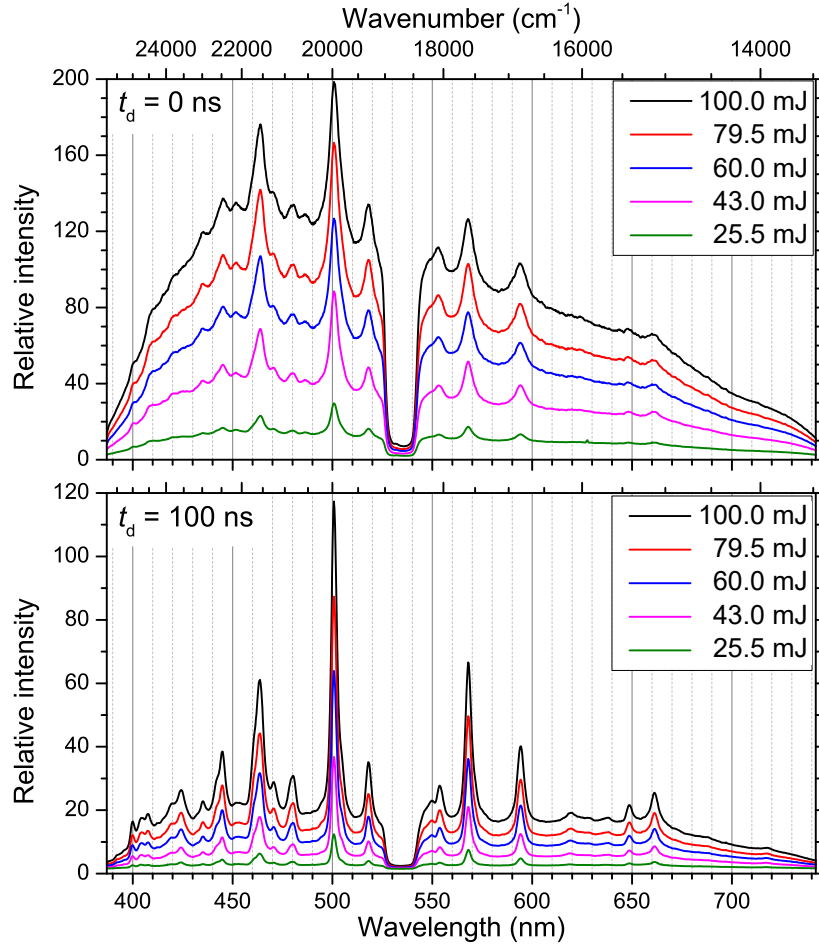


FIGURE 2.5: Energy dependent relative LIP emission spectra in air shown immediately after plasma formation (upper plot), and after a delay of 100 ns (lower plot). Both plots are normalised to the same vertical scale. The dip at  $\sim 535$  nm is due to a notch filter used to protect the detection system from exposure to stray light from the plasma formation laser.

this plot shows a linear relationship between the laser pulse energy and the LIP emission intensity.

By combining the two linear relationships in these plots with the assumption that the broadband continuum emission from the LIP decays mono-exponentially (see Section 3.1.1), estimated values can be calculated for the expected decay constant of the broadband continuum over the first 100 ns after plasma formation, as shown in Fig. 2.8. The values determined here show that, for increasing laser pulse energies in excess of the breakdown threshold of air, the LIP continuum emission decay constant approaches a constant value, i.e. the rate of decay of the LIP emission is largely independent of the laser energy. As the continuum emission intensity is

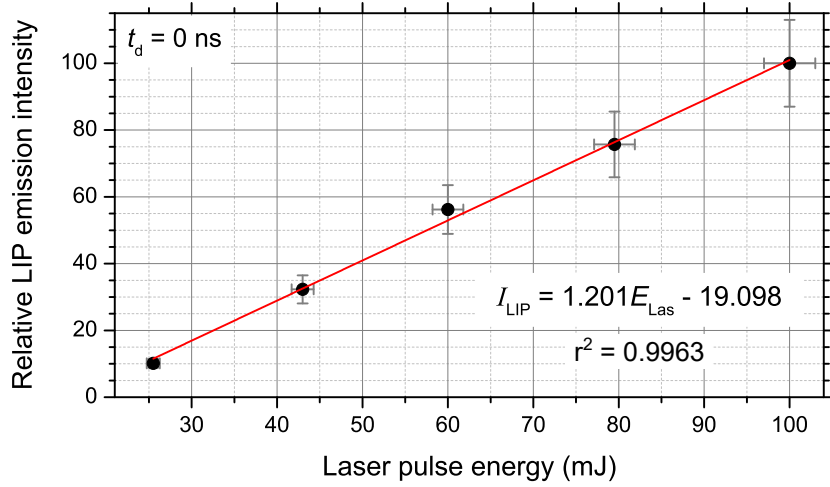


FIGURE 2.6: Relationship between the LIP emission intensity and the laser pulse energy, measured immediately after LIP formation. The LIP emission intensity is normalised to 100 at a pulse energy of 100 mJ. Red: Linear regression fit to the measured data points.

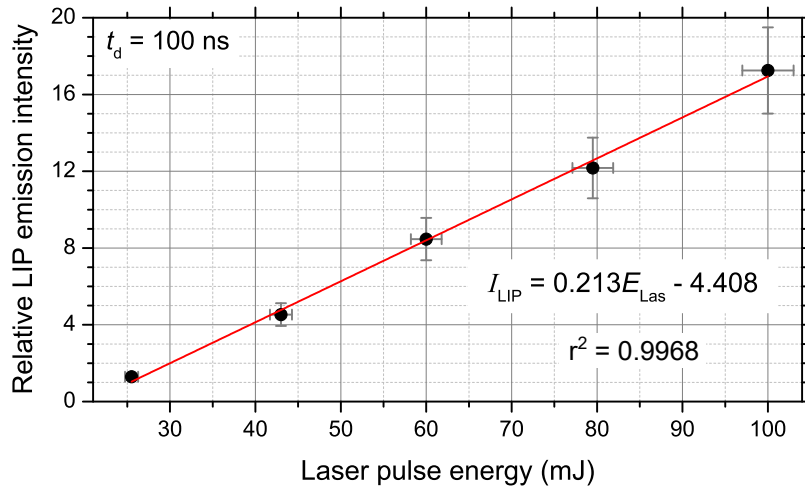


FIGURE 2.7: Relationship between the LIP emission intensity and the laser pulse energy, measured 100 ns after LIP formation. The LIP emission intensity is normalised to the same scale as in Fig. 2.6. Red: Linear regression fit to the measured data points.

expected to be dependent on the LIP temperature, this result is consistent with the work of Yalçın et al. where neither the plasma temperature nor the rate of decay of the plasma temperature were reported to exhibit any dependence on the laser pulse energy [65]. Rather than raising the temperature of the plasma, the excess energy absorbed by the LIP for increasing pulse energies contributes instead to an increased LIP volume [108]. This effect is readily verifiable through visual observations of the physical dimensions of the LIP.

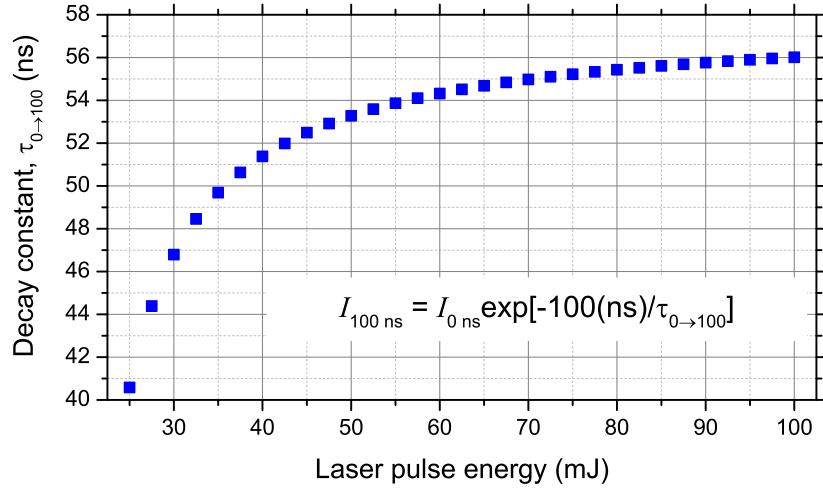


FIGURE 2.8: Calculated exponential decay constant over the first 100 ns after LIP formation, as a function of laser pulse energy, determined from a combination of the two linear relationships presented in Fig. 2.6 and Fig. 2.7.

More details on the spectral properties of the LIP, including the mono-exponential decay of the LIP emission intensity, will be provided in the next chapter.

While the lifetime of the broadband continuum emission remains largely constant with increasing energy, the absolute emission intensity can increase by a substantial amount for relatively large increases in pulse energy. This results in the continuum emission being present in the plasma spectral output for increasing lengths of time as the energy increases. This may present a source of complication in experiments that utilise the LIP continuum emission as a light source, as the “switching off” time of the light source is increased. However, this is not expected to present an issue for the experiments presented in this thesis as cavity based absorption measurements which use the LIP as a light source typically require a delay of  $> 1 \mu\text{s}$  between LIP formation and commencement of data collection (see Chapter 4); well in excess of the LIP emission lifetime.

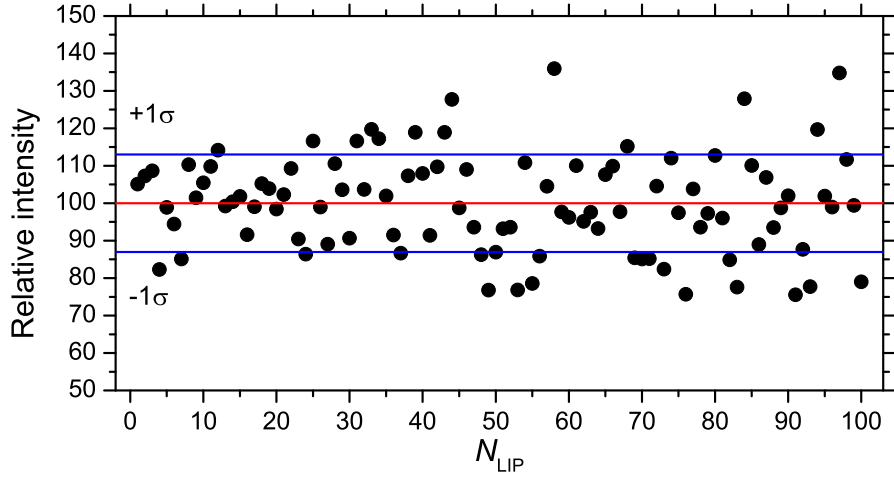


FIGURE 2.9: Relative LIP emission intensity measured for 100 consecutive plasma excitations for a laser pulse energy of 55 mJ, showing the LIP emission jitter around the mean, which is normalised to 100 (red line). The blue lines indicate  $\pm 1$  standard deviation ( $\sigma$ ) around the mean.

### 2.3.3 Laser-induced plasma emission stability

Fig. 2.9 shows the relative emission intensity for 100 consecutive LIPs, formed with a laser pulse energy of 55 mJ, measured immediately after plasma formation, indicating the shot-to-shot jitter between them. The intensity scale in Fig. 2.9 has been normalised such that the mean intensity is equal to 100 (arbitrary units), indicated by the red line in the plot. The blue lines indicate  $\pm 1$  standard deviation in the LIP intensity around the mean intensity. This corresponds to  $\pm 13\%$ , and this value has been taken to represent the jitter in the LIP emission intensity. While there are fluctuations of the order of 3% in the laser pulse energy, fluctuations of this scale would, according to the relationship in Fig. 2.6, result in only a  $< 4\%$  variation in the LIP emission intensity. The larger than expected variance in the LIP emission intensity is assumed to largely be a consequence of variations in the local conditions of the plasma formation region, including pressure and temperature, with the presence of aerosols in the ambient lab air also being significant [66]. Additionally, any lateral movement of the LIP with respect to the imaging optics would result in a variation in the intensity measured by the detection system without any actual change the LIP emission intensity.

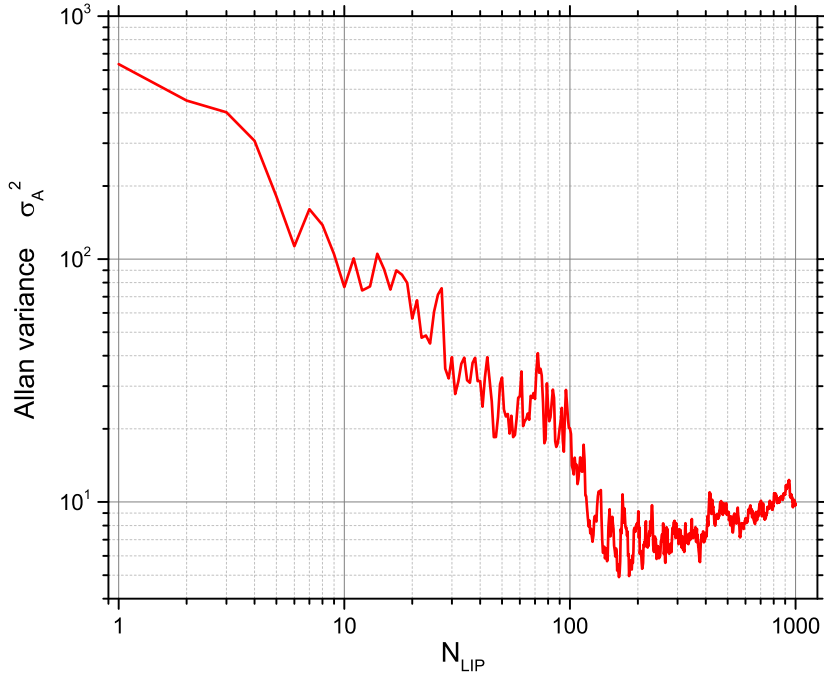


FIGURE 2.10: Allan variance plot for the LIP emission intensity.  $N_{\text{LIP}}$  represents the number of sequential plasma excitations over which the measured intensity has been accumulated.

As a result of the relatively large variation in the LIP emission intensity it is generally necessary to accumulate the emission over a number of individual plasma pulses so as to improve the measurement precision, while also taking account of any potential systematic errors inherent to the setup, including laser pulse energy, and ambient conditions. Fig. 2.10 shows an Allan variance<sup>4</sup> ( $\sigma_A^2$ ) plot [109, 110] for the LIP emission intensity, calculated as a function of the number of individual plasma pulses that the measured intensity is accumulated over,  $N_{\text{LIP}}$ , varying from 1 to 1000 plasma pulses. This plot indicates that the optimum number of plasma pulses to accumulate over is in the range of approximately 200 – 400, before systematic errors in the system (e.g. laser pulse energy drift) start to contribute to an increased overall variance in the measured signal.

The time-dependent change in laser pulse power, and hence, LIP emission intensity, after powering on of the laser is shown in Fig. 2.11. The figure illustrates that the laser requires approximately 2 hours to reach a steady output, during which time

<sup>4</sup>  $\sigma_A^2 = \frac{1}{2} \langle (y_{(n+1)} - y_n)^2 \rangle$ , where  $y_n$  represents the  $n$ th average of a time-series data measurement.

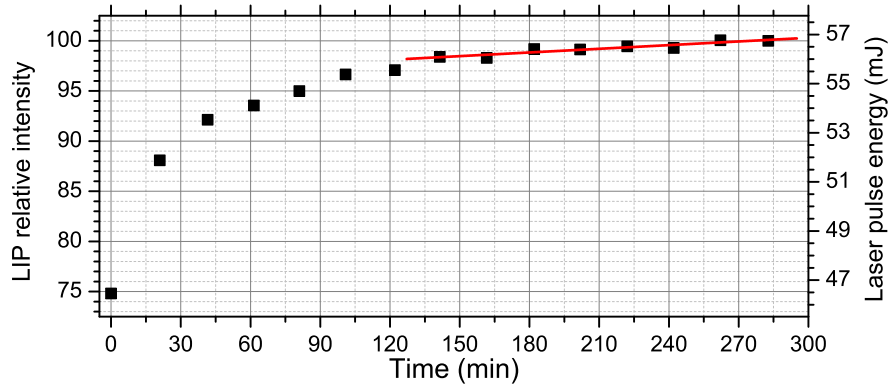


FIGURE 2.11: Relative LIP emission intensity over time, from the point at which the laser is powered on, recorded immediately after plasma formation. The red line indicates the general upward trend in the LIP emission intensity from  $\sim 140$  min onwards.

the sizeable drift in LIP emission intensity would have significant adverse effects on the precision of absorption measurements. Once the required waiting time has elapsed the plasma emission possesses a reasonable degree of stability, although there still exists a small upward trend of  $\sim 0.75\%$  per hour (indicated by the red line in Fig. 2.11). An intensity drift of this scale is not significant within the error limit of the measurements, but it should still be considered as a potential loss of precision when assuming a constant LIP emission intensity.

## 2.4 LIP-induced non-linear refractive index change

The following section provides a description of the experimental approach used to investigate the effect that an LIP has on the propagation of light through or near the plasma formation region.

It should be noted that the purpose of the experiment described is purely qualitative; to determine the effect that an LIP has on the propagation of light, which is important for understanding the observed time-dependence of the intensity of the light leaking from optical cavities (see Chapter 5).

### 2.4.1 Experimental setup

Fig. 2.12 shows a schematic of the experimental setup used to investigate the non-linear refractive index change induced by the LIP, and the effect it has on the propagation of light through/near the plasma formation region. In this case, the beam from a helium-neon (He-Ne) laser ( $\lambda = 632.8$  nm) was focused by a lens ( $f = 30$  mm) through the LIP, with the lens positioned such that the distance between the lens and LIP,  $d_{LP}$ , was less than  $f$ , ensuring that the He-Ne laser probe beam is still converging upon encountering the LIP. The probe beam is incident upon a  $200$   $\mu\text{m}$  pinhole. The time-dependent intensity of the light that is transmitted through the pinhole was monitored with the same detection system described in Section 2.1.1.2. The amount of light transmitted through the pinhole depends on the radius of the expanding probe beam where it reaches the pinhole. A small/large beam radius corresponds to a high/low transmission through the pinhole. This approach to measure non-linear refractive index changes differs from the probe beam deflection method in which the expansion of an LIP is studied based on the direct deflection of a probe beam which travels adjacent to the LIP [111–113].

The LIP, generated as previously described, acts to deviate the probe beam that travels through/near it via a localised refractive index change which arises from the high temperatures and intense electric field around the LIP. In this manner, the LIP produces a negative lensing effect which results in a change in the probe beam radius at the pinhole, and thus, a change in the detected intensity of light transmitted through the pinhole. For a lens-plasma distance,  $d_{LP}$ , less than the focal length,  $f$ , of the probe lens ( $L_2$  in Fig. 2.12), this negative lensing effect acts to lower the divergence of the probe beam, leading to an increased transmitted intensity at the pinhole. Similarly, in the case of  $d_{LP} > f$ , this negative lensing effect would act to increase the divergence of the probe beam, yielding a decreased pinhole intensity. As the plasma expands and cools, the induced refractive index change diminishes, allowing the probe beam to propagate freely again with the beam radius at the pinhole returning to its original size. By measuring



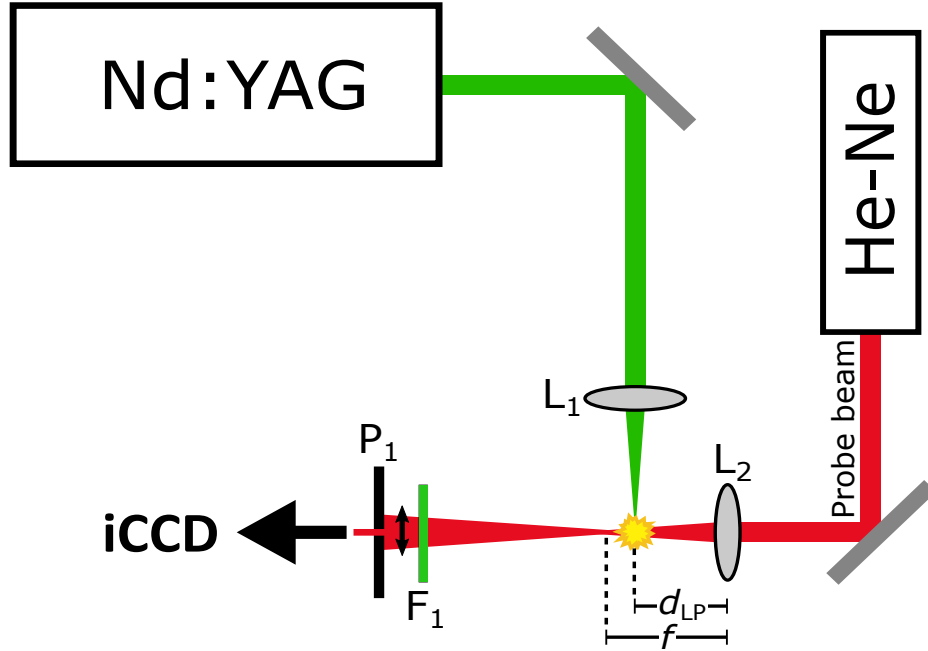


FIGURE 2.12: Schematic of experimental setup used to investigate the non-linear refractive index effects of the LIP. A probe beam from a He-Ne laser is focused through the LIP (generated as described above) by the lens  $L_2$  ( $f = 3$  cm) such that the lens-plasma distance,  $d_{LP}$  is less than the focal length,  $f$ , of the lens. The transmitted probe beam is imaged onto a  $200 \mu\text{m}$  pinhole,  $P_1$ , and the time-varying intensity through the pinhole is monitored with the spectrometer and iCCD previously described.

the transmission through the pinhole, as a function of time, using the iCCD, the time-dependence of the effect of the LIP on light propagation can be monitored. However, along with acting to focus/defocus the probe beam, the LIP also absorbs a significant fraction of the light due to its blackbody properties. Hence, the detected signal is affected by a combination of both the time-dependent focusing of the probe beam, and the time-varying absorption, which makes the interpretation of the results in terms of the refractive index change a formidable task. A description of how the observed effects of the LIP on the propagation of light should be interpreted is provided in Section 5.2.

## 2.5 Conclusion

A description of the experimental setup, including all apparatus, used for the CEAS experiments presented in this thesis was provided in the chapter. This

was followed by an outline of how the use of LIPs as intra-cavity light sources was applied to both time-dependent (CRDS) and intensity-dependent (IBBCEAS) cavity-enhanced absorption spectroscopy.

A description has been provided of the LIP formation process with the pulsed Nd:YAG laser, and the measured power density of the laser pulse ( $\sim 7.8 \times 10^{11} \text{ W/cm}^2$ ) was compared to literature values for the breakdown threshold of air.

The suitability of the LIP as a light source for CEAS was discussed in terms of the stability of the LIP emission. The overall shot-to-shot stability of the emission from the LIP was found to be  $\pm 13\%$ .

Finally, a description of the experimental approach to investigate the time-varying effects of the LIP on the propagation of light was provided.

The next chapter will provide an analysis of the broadband spectral properties of the laser-induced plasma emission along with a description of the graphical approach to determining the LIP temperature, values of which are relevant to the spectral properties of the LIP.

## Chapter 3

# Spectral properties of laser-induced plasmas

The following chapter provides a description of the spectral properties of the laser-induced plasma emission and how the emission spectrum evolves over time. Section 3.1 provides details of the broadband continuum emission from the LIP, with this aspect of the LIP emission being of most relevance to the use of the LIP as a light source for CEAS measurements. Particular attention is paid to how the continuum emission evolves over time after plasma formation. The time-dependent decay of the LIP emission exhibits a spectral-dependence which arises from the time-varying spectral profile of the LIP continuum emission as the plasma cools. This temperature-dependent, time-varying emission profile, which has implications for the measurement baseline of intensity-dependent absorption measurements, is characterised in Section 3.1.2.

Section 3.2 outlines the method of determining the plasma temperature through the use of a graphical approach which relates the relative intensities of a number of emission lines in the LIP spectrum to the temperature of the LIP. This process is then applied to the emission spectra of the LIP used in this study, yielding a description of the temporal evolution of the LIP temperature, and providing the temperature values which are used in Section 3.1.2.

## 3.1 LIP spectral properties

### 3.1.1 Time-resolved LIP emission spectra

Fig. 3.1 shows the broadband LIP emission spectrum, measured with the 150 lines/mm spectrometer grating ( $\Delta\lambda = 1.56$  nm), in steps of 50 ns up to 200 ns after plasma formation. This figure illustrates the early stages of the LIP lifetime, in which the emission spectrum rapidly transitions from a strong broadband continuum emission to a number of ionic and atomic emission lines overlaid upon a weaker broadband emission. The spectra shown here have not been corrected for the wavelength-dependent sensitivity of the iCCD, and hence the reduced intensities for  $\lambda < 450$  nm and  $\lambda > 700$  nm are a consequence of the lower quantum yield of the detector in these spectral regions. The true broadband emission from the LIP stretches deep into the ultraviolet and into the infrared. The dip in the spectra at  $\sim 535$  nm is due to a notch filter that is placed in front of the detector fibre bundle to protect the detector from any possible exposure to stray light from the plasma formation laser (2nd harmonic of the Nd:YAG laser at  $\lambda = 532$  nm).

Also shown in Fig. 3.1 is the result of a broadband mono-exponential fit to the decaying emission spectra, yielding the characteristic exponential decay constant, or lifetime, of the LIP emission at each wavelength. It can be seen that the lifetime of the continuum emission ranges from 60 – 80 ns, while at wavelength corresponding to strong emission lines an increased lifetime is observed. While these regions would, in principle, be better described by a bi-exponential process, fitting of emission line decays in this manner is not straight forward and a mono-exponential fit was found to provide a reasonably accurate estimate of the overall decay constant. This was verified by the broadly constant coefficient of determination,  $r^2$ , values for the fit across the full spectral range. It should be noted that in the case of the data shown here, the spectrum for 0 – 50 ns after plasma formation was excluded from the fit due to erroneous results in the regions with strong emission lines. For example, the emission line around 500 nm, shows a higher intensity from

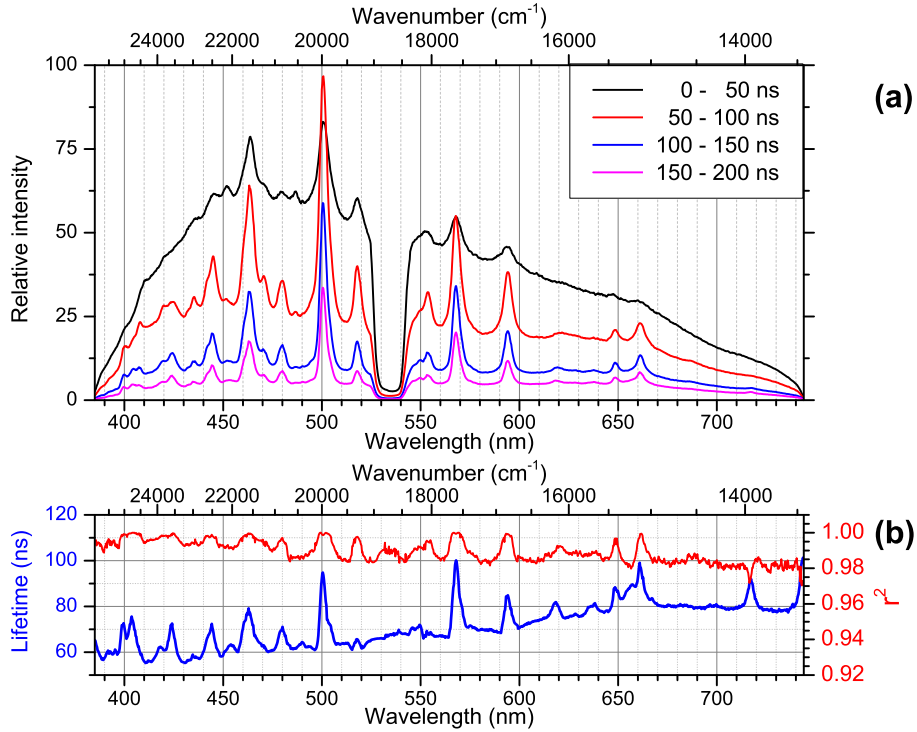


FIGURE 3.1: **(a)** LIP emission spectrum shown in steps of 50 ns, from 0 to 200 ns after plasma formation. The dip at  $\sim 535$  nm is due to a notch filter to protect the detection system from stray laser light. **(b)** Blue: Broadband LIP emission decay lifetime determined from a mono-exponential fit to the decaying spectra shown in (a) above. Red:  $r^2$ -values for the mono-exponential fit.

50 – 100 ns, than from 0 – 50 ns. This increase in intensity is likely a consequence of the plasma ionisation process having not fully come to completion until after the first spectrum is recorded. Fitting including the first spectrum yields broadly similar results for the underlying decay constant corresponding to the continuum decay, but grossly overestimates the lifetimes of emission lines with very poor fitting quality (e.g.  $r^2 \sim 0.45$  around the emission peak at 500 nm).

For longer delay times after LIP formation, the emission continues to decay approximately mono-exponentially, however at a different rate than for the early stages of the LIP emission. Fig. 3.2 shows the measured LIP emission for delay times of 750 ns, 1000 ns, and 1250 ns after plasma formation. The spectra measured at these delay times exhibit an emission intensity that is 2 orders of magnitude smaller compared to those shown in Fig. 3.1. The decay lifetime of approximately 600 ns, determined from a mono-exponential fit to the spectra, is greatly increased. The difference in decay rate between short and long delay times

is likely the consequence of a combination of the rapid cooling and expansion of the LIP that occurs within the first 100 – 200 ns after plasma formation (see Section 1.3). The time-dependent LIP emission intensity from 0 to 1750 ns after plasma formation, measured at 631 nm, is shown in a semi-logarithmic plot in Fig. 3.3. The two regions corresponding to the fits in Fig. 3.1 and Fig. 3.2 are indicated by straight lines (blue and red respectively) in Fig. 3.3. The wavelength of 631 nm was arbitrarily chosen due to a lack of any noticeable emission lines from the plasma in this region. The time-dependent emission of the plasma throughout its entire lifetime is evidently not well described by one mono-exponential decay, with the emission at short and long delay times characterised by two different exponential decays. The different behaviour between short and long delay times is attributed to contributions from other processes in the plasma expansion and cooling, which in turn affects the plasma emission intensity. In particular, at short delay times ( $t \lesssim 0.5 \mu\text{s}$ ), the rapid plasma expansion as a 3-dimensional shock wave leads to a rapidly decreasing temperature, while at later times radiative cooling is the dominant process [114]. Despite the presence of other cooling processes, mono-exponential decays were found to, within the scope of this work, adequately describe the temporal dependence of the plasma emission intensity.

### 3.1.2 Temporal evolution of the LIP broadband continuum emission

From Fig. 3.1(b) it can be seen that the measured lifetime of the LIP emission (blue trace) exhibits a wavelength-dependent increase to longer wavelengths, from approximately 60 ns at  $\lambda \approx 400$  nm to approximately 80 ns for  $\lambda > 650$  nm. The quality of the fit used to determine the decay lifetime ( $r^2$ , red trace) also displays a corresponding slight decrease for longer wavelengths. It is surmised that this is a consequence of the blackbody emission maximum of the LIP shifting to longer wavelengths as the plasma cools, in accordance with Wien’s displacement law (See Eq. 3.2). The blackbody emission spectral radiance,  $B_\lambda(\lambda, T)$ , at a temperature  $T$ , is described by Planck’s law.

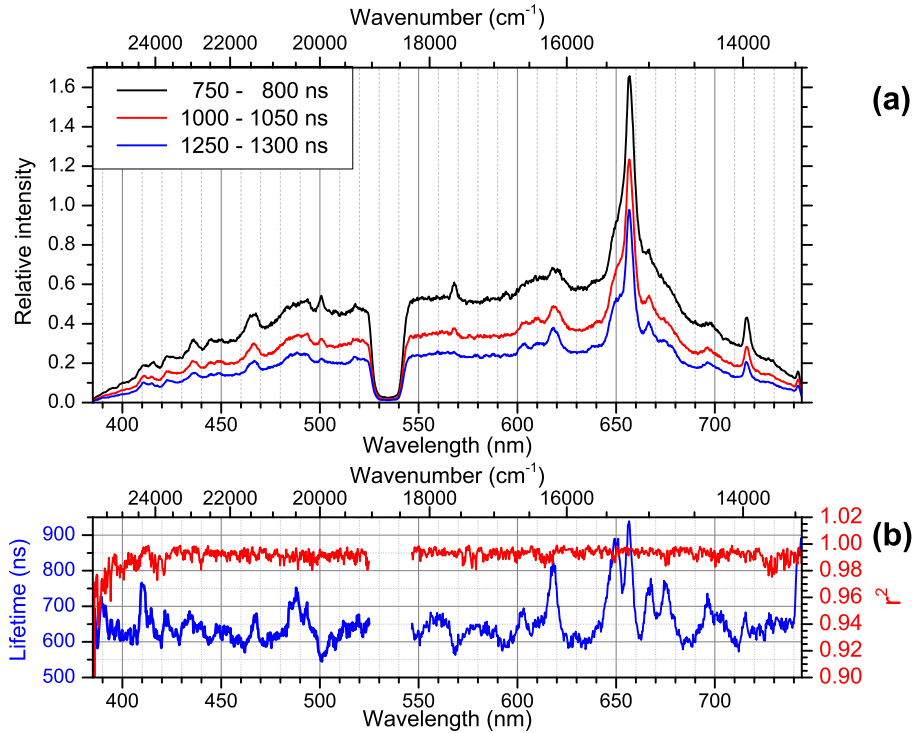


FIGURE 3.2: **(a)** LIP emission spectrum measured for delay times of 750 ns, 1000 ns, and 1250 ns after plasma formation. The dip at  $\sim 535$  nm is due to a notch filter used to protect the detection system from stray laser light. **(b)** Blue: Broadband LIP emission decay lifetime determined from a mono-exponential fit to the spectra shown above. Red:  $r^2$ -values for the mono-exponential fit.

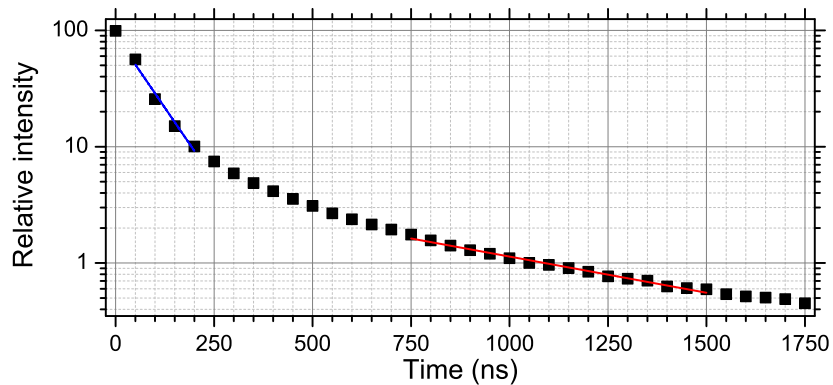


FIGURE 3.3: Semi-logarithmic plot of the relative LIP emission intensity from 0 – 1750 ns after plasma formation, measured at a wavelength of 631 nm. The blue and red lines indicate the time regions which were used to determine the LIP emission decay constants shown in Fig. 3.1 and Fig. 3.2, respectively.

$$B_{\lambda}(\lambda, T) = \frac{2hc^2}{\lambda^5} \frac{1}{\exp\left[\frac{hc}{\lambda k_B T}\right] - 1} \quad (3.1)$$

where  $h$  is the Planck constant,  $c$  is the speed of light, and  $k_B$  represents the Boltzmann constant. A blackbody emitting according to Planck's law has a maximum emission intensity at a wavelength  $\lambda_{\max}$ , which can be calculated according to:

$$\lambda_{\max} = \frac{2.8978 \times 10^{-3} \text{ [m K]}}{T} \quad (3.2)$$

Although the plasma emission is not fully described by Planck's law (particularly at short delay times when collisional processes dominate), approximating the broadband continuum emission of the LIP to be described by Planck's law provides a rough description of the temporal evolution of the broadband emission. Based on this description, the emission spectrum decreases in intensity and the emission maximum shifts to longer wavelengths as the plasma cools. This results in the emission seemingly decaying faster (smaller decay constant) at shorter wavelengths, and slower (larger decay constant) at longer wavelengths.

Based on the relative intensities of the emission lines present in the LIP spectra, the plasma temperature can be estimated to be approximately 51300 K and 34750 K, at 50 ns and 200 ns, after plasma formation, respectively. A detailed description of the method used to determine the LIP temperature will be provided in Section 3.2. Fig. 3.4 shows the theoretical blackbody emission spectrum at each of these temperatures, along with the maximum emissions at  $\sim 56.5$  nm and  $\sim 83$  nm, according to Eq. 3.2. Also shown is the ratio of these two spectra within the spectral range of the detection system, which illustrates the more significant change in the blackbody emission intensity at shorter wavelengths.

This behaviour is further illustrated in Fig. 3.5 which shows the expected wavelength-dependent continuum decay constant,  $\tau$ , (red trace) for a mono-exponential decay from the theoretical blackbody spectrum at  $t = 0$  s, to that at  $t = 1250$  s, where the temperature at each point is determined as described



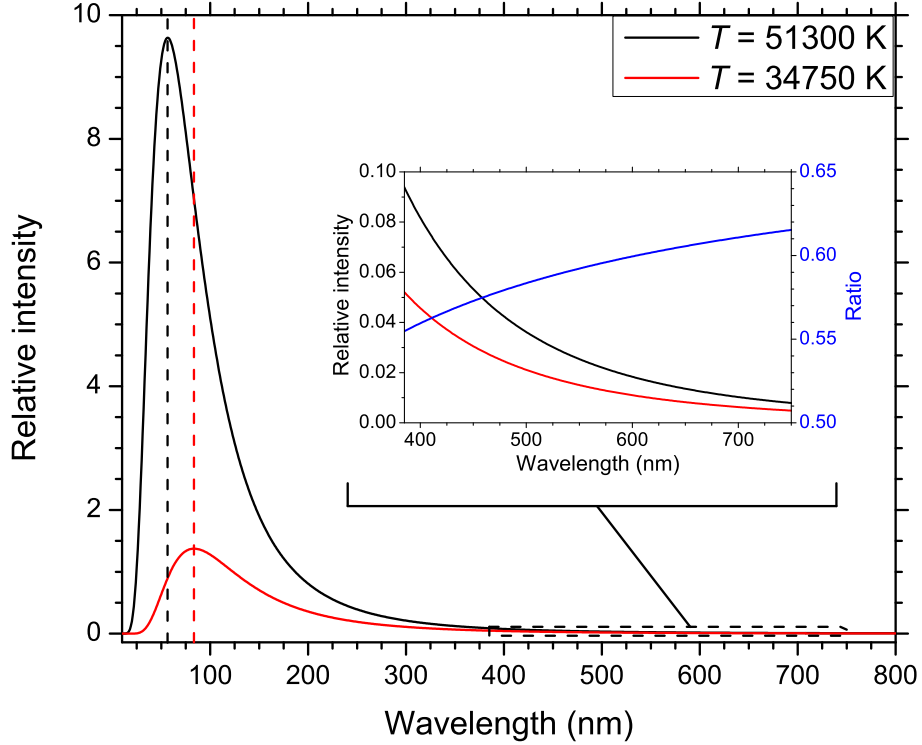


FIGURE 3.4: Blackbody emission spectra, calculated from Eq. 3.1, for  $T = 51300$  K and  $34750$  K, which correspond to radiation temperatures  $50$  ns and  $200$  ns after plasma formation, respectively. The inset shows an expanded view of the region corresponding to the spectral range of the detector used for CEAS measurements, with the blue trace representing the ratio between the two spectra.

below. This is shown along with the measured broadband decay lifetime (black trace) from Fig. 3.1, which has been normalised and scaled such that both spectra shown in Fig. 3.5 are equal at a wavelength of  $610$  nm, for ease of comparison. While the measured decay of the LIP emission was found to be much faster than that predicted by an exponential decay of the idealised blackbody emission spectra ( $\tau \approx 75$  ns, compared to  $\tau \approx 290$  ns), the two spectra show the same behaviour, with similar relative increases in the wavelength-dependent decay constants across the spectral range. The discrepancy between the rate of decay of the measured LIP emission and that expected from Planck's law can be attributed both to alternative energy loss mechanisms of the LIP, and to the changing LIP dimensions over time. In particular, as the LIP expands, the detector collection efficiency of

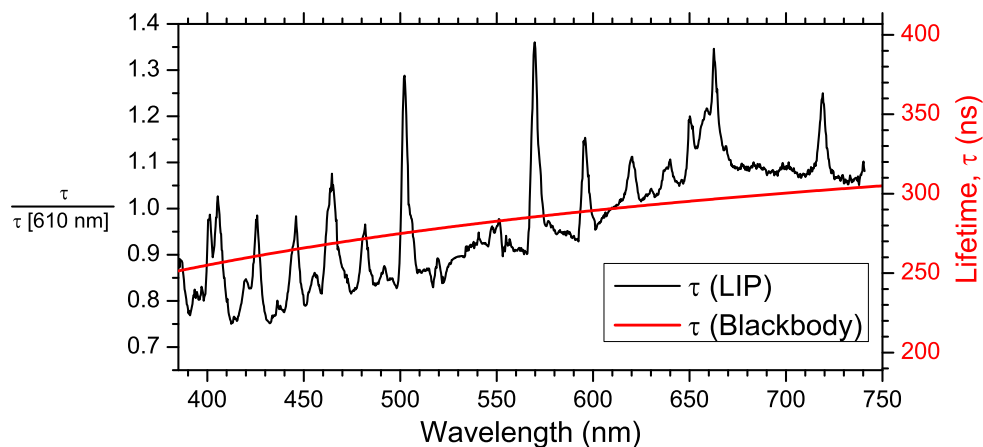


FIGURE 3.5: Red: Exponential decay lifetime between the two simulated blackbody emission spectra shown in Fig. 3.4. Black: Decay lifetime of the measured LIP emission spectra showing the relative increase in the lifetime across the spectral range. To facilitate a comparison of the spectral dependence, the black spectrum has been normalised and scaled so that both spectra are equal at a wavelength of 610 nm.

the optical emission will decrease, which contributes to the measured decay of the emission intensity and introduces an exponential bias.

The greater change in emission intensity from the LIP at shorter wavelengths for any change in plasma temperature has implications for the baseline correction for cavity based absorption measurements using the LIP as a light source. For IBBCEAS measurements, any change in the LIP temperature between the  $I_0(\lambda)$  and  $I(\lambda)$  measurements will produce a wavelength-dependent offset in the measured absorption. This effect is of less concern for CRDS measurements which are generally insensitive to changes of the light source intensity. The effect on the IBBCEAS absorption baseline is presented in Section 4.4.2.

## 3.2 Determination of the LIP temperature

The following provides a description of the approach used to measure the LIP temperature based on the relative intensities of emission lines from the LIP. This approach is then applied to the LIP used in this study to determine its temporal

evolution, and to justify the temperature values which were used in the previous section.

### 3.2.1 Boltzmann analysis of the LIP temperature

Each line in an LIP emission spectrum corresponds to a transition from an excited state of one of the constituents of the plasma medium; mostly singly ionised or neutral atomic nitrogen and oxygen in the case of LIP formation in air. The integrated intensities of these emission lines are proportional to the population of the excited state, and hence, plasma temperature, according to the Boltzmann distribution, provided that the plasma is in local thermodynamic equilibrium. Based on the measured intensities of a number of emission lines from the same ionisation state, the LIP temperature can be determined using a graphical approach which relates the weighted line intensities to the excited-state energy according to the temperature [65, 115]. A description of this analysis procedure, which is termed the *Boltzmann plot method*, is outlined below.

For a given transition,  $k \rightarrow i$ , at an energy  $E_k$ , the mean population of the excited state,  $\langle n_k \rangle$ , is related to the temperature,  $T$ , according to Eq. 3.3:

$$\langle n_k \rangle = \frac{n_0 g_k}{Z(T)} \exp \left[ -\frac{E_k}{k_B T} \right] \quad (3.3)$$

where  $n_0$  represents the total number density,  $k_B$  is the Boltzmann constant,  $g_k$  is the statistical weight of the upper state, and  $Z(T)$  is the partition function:

$$Z(T) = \sum_j g_j \exp \left[ -\frac{E_j}{k_B T} \right] \quad (3.4)$$

The emission intensity,  $I_{k \rightarrow i}$ , at a wavelength  $\lambda$ , from this transition is related to the excited-state population and the corresponding transition probability (Einstein coefficient),  $A_{k \rightarrow i}$ , as described by Eq. 3.5, where  $h$  and  $c$  represent the Planck constant, and the speed of light, respectively.

$$I_{k \rightarrow i} = \frac{n_k A_{k \rightarrow i} h c}{\lambda} \quad (3.5)$$

The ratio of the emission intensities of two different transitions from the same ionisation state of a species yields a relationship (see Eq. 3.6) to the plasma temperature,  $T$ , which is dependent only on the known quantities  $A_{k \rightarrow i}$ ,  $g_k$ ,  $E_k$ , and the transition wavelength,  $\lambda$ . The values for each of these are available from the National Institute of Standards and Technology (NIST) Atomic Spectra Database (ASD) [116].

$$\frac{I_1}{I_2} = \frac{A_{k \rightarrow i,1} g_{k,1} \lambda_2}{A_{k \rightarrow i,2} g_{k,2} \lambda_1} \exp \left[ -\frac{E_{k,1} - E_{k,2}}{k_B T} \right] \quad (3.6)$$

Rearranging and taking the natural logarithm of each side of Eq. 3.6 yields a linear relationship between the difference in the excited-state energies ( $E_{k,1} - E_{k,2}$ ), and the difference between the weighted emission intensities:

$$\ln \left[ \frac{\lambda_1 I_1}{A_{k \rightarrow i,1} g_{k,1}} \right] - \ln \left[ \frac{\lambda_2 I_2}{A_{k \rightarrow i,2} g_{k,2}} \right] = -\frac{E_{k,1} - E_{k,2}}{k_B T} \quad (3.7)$$

Taking a number of emission lines and plotting their weighted emission intensities ( $\ln [\lambda I / A_{k \rightarrow i} g_k]$ ) as a function of the excited-state energy produces a linear distribution. A fit to this distribution yields a slope of  $-1/k_B T$ , thus providing a value for the LIP temperature,  $T$ . Use of this graphical approach, rather than simply solving Eq. 3.7 for a number of pairs of emission lines, has the advantage of improving the accuracy of the temperature calculation, as well as allowing easy identification of incorrectly assigned emission lines through the presence of obvious outliers from the linear relationship.

### 3.2.2 Temporal evolution of the LIP temperature

To measure the temperature of the LIP its emission was recorded with the detection spectrometer and iCCD in steps of 50 ns from immediately after plasma

formation up to a delay time of 1250 ns after plasma formation. Spectra were recorded using the low resolution spectrometer grating (150 lines/mm), giving a resolution of 1.56 nm with considerable spectral coverage (390 – 740 nm), allowing simultaneous detection of  $\sim 20$  emission lines. Table 3.1 lists the singly ionised nitrogen (N II) lines identified in the plasma emission which were used to determine the plasma temperature via the Boltzmann plot method, along with the relevant quantities required to calculate the temperature. All quantities have been retrieved from the NIST ASD [116]. The positions of these lines are indicated by the black numerals (1 – 7) in Fig. 3.6, which shows the LIP emission spectrum measured 150 ns after plasma formation. The line emission intensities,  $I$ , used in the temperature calculation are determined by integrating the identified emission lines after first removing the continuum emission background which is folded with the spectral sensitivity curve of the iCCD (see red-dashed line in Fig. 3.6). While there is clearly a large number of emission lines in Fig. 3.6 that have not been used for the temperature measurement this is due to some lines producing erroneous results due to incorrect measurements of the line area. Incorrectly determined line areas generally arise as a result of overlapping emission lines which cannot be distinguished due to the rather low resolution of the measured spectra. An example of such a case is indicated in Fig. 3.6 by the green  $\times$  at  $\sim 444$  nm. The error in the integrated area of this line originates from a rather large number ( $> 20$ ) of relatively strong emission lines from singly ionised oxygen (O II) in the spectral region of 439 – 449 nm. The graphical approach to determining the temperature makes it very easy to identify these erroneous values as significant outliers in the data. While it would in principle be possible to reduce or eliminate these errors by fitting multiple Gaussian functions to these bands to determine the area of each of the composite emission lines, this has the potential to introduce further error, and was deemed not to be necessary in this case due to the sufficient number of usable lines identified.

Fig. 3.7 shows an example of the “Boltzmann plot method” used to determine the LIP temperature at a delay time of 150 ns after LIP formation, according to the analysis described in Section 3.2.1. This plot shows the points corresponding

Line	$\lambda$ (nm)	$A_{k \rightarrow i}$ ( $10^7 \text{s}^{-1}$ )	$g_k$	$E_k$ ( $\text{cm}^{-1}$ )	$E_k$ ( $10^{-18}$ J)
1	463.054	7.48	5	170666.23	3.38994
2	500.515	11.4	9	186652.49	3.70748
3	553.536	6.04	9	223785.51	4.44505
4	567.956	4.96	7	166678.94	3.31074
5	594.165	5.47	7	187491.90	3.72415
6	648.205	2.58	3	164610.76	3.26966
7	661.056	6.01	7	189335.16	3.76076

TABLE 3.1: Relevant quantities for the singly ionised nitrogen (N II) lines used to determine the LIP temperature. All data has been retrieved from the NIST ASD [116].

Line	$\lambda$ (nm)	$A_{k \rightarrow i}$ ( $10^7 \text{s}^{-1}$ )	$g_k$	$E_k$ ( $\text{cm}^{-1}$ )	$E_k$ ( $10^{-18}$ J)
8	615.819	0.762	9	102865.51	2.04322
9	715.670	5.05	5	116631.09	2.31664

TABLE 3.2: Relevant quantities for the neutral oxygen (O I) lines used to determine the LIP temperature. All data has been retrieved from the NIST ASD [116].

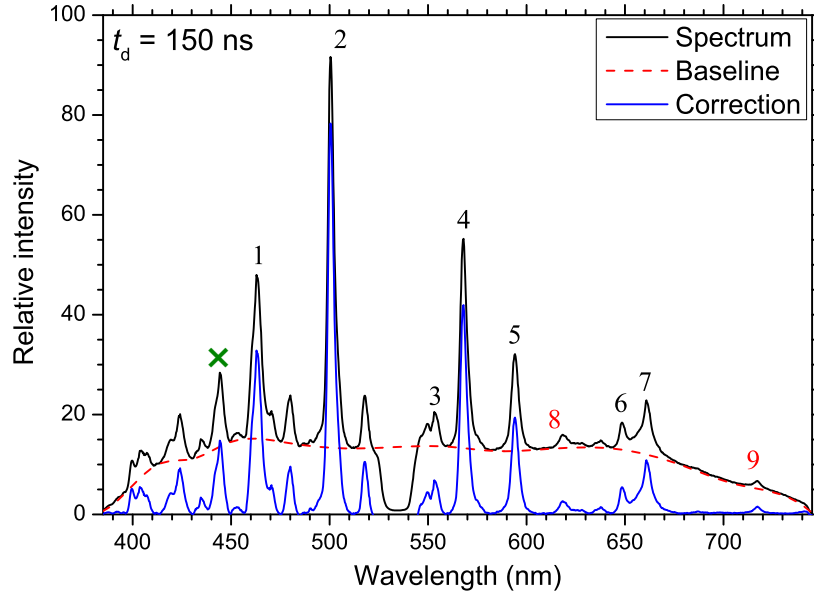


FIGURE 3.6: LIP emission spectrum 150 ns after plasma formation, before (black) and after (blue) subtraction of the broadband continuum background (red-dashed). The numbers indicate the positions of the singly ionised nitrogen (black), and neutral oxygen (red), emission lines used to determine the plasma temperature. The assignments of these lines are listed in Tables 3.1 and 3.2. The green  $\times$  indicates an example of an emission band that produces an erroneous area value when integrated due to a high density of O I emission lines.

to each of the 7 lines listed in Table 3.1, along with the point corresponding to the erroneous peak at  $\sim 444$  nm, indicated by the green  $\times$ , thus demonstrating how outliers can be easily identified by this method. The slope of a linear fit to the points in the plot yielded a value for the LIP temperature of  $38500 \pm 5000$  K, where the error value was determined from the error in the slope of the linear fit in the Boltzmann plot.

For relatively short delay times after plasma formation there is generally a sufficient number of N II lines in the spectra for accurate temperature measurements. However, as the N II lines decay quite rapidly, for longer delay times fewer lines are available for use in the Boltzmann plot, leading to a decrease in the accuracy of the calculated temperature. This is further compounded by the emergence of atomic emission lines which also may obscure residual ionic lines. Therefore, two neutral oxygen (O I) emission lines were identified in the spectra at longer delay times, which provide a secondary measure of the LIP temperature. Details of the identified lines are listed in Table 3.2, and their expected spectral positions are indicated by the red numerals (8 and 9) in Fig. 3.6. While using only two lines to measure the temperature provides no means of detecting erroneous values, using them to calculate a value for the temperature, in combination with the N II measurement, allows for a comparison between the two values obtained to confirm consistency.

The Boltzmann plot method has been used to measure the LIP temperature from immediately after plasma formation out to a delay time of 1250 ns, the results of which are displayed in Fig. 3.8. In this figure the black dots from 0 to 450 ns indicate temperatures determined using only the N II emission lines. For longer delay times the two neutral oxygen lines in Table 3.2 were used, in addition to the remaining ionic nitrogen lines, thus allowing two values to be determined for the plasma temperature, the averages of which are represented by red dots. At the even longer delay times of 1000 ns and 1250 ns after plasma formation there are no longer any N II emission lines present in the LIP emission spectrum and at this point only O I lines can be used for the temperature measurements. These temperatures are represented by the blue dots in Fig. 3.8. As the use of only two

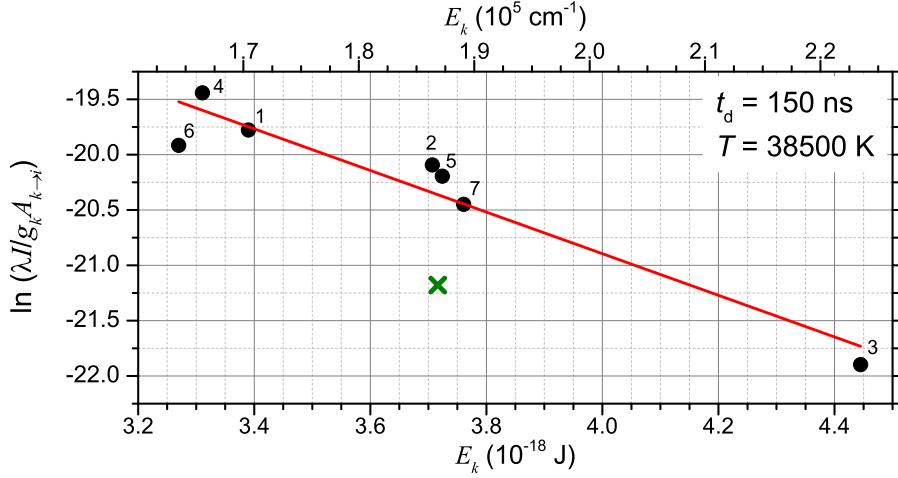


FIGURE 3.7: Example Boltzmann plot for singly ionised (NII) nitrogen lines, measured 150 ns after LIP formation. The numbers indicate the identified emission line, according to Table 3.1. The green  $\times$  is an obvious outlier corresponding to the emission peak at  $\sim 444$  nm. A linear regression fit to the points (red line) yielded a plasma temperature of  $38500 \pm 5000$  K.

values provides no measure of the error in the calculated temperature, the error bars for these two points were determined from the expected error based on the percentage error in the previous points. The first spectrum, measured immediately after plasma formation ( $t = 0$  ns with a measurement gate width of 50 ns), yielded a plasma temperature of  $\sim 63500 \pm 24000$  K, where the error in the temperature was determined from the error in the slope of the linear fit in the Boltzmann plot. The significant error in this value arises from a deviation in the integrated peak areas from the expected linear relationship in the Boltzmann plot ( $r^2 \approx 0.75$ ), with only 3 of the identified NII peaks (lines 1, 2, and 5 from Table 3.1) being usable for the Boltzmann plot, with all others causing severe deviations from the expected linear behaviour. This is likely a result of either the LIP not yet being in local thermodynamic equilibrium; a requisite condition for the Boltzmann plot method, or simply due to the broadened lines at short delay times (see Fig. 3.9) overlapping with other emission peaks, yielding inaccurate values for the line intensities. In either case, it cannot be deduced whether or not the measured temperature at  $t = 0$  ns is representative of the true value, and should therefore be treated with caution.

The green trace in Fig. 3.8 represents a mono-exponential decay fit to the measured



temperatures in the time range of 50 – 1250 ns after LIP formation. This fit returned a decay constant for the LIP temperature of  $440 \pm 45$  ns. While Aguilera and Aragón found, based on the shock wave expansion theory, that the temporal evolution of the LIP temperature is more accurately described by  $T \propto t^{-\frac{6}{5}}$  [114], for the scope of this study, an exponential fit was found to sufficiently describe the temporal behaviour of the LIP temperature, with the fit having a coefficient of determination ( $r^2$ ) of 0.986. The inset in Fig. 3.8 shows the LIP temperature measured 100 ns after plasma formation for a number of different laser pulse energies ranging from 25.5 – 100 mJ. This illustrates the weak correlation between the laser pulse energy and the temperature of the plasma. This is consistent with previous studies which found little correlation between laser irradiance and temperature [56, 65, 117], with one study determining a relationship of  $T \propto E^{0.18}$  [65] (see dark blue trace, inset Fig. 3.8).

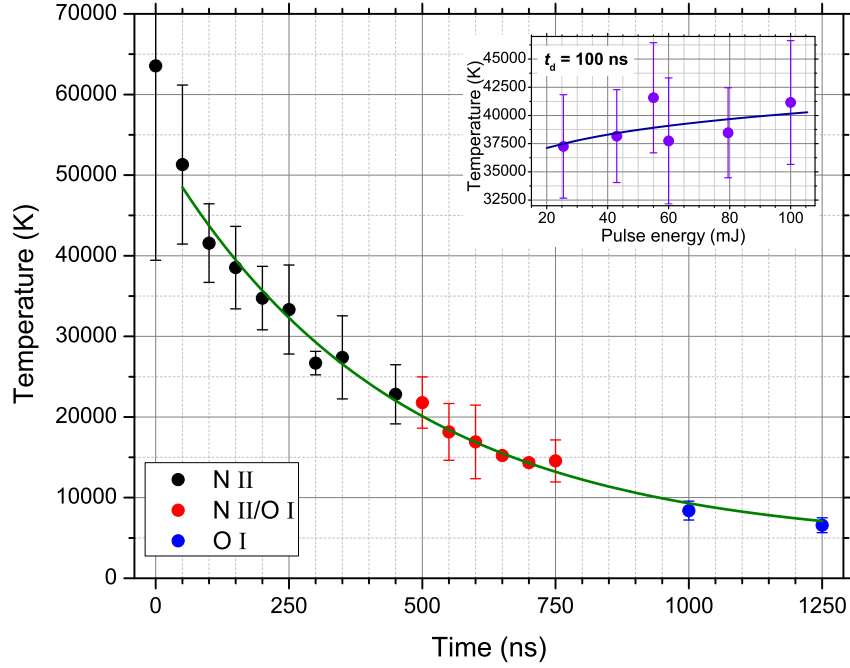


FIGURE 3.8: Measured LIP temperature up to 1250 ns after LIP formation, determined from the Boltzmann plot method. For delays up to 450 ns the temperature is determined from singly ionised nitrogen (N II) lines, for delays of 500 – 750 ns a combination of N II and neutral oxygen (O I) lines are used. Temperatures for longer delay times are determined using only O I lines. Error bars were determined from the error in the slope of the Boltzmann plot. The green trace shows an exponential fit to the temperature from 50 – 1250 ns, with a decay constant of  $440 \pm 45$  ns. Inset: Measured temperature at a delay time of 100 ns for a number of different laser pulse energies showing the weak correlation between the pulse energy and the LIP temperature. Blue trace:  $T \propto E^{0.18}$  fit to the data points shown.

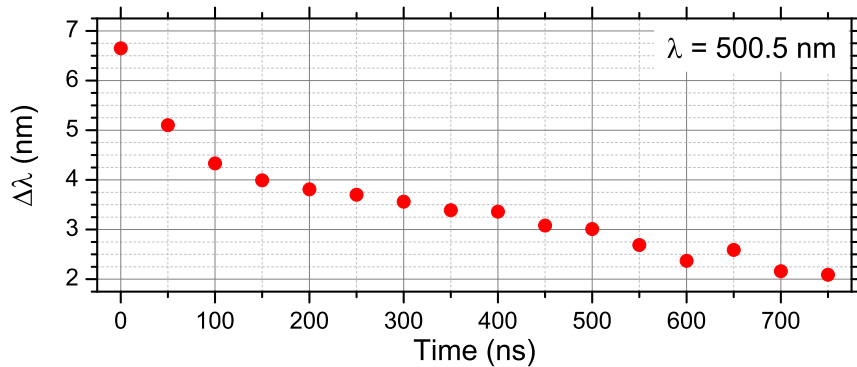


FIGURE 3.9: Temporal evolution of the linewidth (FWHM) of the N II emission line at 500.5 nm (line 2 in Fig. 3.6) after plasma formation. Significantly broadened lines at shorter delay times after plasma formation may contribute to increased errors due to overlapping emission lines.

### 3.3 Conclusion

In this chapter, the broadband continuum emission from the LIP has been characterised, with particular attention paid to how the emission spectra change with time after plasma formation. The temporal evolution of the LIP emission was found to differ between short and long delay times after plasma formation. In both cases the LIP emission decay was found to be well described by a mono-exponential function. However, at short delay times ( $t < 200$  ns) the LIP emission had a decay constant of  $\tau \approx 70$  ns, while for delay times longer than this  $\tau \approx 600$  ns. This discrepancy is attributed to the rapid expansion of the LIP that occurs at short delay times.

It has been shown that the temporal evolution of the LIP emission intensity is wavelength-dependent and can be related to the thermal evolution of the LIP. As the LIP cools, the emission maximum of the plasma continuum shifts to longer wavelengths, in accordance with Wien's law. Hence, the LIP emission is observed to decay at a slower rate at longer wavelengths. This wavelength-dependent drift in the emission intensity has some implications for the absorption baselines of measurements which utilise the LIP as a light source.

A description has also been provided of the Boltzmann plot method which is used to determine the temperature of the LIP based on the relative intensities of a number of atomic and ionic emission lines that are overlaid on the broadband LIP emission. This graphical approach was applied to the current situation, yielding a time-dependent description of the LIP temperature from 0 to 1250 ns after plasma formation. From this it was possible to model the temporal evolution of the LIP temperature from its initial value of  $63500 \pm 24000$  K as a decaying exponential with a decay constant of  $440 \pm 45$  ns.

The results from using the LIP characterised here as an intra-cavity light source for both CRDS and IBBCEAS absorption measurements will be presented in the next chapter.

# Chapter 4

## Cavity-enhanced absorption spectroscopy with intra-cavity LIPs

### LIP-formation with fs-lasers

The use of laser-induced plasmas in air as intra-cavity light sources for IBBCEAS was first demonstrated in 2015 in a proof-of-principle experiment by Ruth et al. [6]. In this study, an immediate difficulty was identified with this approach to IBBCEAS in that an LIP generated within an optical cavity constitutes an inherent time-dependent optical loss until the carrier gas, in which the plasma is generated, has returned to an equilibrium state. Therefore, the experimental parameters to generate the intra-cavity laser-induced plasma in Ref. [6] were chosen so as to minimise the physical dimensions of the LIP. Hence the LIPs were generated with relatively low laser pulse energies of  $\sim 2.6$  mJ and high peak powers of  $\sim 13$  GW, using a neodymium:glass laser which provided pulses with a FWHM duration of 200 fs. The pulses were focused into the centre of a *quasi-confocal* high-finesse optical cavity (length  $\sim 40$  cm) to maximise the light collection efficiency of the light leaking from the cavity. This approach generated short-lived and spatially small LIPs, at the expense of plasma brightness. Despite the optical

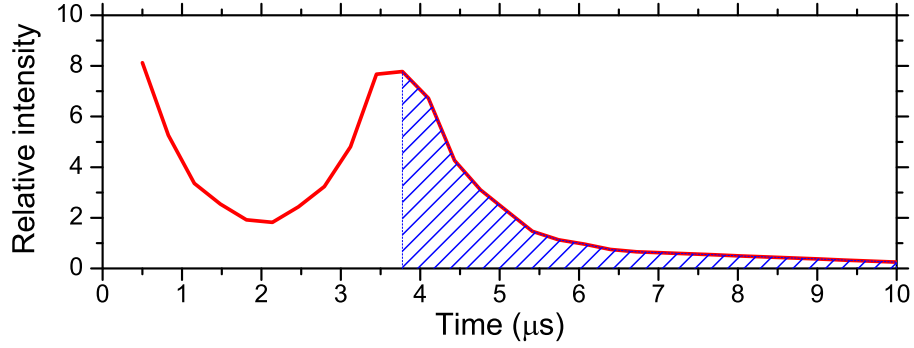


FIGURE 4.1: Illustration of the typical time-dependence of the confocal cavity output observed in Ref. [6]. The blue shading indicates the portion of the cavity output which was accumulated for IBBCEAS measurements.

losses posed by the LIP, the optical emission from the plasma was sustained within the cavity under the described conditions and used to measure IBBCEAS spectra of static gaseous azulene in ambient air (560 – 650 nm), and of molecular oxygen (625 – 635 nm). The SNR ( $\sim 30$ ) in this approach to IBBCEAS was limited by the overall low brightness of the LIP, thus necessitating relatively long integration times ( $> 10$  minutes) and substantial signal amplification.

In addition to the low brightness of the LIP, the SNR of this approach was also impacted by the, at first glance, peculiar time-dependence of the light leaking from the cavity, which limited the amount of usable light leaking from the cavity for absorption measurements. The typical time-dependence of the output from a confocal cavity, as observed in Ref. [6], is illustrated in Fig. 4.1. This time-dependence exhibited a maximum in the cavity output intensity that occurred  $\sim 3.6 \mu\text{s}$  after LIP formation. After this, the cavity output decayed mono-exponentially, in a true ringing-down of the light within the cavity. Only the mono-exponentially decaying part of the cavity output is useful for IBBCEAS measurements. Hence a large portion of the light output from the cavity is lost prior to data collection.

This unusual time-dependence is a consequence of both the absorption of light within the cavity by the plasma itself, along with the LIP producing a temporally varying non-linear refractive index change within the cavity which acts to interfere with the propagation of light within the cavity. This influence on the propagation

of light within the cavity, and its adverse effects on the intensity of the light that is leaking from the cavity, will be discussed in more detail in Chapter 5.

### **LIP-formation with ns-lasers**

The low SNR arising from the factors outlined above motivated the use of a *nanosecond* Nd:YAG laser for LIP formation in this study. The laser used provided pulses of  $\sim 10$  ns duration, with significantly higher pulse energies ( $\sim 55$  mJ), but lower peak powers ( $\sim 5.5$  MW), resulting in a larger plasma plume with greatly increased brightness. Despite the expected increase in the optical losses from the larger LIP, it was found that light is still well sustained in the cavity and the SNR of IBBCEAS measurements show a marked improvement over the previous fs-pulsed laser experiments. In addition to the ns-pulsed laser, the optical cavity dimensions were also modified to a *near-concentric* geometry ( $L = 79.3$  cm) which helps to reduce potential exposure of the mirror coatings to any highly reactive species (e.g. ions/radicals) emitted from the plasma, thus minimising degradation of the cavity mirror reflectivity over time. The loss of light due to the increase in cavity length is also partly offset by the increase in the effective path length of the cavity which yields an increase in the sensitivity of absorption measurements.

The use of a near-concentric cavity geometry also resulted in a change in the observed time-dependence of the cavity output (see Fig. 4.3) which, compared to the previous experiments, enables earlier commencement of data collection, during which time there is a greater intensity of light output from the cavity (see Section 5.4).

The data presented in this chapter represents the work featured in Ref. [118], in which an LIP from a ns-pulsed laser was generated at the centre of a near-concentric optical cavity. The light leaking from the cavity was used to measure IBBCEAS spectra of gaseous azulene in ambient air, and the spectra were compared with broadband CRDS spectra obtained with the same setup. Also included is a description of the process of using the pulsed nature of the LIP emission to

determine the effective cavity mirror reflectivity *in situ*, thus facilitating absolute absorption measurements via the IBBCEAS approach.

## 4.1 Azulene

For the absorption measurements presented below azulene was used as the absorbing species. Azulene ( $C_{10}H_8$ ), structure shown in Fig. 4.2, is an aromatic hydrocarbon and isomer of naphthalene. Due to its unusual photophysical properties [119–121], in particular its violation of Kasha’s rule [122, 123], azulene has been the subject of many spectroscopic studies [124–126]. In addition to this, due to the low oscillator strength of the  $S_1 \leftarrow S_0$  transition ( $f \approx 0.009$  [124]), azulene has also been used as a test case for a number of CEAS methods [1, 6, 127]. Azulene was also well suited to the experimental system employed in this work due to its absorption spectrum in the wavelength range covered by the HR mirrors and its ease of handling.

### 4.1.1 Preparation of the gaseous azulene samples

For the absorption measurements of azulene described here, addition of azulene to the cavity was carried out in a rather rudimentary manner, which took advantage of the reasonably high vapour pressure of azulene at room temperature of  $\sim 0.013$  mbar [128, 129]. A few crystals of azulene were placed within the cavity and allowed to sublime under ambient conditions, while the cavity chamber, consisting of metal tubing which was not completely sealed, helped to contain the azulene vapours within the cavity volume. As the equilibrium time for the azulene sublimation process is expected to be very long, the partial pressure of the azulene vapour in the cavity is markedly lower than the room temperature vapour pressure of azulene. In addition to this, the unpassivated cavity walls presented a significant sink for the azulene vapour present inside the cavity, further lowering the azulene partial pressure. Due to this loss mechanism no potential improvements

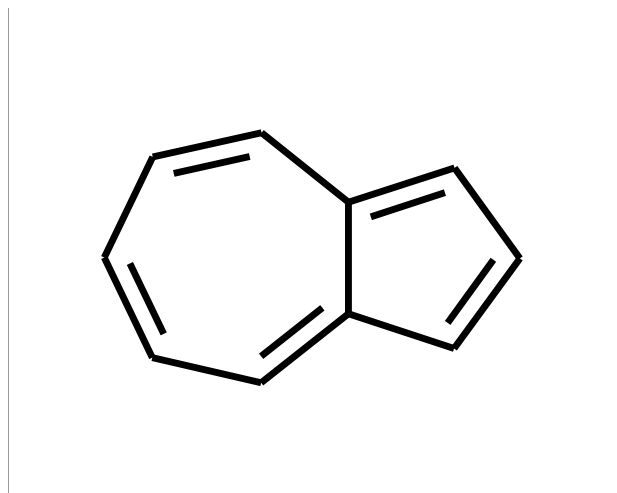


FIGURE 4.2: Chemical structure of azulene ( $C_{10}H_8$ ).

were envisaged from the potential application of heating to increase the azulene partial pressure. In principle, more control over the azulene mixing ratio could be achieved in a flow cell system, however this would yield a significant increase in the overall experimental complexity.

In a typical experiment, the cavity volume was generally flushed with dry air for some length of time (typically  $\sim 10$  mins) prior to taking CEAS measurements, in order to further lower the mixing ratio of azulene in air. Rough estimates of the azulene mixing ratio are determined in Section 4.6.1 for the purpose of estimating detection limits. However, these estimates of the azulene vapour concentration are far too inaccurate to justify any attempt at deducing meaningful values for the absorption cross-section of azulene from the measured absorption spectra shown below.



## 4.2 Cavity output and reflectivity calibration

### 4.2.1 Time-dependence of the cavity output from a near-concentric cavity

Fig. 4.3 shows the measured *near-concentric* cavity output intensity from 0 to 13  $\mu\text{s}$  after plasma formation, measured in steps of 500 ns, with an integration time of 250  $\mu\text{s}$  per step, shown at a wavelength of 631 nm. Considering that a high power ns-laser pulse was used for plasma formation, and the associated substantial physical dimension of the plasma (3–4 mm diameter), the intensity level at which light was sustained in the cavity was surprisingly high in comparison to prior experiments [6]. The time-dependence in Fig. 4.3 shows that the light is indeed sustained within the cavity by more than  $\sim 12 \mu\text{s}$ ; sufficiently long to facilitate cavity-based absorption measurements. As expected, the significant initial optical loss presented by the plasma formation within the cavity acts to decrease the output intensity immediately after LIP formation by a factor of  $\sim 7$ . This substantial intensity decrease lasts for approximately 1.5  $\mu\text{s}$ . Thereafter, the cavity output intensity begins to decay mono-exponentially (ring-down). This behaviour is in contrast to the time-dependence observed in the case of a *confocal* cavity geometry (see Ref. [6], and Fig. 4.1 and accompanying description above), where an intensity maximum was observed during the time-dependence of the light leaking from the cavity. The differences in behaviour between confocal and concentric cavity alignments is attributed to differences in how light propagates in cavities of differing geometry (see Chapter 5).

The time interval in which the light intensity leaking from the cavity decays mono-exponentially can be used to determine the effective reflectivity of the cavity mirrors. This mono-exponential decay is also used for both CRDS and IBBCEAS absorption experiments (see Sections 2.2.1 and 2.2.2). The cavity output during the initial fast decay (0 – 1.5  $\mu\text{s}$ ) is not usable for absorption measurements as the time-dependence of the cavity output at this stage is a combination of a number

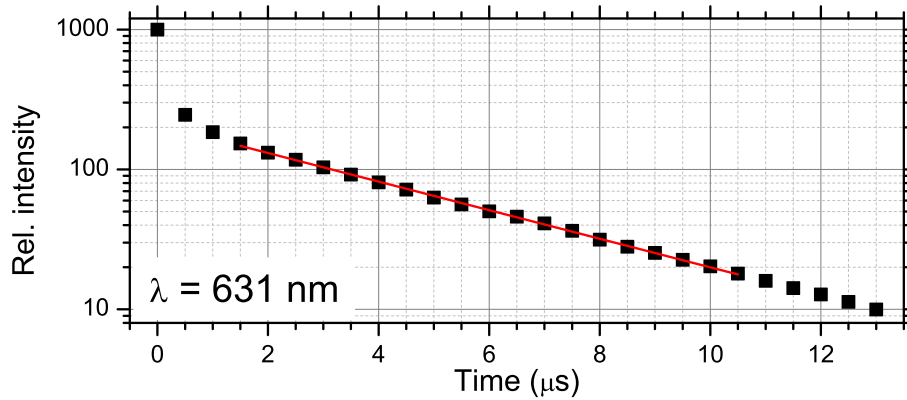


FIGURE 4.3: Semi-logarithmic plot of the measured cavity output intensity for a laser-induced plasma at the centre of a 79.3 cm cavity filled with air, measured at  $\lambda = 631$  nm. The cavity output intensity was accumulated over 500 plasma pulses with a gate duration of 500 ns, giving a total integration time of  $250 \mu\text{s}$  for each data point. After the initial factor of  $\sim 7$  decrease in intensity over the first  $1.5 \mu\text{s}$ , mono-exponential decay behaviour is observed with a corresponding ring-down time of  $4.24 \mu\text{s}$ . Red trace: Linear regression fit to the data points shown.

of processes, including the decay of light sustained in the cavity, and the decay of the LIP emission. As a result, a ring-down time for the cavity output cannot be determined based on a simple mono-exponential fit to the time-dependent cavity output. Similarly, integrating the cavity output over this time interval (see Section 4.4) yields essentially no absorption information due to the low number of round trips of light within the cavity. The cavity output at this time also experiences increased sensitivity to fluctuations in the LIP emission intensity.

#### 4.2.2 *In situ* cavity mirror reflectivity measurement

The pulsed nature of the LIP facilitates an *in situ* calibration of the effective cavity mirror reflectivity,  $R(\lambda)$ , based on the wavelength-dependent ring-down time,  $\tau_0(\lambda)$ , measured without an absorbing sample in the cavity (see Fig. 4.3).  $R(\lambda)$  is calculated as shown in Eq. 4.1, where  $c$  is the speed of light, and  $L$  represents the length (mirror separation) of the cavity:

$$R(\lambda) = 1 - \frac{L}{c\tau_0(\lambda)} \quad (4.1)$$

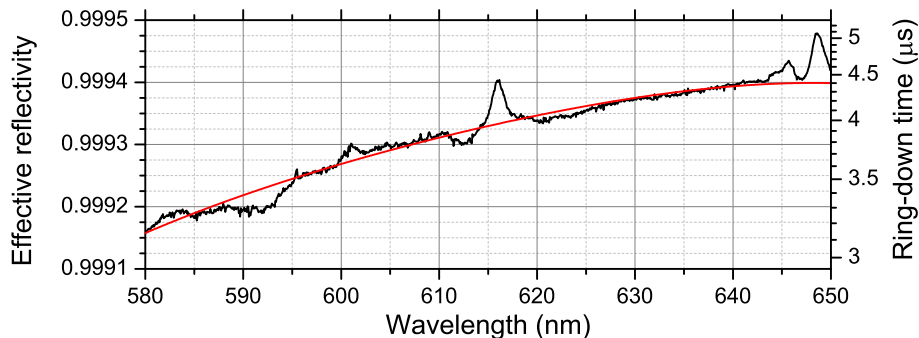


FIGURE 4.4: Black trace: Effective mirror reflectivity (left axis) calculated from the wavelength-dependent ring-down time of light leaking from the cavity (right-axis). Red trace: Fourth-order polynomial fit to the measured reflectivity spectrum.

The ring-down time was determined from the time-dependence of the light leaking from an (air-filled) cavity in the time window from 1.5 to 10.5  $\mu\text{s}$  after plasma formation, measured in steps of 0.5  $\mu\text{s}$  (see Fig. 4.3). This measurement, without azulene present in the cavity, corresponds to the  $\tau_0(\lambda)$  spectrum used for the CRDS measurements which are presented in Section 4.3. The measured wavelength-dependent reflectivity,  $R(\lambda)$ , is shown in Fig. 4.4 (left-axis) along with the corresponding ring-down time (right-axis).

It should be noted that, depending on the carrier gas used for plasma formation (air in the current case), reflectivities determined in this manner may be affected by long-lived recombination emissions from the plasma. In the case of Fig. 4.4, long-lived emission bands are visible around 616 nm and beyond 642 nm, where apparently longer lifetimes (and hence, higher reflectivities) are observed. Around the spectral regions in which long-lived recombination bands are located a mono-exponential fit function (as used in this analysis) may not necessarily provide an adequate description of the time-dependence of the cavity output intensity. This is particularly evident in Fig. 4.5 which shows the measured reflectivity along with the coefficient of determination,  $r^2$ , for the mono-exponential fit at each point in the spectrum, with clearly decreased fit quality visible around the two previously mentioned emission bands. The inadequacy of the mono-exponential description leads to a deviation from the expected smooth unstructured reflectivity spectrum. However, as the reflectivity is expectedly a smooth function of the wavelength over

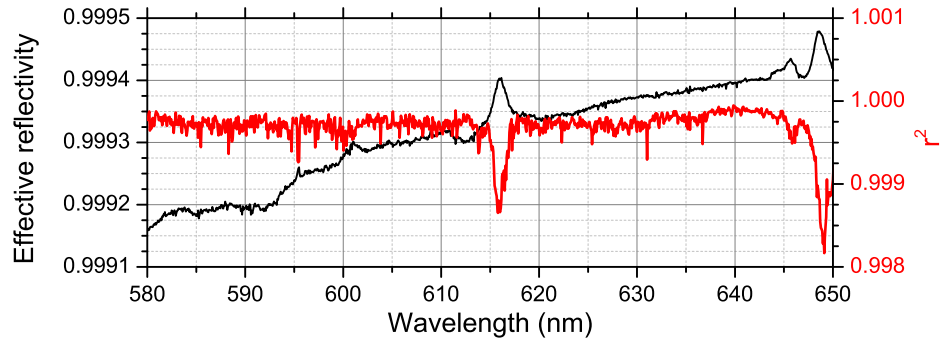


FIGURE 4.5: Measured effective mirror reflectivity (black) shown with the coefficient of determination (red) of a mono-exponential fit to the data, indicating the decrease in fit quality around the spectral regions which exhibit long-lived emission lines.

the high reflectivity range of the mirrors, emission lines can be readily eliminated by appropriately modelling the data with a polynomial fit, by using a B-spline, or Fourier filters. The red trace in Fig. 4.4 represents a fourth-order polynomial fit to the measured reflectivity. The long-lived plasma emissions should ideally be identified and studied for specific carrier gases and experimental scenarios before carrying out absorption measurements. The use of a different carrier gas which lacks significant emission lines in the spectral region of interest is another option for improving the accuracy of the measured reflectivity.

Finally, it should be noted that the maximum measured reflectivity of  $R \approx 0.9994$  at  $\sim 640$  nm is lower than the nominal on-axis reflectivity quoted by the manufacturer, while also being offset from the stated central wavelength of 610 nm. These differences arise due to this method yielding merely an effective reflectivity. High order TEM modes, which typically have shorter decay times, are populated by this approach as the entire mirror surface is used to sustain light in the cavity, and the measured reflectivity is based on an effective mean over all relevant mode lifetimes (applicable over the entire mirror surface) for the given experimental conditions (i.e. cavity geometry) [130]. The use of an intra-cavity iris which is adjusted to provide negligible losses for low order modes while acting to remove higher order transverse modes would, in principle, yield an improved ring-down time, however, this would be at the expense of a lower signal intensity due to a decrease in the

overall amount of light being sustained within the cavity. The measured reflectivity is also subject to losses due to Rayleigh scattering by air and potentially small aerosol particles ( $< 100$  nm), although the influence of this over the spectral range in question is expected to be small.

### 4.3 Broadband CRDS with LIPs as intra-cavity light sources

The following presents the results from using broadband CRDS with intra-cavity LIPs to measure the absorption spectrum of gaseous azulene.

#### 4.3.1 Broadband CRDS of gaseous azulene

Fig. 4.6 (red trace) shows the room temperature  $S_1 \leftarrow S_0$  absorption spectrum of gaseous azulene at its vapour pressure in ambient laboratory air, determined from the ring-down time of the plasma emission within the cavity, according to the CRDS analysis procedure outlined in Section 1.1. The broadband cavity output intensity was measured in steps of  $0.5 \mu\text{s}$  from  $1.5$  to  $10.5 \mu\text{s}$  after plasma formation, accumulated over 500 plasma pulses, giving a total integration time of  $250 \mu\text{s}$  per step. This stepwise approach to broadband CRDS resulted in an overall measurement time of  $\sim 16$  minutes. Mono-exponential fits to the wavelength-dependent cavity output intensities were used to determine the broadband ring-down times. The delay of  $1.5 \mu\text{s}$  was necessary to allow the cavity output to reach the mono-exponential decay stage, as described above. The measurement end time of  $10.5 \mu\text{s}$  was chosen in order to maximise the SNR of the measured spectra. Measurements extending beyond this time increased the noise level due to the lower intensity of light output from the cavity at times  $> 10.5 \mu\text{s}$ . This also led to poorer fit qualities. The measured spectrum shown in Fig. 4.6 has been corrected for the baseline absorption, as outlined in Section 4.3.2.

### The $S_1 \leftarrow S_0$ absorption band of gaseous azulene

The spectrum shown in Fig. 4.6 constitutes part of the ro-vibronic contour bands of azulene at excess energies between  $\sim 1100 \text{ cm}^{-1}$  and  $\sim 3100 \text{ cm}^{-1}$  above the 0,0 transition which is located at  $14283 \text{ cm}^{-1}$  [126]. The choice to measure this part of the  $S_1 \leftarrow S_0$  spectrum rather than the 0,0 transition at  $14283 \text{ cm}^{-1}$ , which would present a stronger absorption, was made due to the reflectivity range of the mirrors used, and the generally low sensitivity of the iCCD around the 0,0 transition. For comparison, the scaled cavity ring-down absorption spectrum of jet-cooled azulene (black trace) from a previous study is also shown [126]. Apart from the narrower band structure of the jet-cooled azulene spectrum, which is a result of the significantly lower temperature in the collisionless regime, and the higher resolution of the corresponding jet measurement, the general agreement between the two spectra is satisfactory. The steadily increasing absorption background towards shorter wavelengths in the measured CRDS spectrum in Fig. 4.6 is due to overlapping absorption features resulting from an increased density of states at higher energies in combination with the lower spectral resolution of this measurement. Discussions on this background are provided by Ruth et al. [126] and Fiedler et al. [127].

The grey shading in Fig. 4.6 represents regions in which the presence of strong emission lines are observed to interfere with the measured spectrum (compare Figs. 4.4 and 4.5). Hence, the spectrum in these regions should be treated with caution.

It should be noted that absorption measurements carried out in this manner are quite reproducible, with the spectra presented in Fig. 4.6 representing only one of the multiple azulene spectra that were recorded. The main obstacle to repeated measurements was drift in the overall cavity alignment over time which would affect the cavity ring-down time, thus lowering the performance of this approach in terms of the achievable SNR. While the reproducibility of CEAS measurements via this approach is dependent on the cavity alignment, preliminary tests indicate that the exact position of the LIP within the cavity is not critical. It was found that small deviations in the LIP position *off* the optical axis ( $\sim \pm 2 \text{ mm}$ ) have only

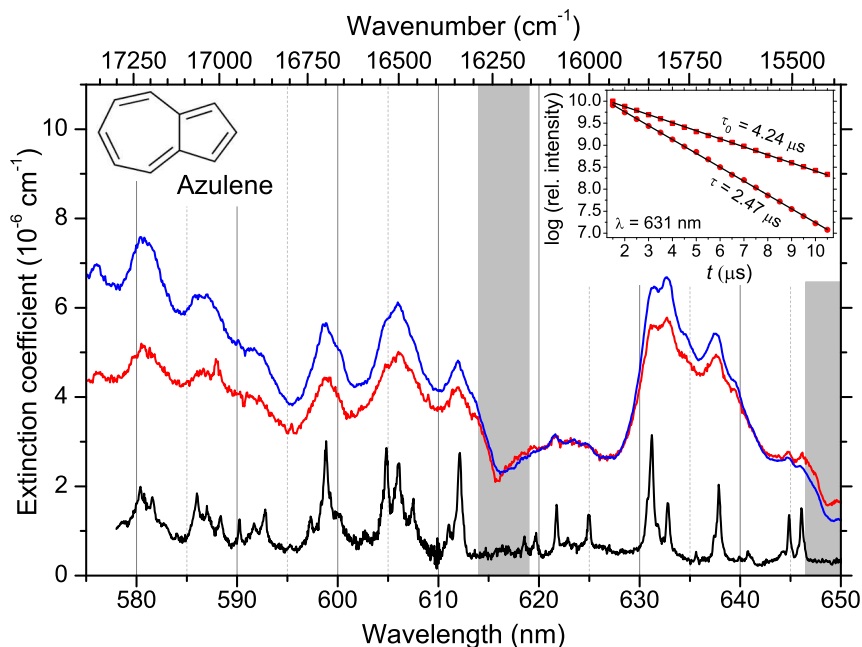


FIGURE 4.6: Red trace: Broadband CRDS spectrum of azulene obtained from the ring-down time of light leaking from the cavity between 1.5 and 10.5  $\mu\text{s}$  after plasma formation. The ring-down time was measured in steps of 0.5  $\mu\text{s}$  accumulated over 500 plasma pulses (integration time of 250  $\mu\text{s}$ ) per step. Blue trace: IBBCEAS spectrum of azulene (see Section 4.4.1) obtained by accumulating the cavity output for 500 plasma pulses from 1.5 to 10.5  $\mu\text{s}$  after plasma formation; total integration time of 4.5 ms. Determination of the extinction coefficient is based on the effective reflectivity shown in Fig. 4.4. Black trace: Arbitrarily scaled cavity ring-down absorption spectrum of jet-cooled azulene from [126] for comparison. Inset: Semi-logarithmic plot of the cavity output intensity showing the ring-down time measurements including the respective fit without and with azulene present in the cavity (red squares and dots respectively), measured at 631 nm (also compare Fig. 4.3).

a slight influence on the measured cavity ring-down times (likely a consequence of excited off-axis cavity modes), with greater deviations in the LIP position causing a significant drop in the cavity output signal. Conversely, the achievable ring-down times were found to be largely unaffected by deviations in the LIP position of up to 1 cm *along* the optical axis.

### 4.3.2 CRDS baseline and SNR

The absorption baseline for CRDS measurements was determined from two separate measurements of the broadband cavity ring-down times ( $\tau_{0a}(\lambda)$  and  $\tau_{0b}(\lambda)$ )

without azulene present in the cavity.

$$\varepsilon_{\text{base}}(\lambda) = \frac{1}{c} \left( \frac{1}{\tau_{0a}(\lambda)} - \frac{1}{\tau_{0b}(\lambda)} \right) \quad (4.2)$$

This baseline measurement accounted for drifts in the cavity ring-down time over the course of the absorption measurement. The measured baseline is shown in Fig. 4.7, along with the two ring-down spectra,  $\tau_{0a}$  and  $\tau_{0b}$ , which were used to determine it. A cubic spline (interpolated between 10 points) was applied to the measured baseline to reduce the noise, shown as the red trace in Fig. 4.7. The measured baseline is, in first approximation, constant ( $\sim 0.15 \times 10^{-6} \text{ cm}^{-1}$ ) over the relevant spectral region; a consequence of the general insensitivity of CRDS to changes in the light source emission spectrum. However, the baseline is quite noisy, exhibiting a standard deviation of approximately 30% of the baseline intensity. This noise mainly arises due to the fitting procedure.

Knowing the absorption baseline, the signal-to-noise ratio (SNR) of the measured CRDS spectrum can be determined to be 51. Here the noise level was taken to be twice the standard deviation of the baseline noise around the spline baseline shown in Fig. 4.7. For this calculation of the noise level the regions from 611 – 619 nm, and  $\lambda > 646.5$  nm (see grey shading in Fig. 4.7) were excluded. The calculated SNR corresponds to a minimum detectable absorption coefficient,  $\varepsilon_{\text{min}}$ , of  $7.4 \times 10^{-8} \text{ cm}^{-1}$ . Accounting for the measurement time yields a noise equivalent absorption of  $2.3 \times 10^{-6} \text{ cm}^{-1} \text{ Hz}^{-\text{frac}12}$ . This value for the minimum detectable absorption, combined with an estimate for the azulene vapour mixing ratio, facilitates a rough approximation of the detection limit for azulene, which will be outlined in Section 4.6.1.

It is expected that the energetic LIP process will lead to breakdown of the azulene molecules within the plasma volume thus producing secondary compounds, including long-chain carbon molecules. Absorption by these secondary compounds may serve as a source of noise in measured absorption spectra. However, the scale of this is not expected to be significant enough to be of much concern. Even



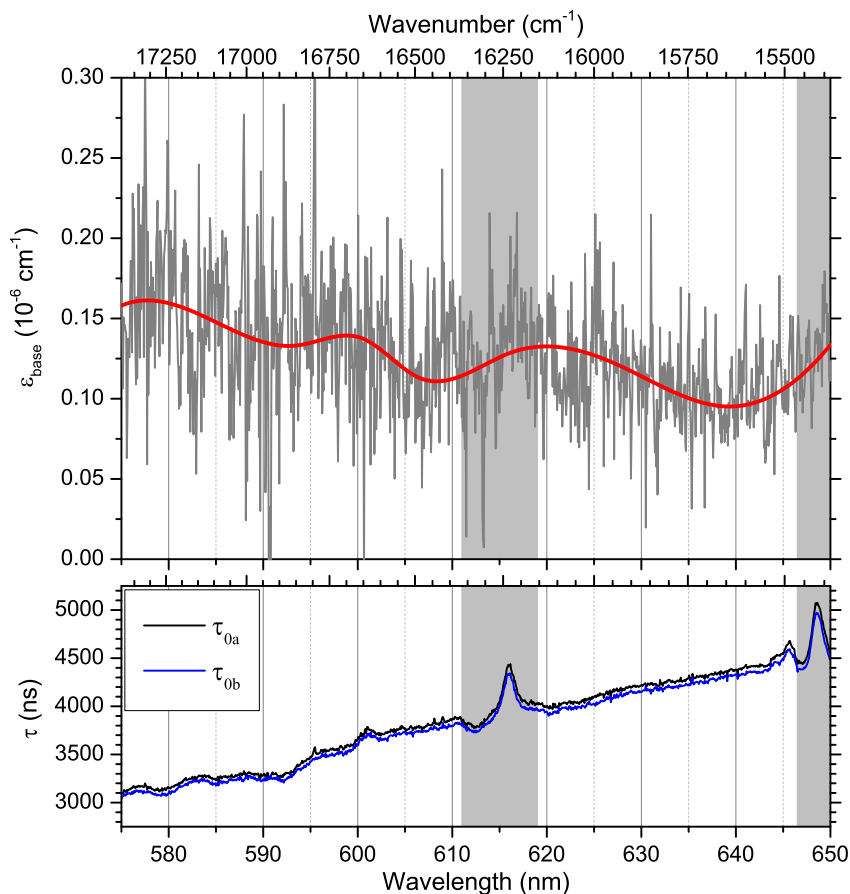


FIGURE 4.7: CRDS absorption baseline (grey) determined from two separate ring-down measurements without azulene present within the cavity (see lower panel). Red trace: Cubic spline applied to the measured baseline. The grey shading indicates regions of the baseline that were excluded from SNR calculations due to the previously identified emission lines.

taking the maximally possible mixing ratio of azulene of 250 ppbv (as described in Section 4.6.1), the small LIP volume of  $\sim 0.01 \text{ cm}^3$  means that only a relatively small number of azulene particles ( $\sim 6.26 \times 10^{10}$ ) will be within the plasma volume at any given time. This, combined with the comparatively large cavity volume of  $\sim 996.5 \text{ cm}^3$ , means that even if all of the azulene molecules present in the plasma volume were converted into some other long-chain carbon molecule, the expected mixing ratio of this species would still be maximally 2.5 parts per trillion (pptv). Assuming a similar absorption cross-section to azulene, this corresponds to an absorption that is many orders of magnitude below the minimum detectable absorption of the setup. In principle, these plasma by-products may begin to accumulate after a large number of plasma pulses, however, it is still not

expected to be an appreciable source of error or contribution to the noise.

## 4.4 IBBCEAS with LIPs as intra-cavity light sources

The following presents the results from using the IBBCEAS approach to measure the absorption spectrum of gaseous azulene.

### 4.4.1 IBBCEAS of gaseous azulene

The IBBCEAS spectrum (blue trace) shown in Fig. 4.6 was obtained by integrating the cavity output and accumulating over 500 plasma pulses from 1.5 to 10.5  $\mu\text{s}$  after plasma formation, giving a total integration time of 4.5 ms. With a laser repetition rate of 9.7 Hz, this results in a total measurement time of  $\sim 52$  s, approximately 18 times shorter than that of the corresponding CRDS spectrum shown in Fig. 4.6. The baseline absorption spectrum was also subtracted from the IBBCEAS spectrum, as described in Section 4.4.2.

Absolute extinction coefficient values for the IBBCEAS measurement were determined using the effective reflectivity curve previously determined in Section 4.2. However, due to the aforementioned uncertainty in the absolute azulene vapour mixing ratio (which is caused by the rather basic means of introducing gaseous azulene into the cavity) deduction of meaningful absorption cross-sections from this measurement has not been attempted.

As previously mentioned in Section 4.3, the steadily increasing absorption to shorter wavelengths is a consequence of overlapping absorption features due to an increasing density of states at higher energies in combination with the lower resolution of the measurement.

From Fig. 4.6 it can be seen that the absorption spectrum measured via IBBCEAS shows generally good qualitative agreement with that measured through the broadband CRDS approach. However, extinction coefficients measured via IBBCEAS appear to be systematically larger than those measured with the broadband CRDS technique. This discrepancy between the spectra is a generic consequence of the IBBCEAS measurement being pulsed (rather than CW), in combination with the fact that there is a time-delay prior to data collection. Absorption measurements carried out via these approaches require some delay time prior to data collection ( $1.5 \mu\text{s}$  in the case of Fig. 4.6) to fulfill Lambert-Beer pre-conditions (mono-exponential decay). A full description of the source of this offset, and how it is corrected for, is provided in Section 4.5.

#### 4.4.2 IBBCEAS baseline and SNR

As in Section 4.3, the IBBCEAS absorption baseline, shown in Fig. 4.8, was determined from two separate accumulations of the cavity output spectrum,  $I_{0a}(\lambda)$  and  $I_{0b}(\lambda)$ , (shown in Fig. 4.8) without the absorbing species (azulene) present within the cavity.

$$\varepsilon_{\text{base}}(\lambda) = \frac{1 - R(\lambda)}{L} \left( \frac{I_{0a}(\lambda)}{I_{0b}(\lambda)} - 1 \right) \quad (4.3)$$

Again, a cubic spline (interpolated between 10 points) was applied to the measured baseline, yielding the smooth baseline shown as the red trace in Fig. 4.8. The baseline is both larger in magnitude than that determined for CRDS measurements and it shows a clear upward trend to shorter wavelengths, which are direct consequences of the sensitivity of IBBCEAS to any change in the LIP emission intensity between measurements. As outlined in Section 3.1.2, if the LIP emission is treated as a blackbody emission which follows Planck's law, then any drift in the plasma temperature will yield a wavelength-dependent change in the corresponding emission spectrum, with a more significant drift to shorter wavelengths. This effect is clearly evident in Fig. 4.8 in which a decrease in the overall LIP

emission intensity between the two measurements (black and blue traces in the lower panel) contributes to a greater absorption baseline at shorter wavelengths. This is in contrast to that observed in the case of the CRDS baseline shown in Fig. 4.7, which, due to the general insensitivity of ring-down methods to fluctuations in the light source emission intensity, exhibits no particularly strong spectral dependence, instead having a roughly constant value across the spectral range.

In comparison to the CRDS baseline above, the level of noise here is significantly smaller at approximately 3% of the baseline, which arises from the much longer integration time and the lack of any fitting procedure which may impart more noise on to the measured spectrum. As before, the SNR for the IBBCEAS measurements was determined from the standard deviation of the noise level, i.e.  $2\sigma = \varepsilon_{\min} = 4.7 \times 10^{-8} \text{ cm}^{-1}$ , corresponding to a noise equivalent absorption of  $3.4 \times 10^{-7} \text{ cm}^{-1} \text{ Hz}^{-\text{frac}12}$ . Combined with the spectrum in Fig. 4.6, this yields an SNR of 104, approximately two times larger than the SNR of the CRDS measurement. The value for the SNR can be compared to the previous work carried out with a confocal cavity and fs-pulsed laser [6] which yielded an SNR of approximately 30 for a greatly increased integration time of 180 ms, thus illustrating the significantly improved performance of the current approach using a ns-pulsed laser.

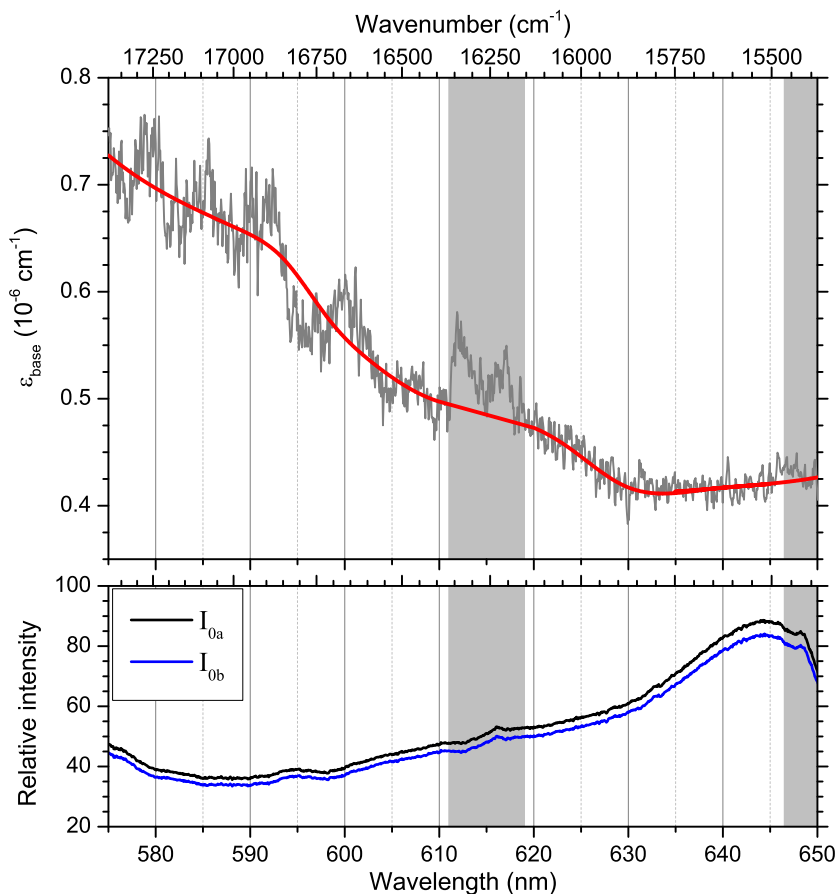


FIGURE 4.8: IBBCEAS absorption baseline (grey trace) determined from two separate accumulations (lower panel) of the cavity output without azulene present in the cavity. Red trace: Cubic spline applied to the measured baseline. The grey shading indicates regions that were not included in calculations of the SNR.

## 4.5 Correction to measured IBBCEAS spectra

The following provides an explanation of the origin of the offset that is observed in IBBCEAS measurements due to the necessary delay between LIP formation and the commencement of data collection. This is followed by a description of two numerical approaches to correcting the measured IBBCEAS spectra to account for this offset.

### 4.5.1 Origin of the offset in IBBCEAS measurements

The origin of the offset is demonstrated in Fig. 4.9, in which the measured IBBCEAS spectrum of gaseous azulene is shown for three different measurement delay times – 1.5, 3.0, and 4.5  $\mu\text{s}$  after LIP formation. The measured absorption shows a substantial increase with increasing delay time. The three spectra shown here were determined from a summation of a number of sequential measurements of gate width 0.5  $\mu\text{s}$ , from the stated delay time to 10.5  $\mu\text{s}$  after plasma formation. As such, these spectra are all comprised of the same data, and hence, measure the same azulene mixing ratio. Therefore, the increasing offset is a direct result of the increasing delay time, and not a coincidental change in azulene mixing ratio between measurements. Similarly, the relatively larger noise level in these spectra compared to the direct IBBCEAS spectrum in Fig. 4.6 is a consequence of these spectra being comprised of a summation of a number of separate shorter measurements of 0.5  $\mu\text{s}$ , each with an integration time of only 250  $\mu\text{s}$ , compared to 4.5 ms for the direct IBBCEAS spectrum.

In IBBCEAS, the fractional absorption  $I_0/I - 1$  is determined, which is based on the measurement of the time-integrated intensities without the sample,  $I_0$ , and with the sample,  $I$ , in the cavity. The measurement condition for determining  $I$  and  $I_0$  must (ideally) be identical for the measurement principle to hold [2, 30]. Introducing a delay in a pulsed IBBCEAS measurement scheme impinges on this condition, since absorption already takes place during the delay before the start time of the data acquisition, when a sample is present in the cavity (a schematic of the situation is shown in Fig. 4.10). Thus the intensities,  $A_{I_0}$  and  $A_I$ , at the time when signal integration starts, are not identical; in fact  $A_{I_0} > A_I$ . The *measured absorption* is therefore larger than the *true absorption* by an amount that corresponds to the absorption of light in the cavity during the delay time (between  $t = 0$  and  $t_{\text{start}}$ ). As a consequence, pulsed IBBCEAS spectra measured with a delay tend to give larger absorptions than CRD spectra, which, due to the intensity-independent measurement approach of the latter, are not affected by the delay. It should be noted that this source of error is not unique to this experimental

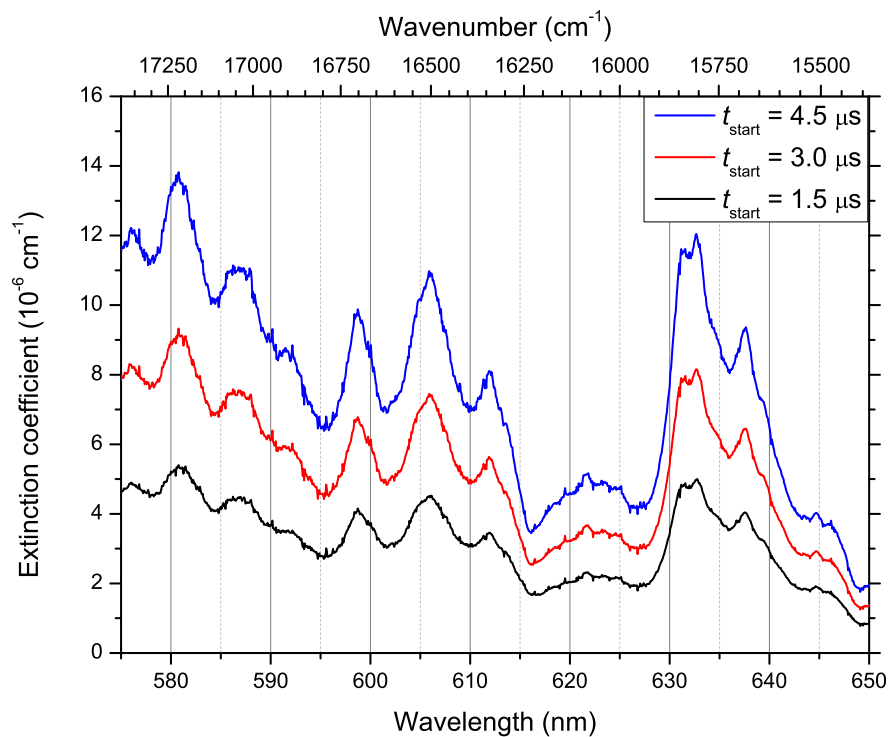


FIGURE 4.9: Measured IBBCEAS spectra of azulene for measurement delay times,  $t_{\text{start}}$ , of 1.5 (black), 3.0 (red), and 4.5 (blue)  $\mu\text{s}$ , with a measurement end-time,  $t_{\text{end}}$ , of 10.5  $\mu\text{s}$  for each measurement. The increase in measured absorption with increasing delay time is due to the absorption of light that occurs prior to data collection.

approach using laser-induced plasmas, but applies to all *pulsed* IBBCEAS systems where a delay after light generation is necessary for whatever experimental reason. The shorter the delay, the smaller the discrepancy between the measured and the true absorption spectrum.

It should be noted that despite this offset it is advantageous to determine a spectrum from the IBBCEAS approach, because measurement times are shorter due to using only one long gate window, and because higher signal to noise ratios can be achieved in comparison of the CRDS approach, where the scanning of the delay of the gate window is significantly more cumbersome.

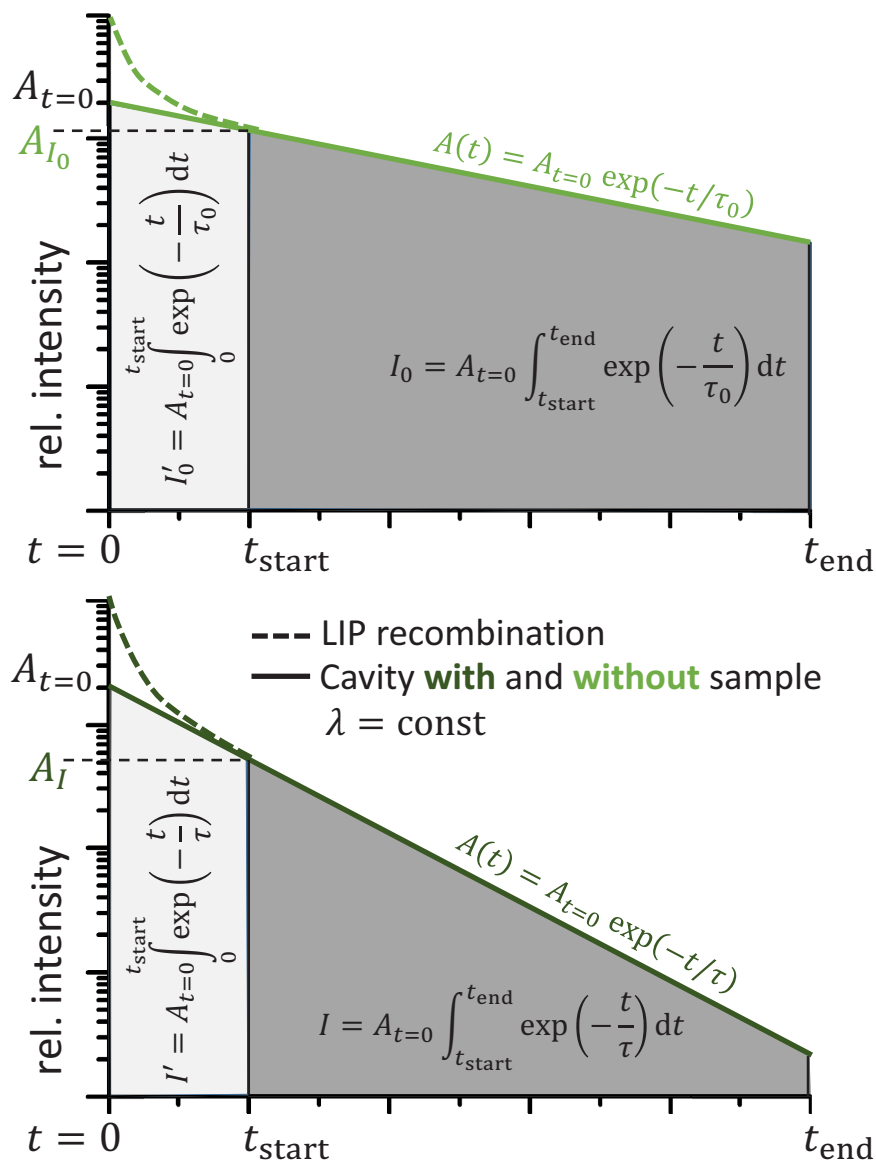


FIGURE 4.10: Illustration of the source of error in pulsed IBBCEAS measurement with delayed (i.e. gated) data acquisition.  $A(t)$  is the time-dependent cavity output intensity without (light green) and with (dark green) the sample.  $I$  and  $I_0$  (both dark grey) are the time-integrated intensities as measured in pulsed IBBCEAS during the gate time, i.e.  $(t_{\text{end}} - t_{\text{start}})$ .  $I'$  and  $I_0'$  (both light grey) are the time-integrated intensities during an arbitrary delay time,  $t_{\text{start}}$ , that needs to be accounted for. If not corrected, pulsed gated IBBCEAS will deliver absorption coefficients that are too high, depending on the gate delay.



## 4.5.2 Procedure for correcting IBBCEAS spectra

Accounting for the absorption offset analytically is not possible. Thus corrections are applied to the gated IBBCEAS spectra using two similar numerical procedures, which are outlined and compared here. The approach is illustrated in Figure 4.10, where typical schematic decays after pulsed excitation are shown for the cases without and with the sample (upper and lower panel, respectively). The assumptions (AS $i$ ) are made that, at each wavelength in the relevant spectral range, the following quantities are known in a typical IBBCEAS measurement:

- (AS1) The value of the *time integrated signal* without and with a sample in the cavity (dark grey areas in Fig. 4.10, denoted  $I$  and  $I_0$ ).
- (AS2) The *ring-down times of the cavity without the sample*,  $\tau_0$ , from which the mirror reflectivity,  $R(\lambda)$ , is deduced (as per Section 4.2). From the latter measurement also the light signal amplitude  $A(\lambda, t = 0)$  (denoted  $A_{t=0}$ ) is known.

By accounting for the integration gate width in the  $R(\lambda)$  calibration (500 ns in the case of Fig. 4.3),  $A_{t=0}$  can be determined from the constant term in the linear regression fit to the linearised mono-exponential decay (see Eq. 2.2). This constant, which corresponds to the  $y$ -intercept of the fit (i.e. the expected logarithmic integrated intensity from  $t = 0 - 500$  ns), is denoted  $\ln[C_0]$ . Therefore,  $A_{t=0}$  may be calculated as shown in Eqs. 4.4 and 4.5:

$$C_0 = A_{t=0} \int_0^{500} \exp\left[-\frac{t}{\tau_0}\right] dt \quad (4.4)$$

$$A_{t=0} = \frac{C_0}{\tau_0} \left(1 - \exp\left[-\frac{500}{\tau_0}\right]\right)^{-1} \quad (4.5)$$

Using this value for  $A_{t=0}$ , a value for the total light intensity that would be output from the cavity for  $0 < t < t_{\text{start}}$  without an absorbing species present,  $I_0'$ , can be calculated as follows:

$$I_0' = A_{t=0} \int_0^{t_{\text{start}}} \exp\left[-\frac{t}{\tau_0}\right] dt \quad (4.6)$$

In the case of an absorbing sample present within the cavity, the integrated cavity output is given by:

$$I = A_{t=0} \int_{t_{\text{start}}}^{t_{\text{end}}} \exp\left[-\frac{t}{\tau}\right] dt = A_{t=0} \tau \left( \exp\left[-\frac{t_{\text{start}}}{\tau}\right] - \exp\left[-\frac{t_{\text{end}}}{\tau}\right] \right) \quad (4.7)$$

Since  $I$  and  $A(\lambda, t = 0)$  are known from measurements as assumed in (AS1) and (AS2) the only unknown in Eq. 4.7 is the ring-down time  $\tau$ . Through a numerical solution of the transcendental Eq. 4.7 the value of  $\tau$  can be evaluated for each wavelength.

By obtaining  $\tau(\lambda)$  the spectrum of the absorption coefficient  $\varepsilon$  can be evaluated if, in addition to (AS2), another assumption is made:

**(AS3)** The light signal amplitude  $A(\lambda, t = 0)$  (known from (AS2)) does not strongly change between measurements with and without the sample in the cavity (cf. intercept in Fig. 4.10); in other words the excitation light source (averaged over appropriate data acquisition cycles) must be stable enough not to introduce an additional systematic uncertainty in the correction.

This is a generic precondition for IBBCEAS. If assumption (AS3) is not fulfilled, an additional systematic error arises in the form of a small additional (positive or negative) offset in the correction. There are two ways to obtain the corrected absorption coefficient from  $\tau(\lambda)$ , which can be jointly used as a criterion to assess

(AS3), and evaluate the light source instability (drifts or fluctuations) by simple comparison of the results:

- (1) *CRDS based evaluation:* As  $\tau_0$  is known from (AS2) the corrected absorption coefficient at each wavelength can be simply evaluated from

$$\varepsilon_{(1)}(\lambda) = \frac{1}{c} \left( \frac{1}{\tau(\lambda)} - \frac{1}{\tau_0(\lambda)} \right) \quad (4.8)$$

- (2) *CEAS based evaluation:* From the numerically determined  $\tau$  and  $A_{t=0}$  (from (AS3)) a ring-down transient can be modelled and integrated up to the delay time,  $t_{\text{start}}$ , as in Eq. 4.6, thus yielding the unknown contribution to the absorption signal,  $I'$ . From  $I_0'$  (known from (AS2)) and  $I'$ , the new corrected IBBCEAS spectra can be determined:

$$\varepsilon_{(2)}(\lambda) = \frac{1 - R(\lambda)}{L} \left( \frac{I_0(\lambda) + I_0'(\lambda)}{I(\lambda) + I'(\lambda)} - 1 \right) \quad (4.9)$$

The IBBCEAS data (blue trace) in Fig. 4.6 were corrected using Eq. 4.8 and Eq. 4.9, and are shown in comparison with the CRDS spectrum (red) in Fig. 4.11. Based on the complete equilibration time of the plasma in the corresponding experiment (including expansion and full ion recombination),  $t_{\text{start}}=1.5 \mu\text{s}$  was used for this calculation. Furthermore  $t_{\text{end}} = 10.5 \mu\text{s}$  based on the IBBCEAS acquisition gate window of  $9 \mu\text{s}$ , and  $A_{t=0}$  determined from the data shown in Fig. 4.4 were used.

In this case, Eq. 4.7 was solved via a graphical approach in which the point of intersection of  $I/\tau A_{t=0}$  and  $(\exp[-\frac{t_{\text{start}}}{\tau}] - \exp[-\frac{t_{\text{end}}}{\tau}])$ , for varying  $\tau$ , was found numerically.

Both correction methods, (1) and (2) (light-blue and dark-blue traces in Fig. 4.11 respectively), produce very similar spectra with lower absorption coefficients than

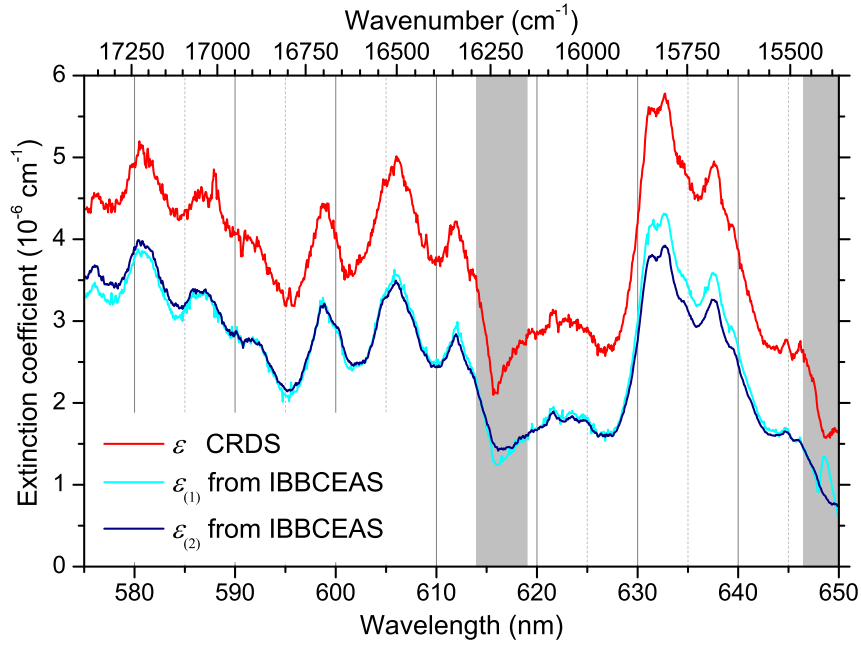


FIGURE 4.11: Red trace: Broadband CRDS spectrum of gaseous static azulene in ambient air from Fig. 4.6. Blue traces: IBBCEAS spectra from Fig. 4.6 corrected using CRDS-based evaluation (1)-light blue ( $\varepsilon_{(1)}$ ), and CEAS-based evaluation (2)-dark blue ( $\varepsilon_{(2)}$ ).

the uncorrected IBBCEAS spectrum in Fig. 4.6, and in accordance with expectation:  $\varepsilon_{(1)} \approx \varepsilon_{(2)} < \varepsilon$ . The good agreement between  $\varepsilon_{(1)}$  and  $\varepsilon_{(2)}$  indicates that the light source did not show severe light intensity variations between the CRDS measurement without a sample (Fig. 4.4) and the gated IBBCEAS measurement. The corrected IBBCEAS spectra in Fig. 4.11 is approximately 30% lower than the CRD spectrum (see Fig. 4.6). This approximately constant difference between the spectra is attributed to a smaller azulene mixing ratio in the cavity during the IBBCEAS measurement in comparison to the CRDS measurement, due to a time delay of more than 16 minutes between measurements. It should be noted that the spectrum  $\varepsilon_{(2)}(\lambda)$  exhibits somewhat more noise than  $\varepsilon_{(1)}(\lambda)$ . This is a consequence of the level of noise in the  $\tau_0(\lambda)$  spectrum which leads to increased noise in the calculated  $\varepsilon_{(2)}(\lambda)$ . This is in contrast to  $\varepsilon_{(1)}(\lambda)$  which is determined mostly from the lower noise integrated cavity output.

In summary, for gated pulsed IBBCEAS the delay time of the measurement window should be as short as possible to avoid overestimation of the measured absorption. If a CRDS spectrum of the empty cavity is known, the systematic overestimate of the absorption in pulsed IBBCEAS, arising from the gating, can be corrected through a numerical approach. In contrast to gated pulsed IBBCEAS, the intensity-*independent* nature of CRDS does not exhibit this bias, however, with the current approach the CRDS measurement time are significantly longer than those for IBBCEAS. Even though broadband pulse CRDS can be assumed to deliver unbiased absorption data, IBBCEAS (and subsequent correction) eliminates the need for more time-consuming ring-down measurements for each sample.

## 4.6 Comparison between CRDS and IBBCEAS approaches

When comparing the two approaches to CEAS with intra-cavity LIPs, it can be seen that while absorption measurements via the CRDS approach have the advantage of measuring absolute extinction coefficients which are generally unaffected by drifts in the LIP emission intensity and the delay between LIP formation and data collection, IBBCEAS measurements present a number of advantages in terms of performance. When compared to CRDS (SNR = 51), the IBBCEAS measurements show an improved SNR of 104, and a corresponding lower minimum detectable absorption of  $4.7 \times 10^{-8} \text{ cm}^{-1}$ , compared to that for CRDS of  $7.4 \times 10^{-8} \text{ cm}^{-1}$ . These improved figures of merit also come with a significant decrease in measurement time from  $\sim 16$  minutes for the CRDS measurement to  $\sim 52$  seconds for the IBBCEAS. These correspond to noise equivalent absorptions of  $2.3 \times 10^{-6} \text{ cm}^{-1} \text{ Hz}^{-\frac{1}{2}}$  and  $3.4 \times 10^{-7} \text{ cm}^{-1} \text{ Hz}^{-\frac{1}{2}}$  for the CRDS and IBBCEAS approaches, respectively. It would, in principle, be possible to shorten the CRDS measurement time by reducing the number of time steps over which data is collected (the spectrum shown in Fig. 4.6 was determined from 18 steps of  $0.5 \mu\text{s}$ ), however this reduction in data points would lead to a reduced fit quality when

	CRDS	IBBCEAS
Measurement time (s)	928	52
SNR	51	104
Min. detectable $\varepsilon$ ( $10^{-8}$ cm $^{-1}$ )	7.4	4.7
Noise equivalent $\varepsilon$ ( $10^{-6}$ cm $^{-1}$ Hz $^{-\frac{1}{2}}$ )	2.3	0.34

TABLE 4.1: Comparison of the figures of merit for both the CRDS and IB-BCEAS approaches to CEAS with intra-cavity LIPs.

determining the ring-down times, which would yield an increase in the noise in the spectrum, thus lowering the SNR, and increasing the minimum detectable absorption.

Table 4.1 lists figures of merit for both the CRDS and the IBBCEAS approach to cavity-enhanced absorption measurements using an LIP as an intra-cavity light source. Based solely on these values, IBBCEAS would be the preferred choice, possessing a greater SNR and lower minimum detectable absorption, along with a significantly shorter overall measurement time. However, these performance benefits of IBBCEAS are offset by the need to determine the mirror reflectivity curve in order to carry out absolute absorption measurements, and, more significantly, the absorption offset present in IBBCEAS measurements of this nature which must be accounted for (see Section 4.5).

Consequently, the choice of approach must be tailored to the specific experimental requirements, with the IBBCEAS approach being suited to experiments that require reasonably rapid absorption measurements without too much emphasis on absolute absorption signals. In this case, the effective cavity mirror reflectivity would be determined from an initial (slow) measurement of the broadband ring-down time of the cavity in the absence of the absorbing species, with this reflectivity curve then used for all subsequent measurements carried out using the (fast) IBBCEAS approach.

In contrast, the CRDS approach directly provides absolute absorption measurements without the need for an independent calibration of the mirror reflectivity. As the LIP exhibits considerable shot-to-shot fluctuations in the emission intensity, the intensity-independent aspect of CRDS also presents an advantage. However,

the very long measurement times required for the CRDS approach hamper its application to absorption measurements.

#### **4.6.1 Estimation of azulene mixing ratio and detection limits**

As a final point of comparison between the two approaches, the following provides rather rough estimates of the detection limit for azulene, based on the measured azulene spectra above. The detection limits are calculated in two different ways: (a) by using an estimation of the azulene mixing ratio based on the equilibrium conditions of air and azulene, and (b) by using literature values for the wavelength-dependent absorption cross-section of azulene.

##### **Estimation of azulene vapour mixing ratio**

Based on the azulene room temperature vapour pressure in ambient air of  $\sim 0.013$  mbar, if the system was allowed sufficient time to come to equilibrium, the azulene mixing ratio in the cavity would be  $\sim 12.8$  ppmv. However, the expected mixing ratio within the cavity is significantly lower due to the slow azulene sublimation process not coming to equilibrium, and the flushing of the cavity with dry air prior to absorption measurements. Other unspecified losses, such as wall losses, also contribute to a lower vapour mixing ratio. For the corrected IBCEAS measurement shown in Fig. 4.11, the cavity was flushed with dry air at a flow rate of  $\sim 1$  litre per minute (LPM) for 10 minutes prior to data collection. A cavity length of  $\sim 79.3$  cm, with a mirror radius of 2 cm, corresponds to a cavity volume of  $\sim 996.5$  cm<sup>3</sup>. If total mixing of the dry air within the cavity is assumed, then the contents of the cavity will be diluted by a factor of 2 approximately every minute. Therefore, after 10 minutes of flushing, the mixing ratio of azulene within the cavity will have decreased by approximately 3 orders of magnitude to  $\sim 12.5$  ppbv. In practice, the mixing of the flushing air in the cavity is expected to be far less efficient. Any residual azulene crystals in the cavity will continue to sublime, thus replenishing the azulene vapour within the cavity, and other loss

mechanisms (e.g. wall losses) will decrease the azulene mixing ratio. As a result of these factors, the measured azulene mixing ratio has a high degree of uncertainty, but is expected to be greater than 12.5 ppbv.

Based on the equilibration time, the partial pressure of azulene in the cavity, prior to flushing of the cavity, is assumed to be maximally 75% of the vapour pressure, i.e. 9.6 ppmv. Similarly, the mixing efficiency of the flushing gas with the cavity contents are also assumed to be  $\sim 50\%$ . Based on these values, the measured mixing ratio of gaseous azulene within the cavity during the absorption measurements is estimated to be within the rather large range of 12.5 – 300 ppbv, with the actual value likely being at the higher end of the range. From this potential range, and the SNR values determined previously, values for the detection limit of the system were determined to be in the range of 0.12 – 2.9 ppbv for IBBCEAS, and 0.25 – 5.9 ppbv for CRDS measurements.

### **Literature values for azulene absorption cross-section**

While the total mixing ratio of azulene is rather uncertain and therefore also the corresponding detection limit, a comparison using literature values for the absorption cross-sections of azulene to estimate azulene mixing ratios, and detection limits, may still be useful.

Theoretical absorption cross-sections for a number of polycyclic aromatic hydrocarbons that are relevant to astrochemistry, including azulene, have been computed by Mallocci et al. [131–133]. Table 4.2 lists the computed cross-sections,  $\sigma$ , of neutral azulene which fall within the HR range of the cavity mirrors. The values listed show reasonable agreement with the limited experimental values that are available [119, 134, 135], deviating by less than 25%, and can be taken to be sufficient for determination of a rough estimate of the detection limit. Based on these cross-section values, the measured azulene mixing ratios for the IBBCEAS and CRDS measurements were determined to be  $175 \pm 75$  ppbv and  $260 \pm 110$  ppbv, respectively, which are in agreement with the possible range determined above. These values were determined from the mean of the mixing ratio calculated for



$\lambda$ (nm)	$\sigma$ ( $10^{-19}$ cm <sup>2</sup> )
578.2	11.967
592	6.361
606.4	7.428
621.6	6.441
637.5	6.062

TABLE 4.2: Values for the absorption cross-section of azulene within the mirror HR range, from Ref. [133].

each of the values for the absorption cross-section. The error was taken to be twice the standard deviation in this mean. Due to a large deviation in the cross-section at 578.2 nm from that expected based on previous experimental absorption measurements (see Fig. 4.12), a decision was made to exclude this value from the calculations. From these values, and the SNR values determined previously, values for the detection limit of the experimental setup were determined to be  $1.7 \pm 0.7$  ppbv for IBBCEAS, and  $5 \pm 2$  ppbv for CRDS measurements. The error values in the detection limits are derived from the error in the measured mixing ratios.

The detection limits determined via the two different calculation methods are in reasonable agreement, even though the absolute value is uncertain owing to large systematic biases as discussed previously. Both of these calculations yield rough detection limit estimates of the order of 2 ppbv for IBBCEAS measurements, and approximately 5 ppbv for the CRDS approach.

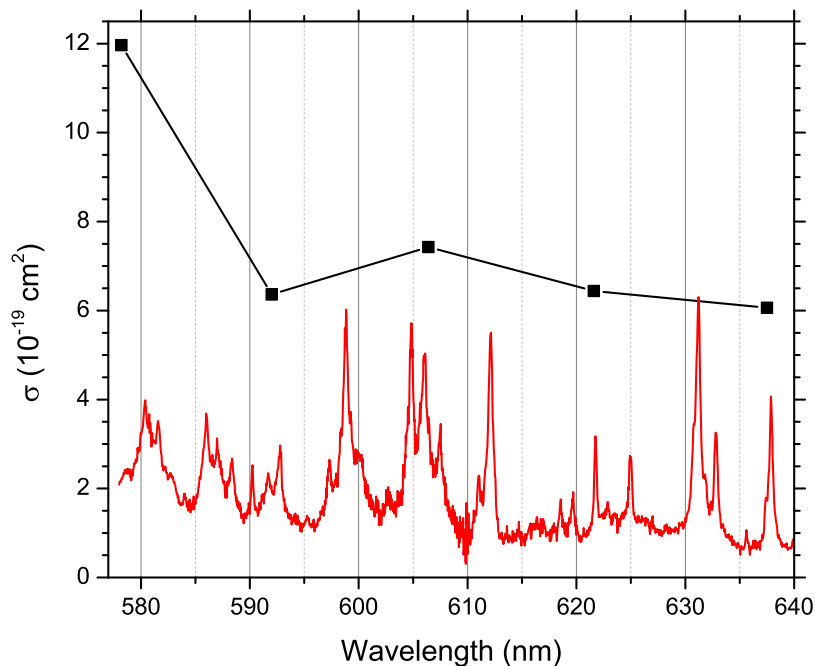


FIGURE 4.12: Black: Absorption cross-section of azulene from Ref. [133]. Red: Vertically scaled CRDS spectrum of jet-cooled azulene from a previous study [126], for comparison. The point at 578.2 nm shows significant deviation from that expected from previous experimental results and has therefore been excluded from any calculations.

## 4.7 Conclusion

The results of the experiments which utilised an LIP as an intra-cavity broadband light source for both time-dependent (CRDS) and intensity-dependent (IBBCEAS) measurements were outlined in this chapter.

The emission from the LIP was found to be well sustained within the cavity, with a measured ring-down time of  $\sim 4 \mu\text{s}$ . The LIP emission sustained in the cavity was used to measure part of the  $S_1 \leftarrow S_0$  absorption spectrum of gaseous azulene via both a step-wise approach to broadband CRDS, and IBBCEAS. The CRDS approach, which had an integration time of  $250 \mu\text{s}$  per step, achieved a signal-to-noise ratio of 51, with a minimum detectable absorption coefficient,  $\varepsilon_{\text{min}} = 7.4 \times 10^{-8} \text{ cm}^{-1}$ . The total measurement time was  $\sim 16$  minutes which corresponds to a noise equivalent absorption of  $2.3 \times 10^{-6} \text{ cm}^{-1} \text{ Hz}^{-\frac{1}{2}}$ .

In comparison to the CRDS approach, the IBBCEAS approach had an increased integration time of 4.5 ms, which resulted in an improved SNR of 104, with a corresponding lower minimum detectable absorption coefficient of  $4.7 \times 10^{-8} \text{ cm}^{-1}$ . This was achieved with a significantly shorter measurement time of 52 s, yielding a noise equivalent absorption of  $3.4 \times 10^{-7} \text{ cm}^{-1} \text{ Hz}^{-\frac{1}{2}}$ . However, absorption measurements with the IBBCEAS approach are complicated by the presence of an artificial offset in the measured absorption which arises due to the necessary delay between plasma formation and data collection, thus allowing light to be absorbed by the absorbing species prior to the measurement. To account for this offset, a method of correcting the measured spectra has been devised which uses the fitting parameters from the reflectivity calibration measurement to determine a wavelength-dependent correction factor for the measured spectra, achieved through a numerical approach. While this procedure does not provide a perfect correction to the measured data, it does bring it more in line with the true value, increasing the suitability of the faster IBBCEAS approach for applications that do not require a very high degree of accuracy in the measured absorption values. Hence, the recommended approach to absorption measurements is to first measure the ring-down time of the cavity without an absorbing sample present to determine the mirror reflectivity and the numerical values necessary for correction of all subsequent measurements with the faster and more sensitive IBBCEAS approach.

The next chapter is concerned with the effects that the LIP has on the propagation of light through the plasma region, and how this influences the sustainment of light within optical cavities, leading to the observed time-dependence in the cavity output intensity which was outlined in this chapter.

## Chapter 5

# Influence of intra-cavity LIPs on the cavity output intensity

As previously discussed at the start of Chapter 4, the work with intra-cavity LIPs as light sources for CEAS [6] yielded a peculiar behaviour of the time-dependent output of *near-confocal* cavities. The intensity of light leaking from the near-confocal cavity exhibited a maximum approximately  $3.6 \mu\text{s}$  after plasma formation with a fs-pulsed laser. The reason for this behaviour was not immediately clear, however, subsequent experiments using LIPs generated by a ns-pulsed laser resulted in a similar time-dependence of the cavity output intensity, albeit with differences in terms of the time scales over which the maximum in the cavity output occurred. As presented in Section 4.3, experiments which utilised an LIP at the centre of a *near-concentric* optical cavity did not result in the same behaviour with the cavity output intensity simply exhibiting a significant decrease in intensity prior to mono-exponential decay (see Fig. 4.3).

These observations yield a number of questions of which the three most significant are to be addressed in this chapter:

- Q1.** Why is a maximum observed in the time-dependence of the *near-confocal* cavity output intensity?

**Q2.** Why is it not observed in the case of (*near*)-*concentric* cavities?

**Q3.** Why does the observed time-dependence of the light leaking from a *near-confocal* cavity differ between cases where the LIP is generated by a fs-pulsed laser, and by a ns-pulsed laser?

The data which have motivated these questions will be briefly reviewed in Section 5.1.

The presence of a maximum in the *near-confocal* cavity output is a direct consequence of the presence of the LIP within the cavity. This unexpected time-dependence in the cavity output is attributed to a combination of both the absorption of light within the cavity by the LIP itself, along with the LIP producing a temporally-varying non-linear refractive index change inside the cavity. This refractive index change manifests as a (net) negative lensing effect. The LIP thereby influences the propagation of light that is resonant within the cavity (cf. CRDS of flames [88–90]) analogous to the effect of a negative lens inside a plasma-free cavity. The lensing effect of the plasma within the cavity results in:

- (i) Additional losses of light sustained by the cavity.
- (ii) Time-varying adverse effects on both the cavity output efficiency (i.e. a reduction in the fraction of light that leaks from the cavity through the output mirror).
- (iii) Adverse effects on the imaging of light leaking from the cavity, thus affecting the detected signal.

A combination of these effects is responsible for the observed time-dependence in the cavity output intensity.

To address **Q1**, a qualitative demonstration of the lensing effect induced by the LIP is provided in Section 5.2 which details the effects that an LIP generated by a ns-pulsed laser has on a probe beam from a helium-neon (He-Ne) laser.

In order to address **Q2**, Section 5.3 outlines the effects of intra-cavity optical elements (a single lens in the form of an LIP in the current case) on the stability

parameters of the cavity. A description of how the light leaking from the cavity is imaged is also included.

The temporal behaviour of the cavity output intensity is found to exhibit some dependence on the cavity geometry (i.e. mirror separation). This relationship between the temporal behaviour of the cavity output and the cavity geometry is explored further in Section 5.4.

An explanation for **Q3** will be discussed in Section 5.4. The differences in the behaviour between LIPs generated by fs-pulsed, and ns-pulsed lasers, is a priori non-trivial, and inherently requires a detailed characterisation of the LIP conditions, including information on parameterisation and dynamics. A key parameter appears to be the laser peak power for the LIP generation. The higher peak pulse power in the case of the fs-pulsed laser produces a much more energetic LIP with a stronger associated electric field. This would expectedly yield a more significant lensing effect from the LIP, thus requiring more time for the light within the cavity to return to a stable resonance.

## 5.1 Summary of observed cavity outputs

This section summarises the observed differences in the time-dependence of the cavity output intensity for (i) different cavity and (ii) LIP formation parameters. It is these observations that motivated the questions **Q1**, **Q2**, and **Q3**.

Fig. 5.1 compares, on a semi-logarithmic plot, the relative cavity output intensity for an LIP generated by a ns-pulsed laser. The upper panel shows the output in the case of a near-concentric cavity ( $L = 79.3$  cm), which corresponds to Fig. 4.3. The lower panel shows the output from a (near-) confocal cavity ( $L = 40$  cm). From these plots it is evident that near-concentric cavities do not exhibit the maximum in the output intensity that is observed in the case of confocal cavities. For completeness, the corresponding ring-down times for each cavity are included

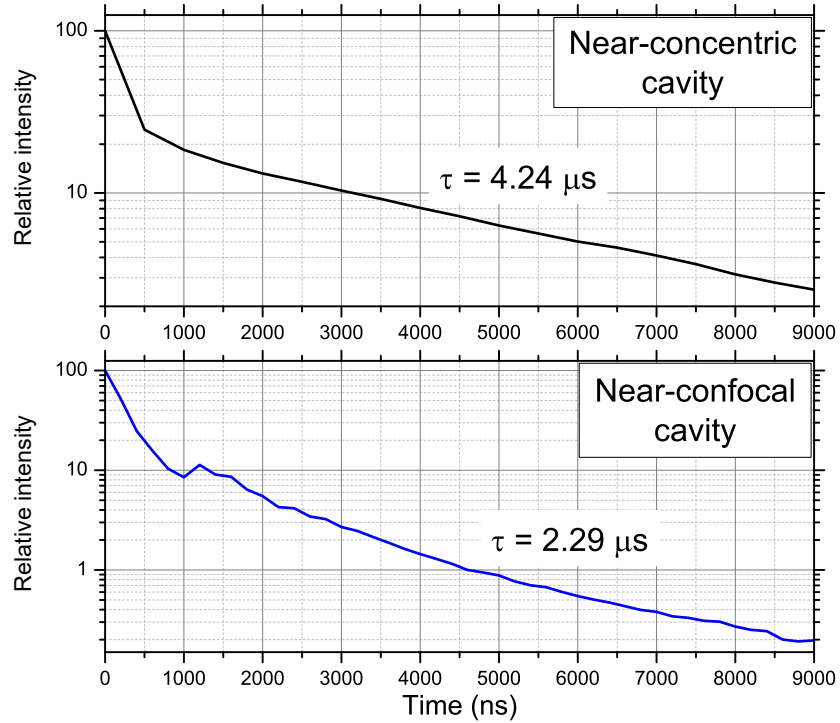


FIGURE 5.1: Relative cavity output intensity for an LIP generated by a ns-pulsed laser at the centre of a near-concentric cavity (upper plot), and a near-confocal cavity (lower plot). The factor of  $\sim 2$  difference between the ring-down times ( $\tau$ ) is a consequence of the factor of 2 difference in cavity length.

in Fig. 5.1, with the approximate factor of 2 difference arising mostly from the factor of two difference in the cavity length.

The absence of a maximum in the output from a near-concentric cavity, led to the supposition that the observed behaviour in a confocal cavity is likely a consequence of the cavity geometry (i.e. the mirror separation). This was confirmed through experiments in which the mirror separation was incrementally increased beyond that of a confocal geometry, yielding a change in the time-dependence of the cavity output. Fig. 5.2 shows the measured cavity output for three cavity lengths (40, 40.1, and 40.2 cm), from which the dependence on cavity length is evident. The data shown were all measured with the same excitation conditions for the LIP. The relationship between the temporal behaviour of the cavity output and the cavity geometry will be explored further in Section 5.4.

The different behaviour of the cavity output between LIPs generated with fs-, and ns-pulsed lasers, is shown in Fig. 5.3. The output from an LIP generated with

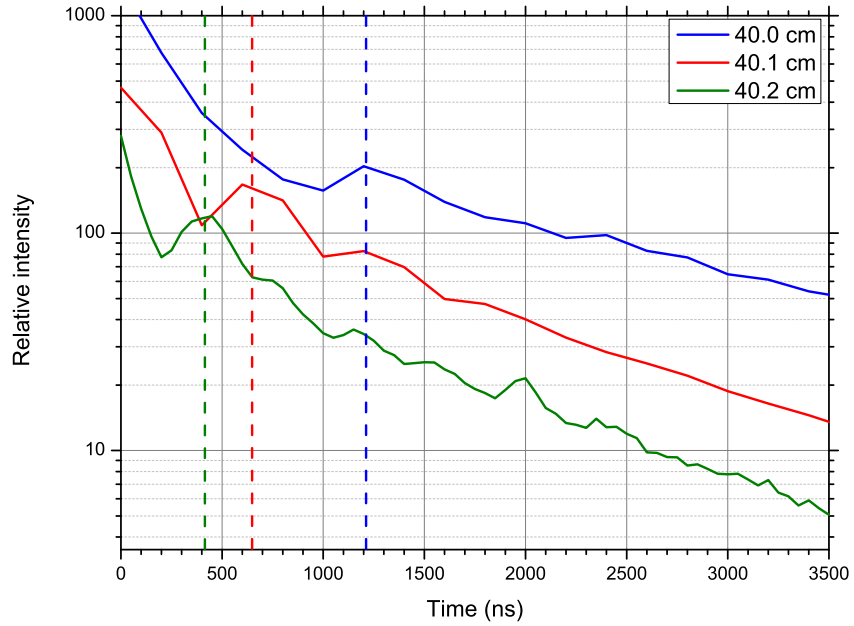


FIGURE 5.2: Time-dependent cavity output intensity for three different cavity lengths showing how the time at which the maximum (indicated by dashed lines) in the output occurs changes with cavity length. A cavity length of 40 cm corresponds to a confocal cavity geometry. LIP generation was provided by a ns-pulsed laser. The three traces have been arbitrarily scaled for clarity.

a fs-pulsed laser at the centre of a confocal cavity is shown in the upper panel [6], while the corresponding output for a ns-pulse LIP is shown in the bottom panel. While both plots show a similar behaviour (which arises from the cavity geometry), there is a significant difference between the times at which the observed maximum occurs. Further details on this difference are provided in Section 5.4.3.



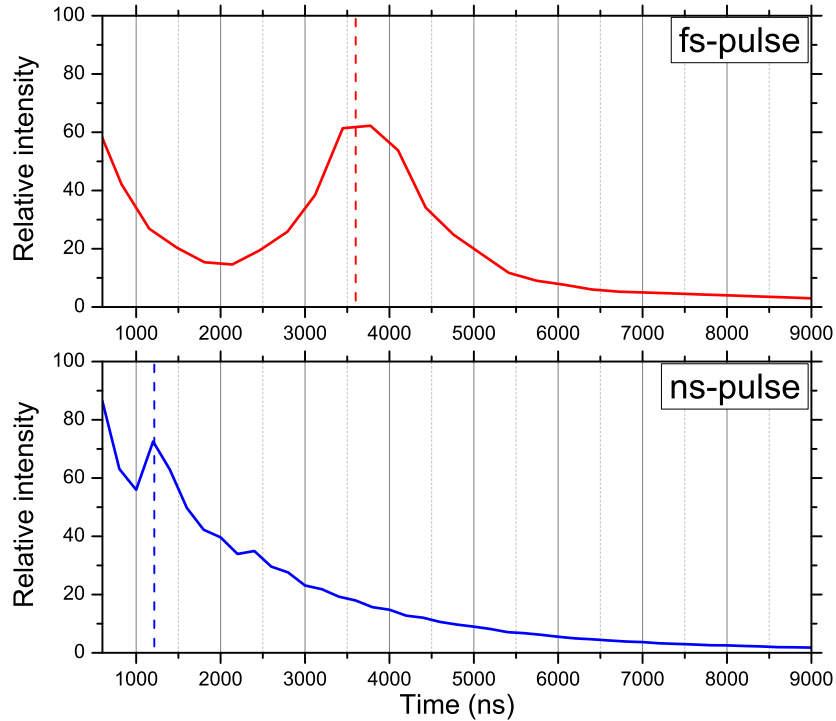


FIGURE 5.3: Comparison of the typical time-dependence of the cavity output intensity for an LIP generated by a fs-pulsed laser (upper plot) and by a ns-pulsed laser (lower plot). In both cases the cavity was in a (quasi-) confocal arrangement with a length of  $\sim 40$  cm.

## 5.2 Demonstration of the lensing effect induced by LIPs

The following section outlines the results of experiments which demonstrate that an LIP (generated by a ns-pulsed laser) effects the propagation of light through, and in the vicinity of, the LIP. The corresponding experimental setup has been described in Section 2.4.

To illustrate the principle of the experimental approach, Fig. 5.4 shows the effect of the LIP on the He-Ne laser probe beam at four different stages:

- (a) Prior to LIP formation, the probe beam propagates freely.
- (b) The LIP presents a significant optical loss, absorbing a portion of the probe beam, while also focusing it to a smaller spot size on the pinhole,

producing an increase in the intensity of light transmitted through the pinhole.

- (c) As the LIP expands and becomes increasingly transparent, the absorption is reduced, while the LIP still acts to focus the probe beam, to some extent.
- (d) After expansion and cooling of the LIP it no longer absorbs nor focuses the probe beam, with the beam radius at the pinhole returning to its initial value, as in (a).

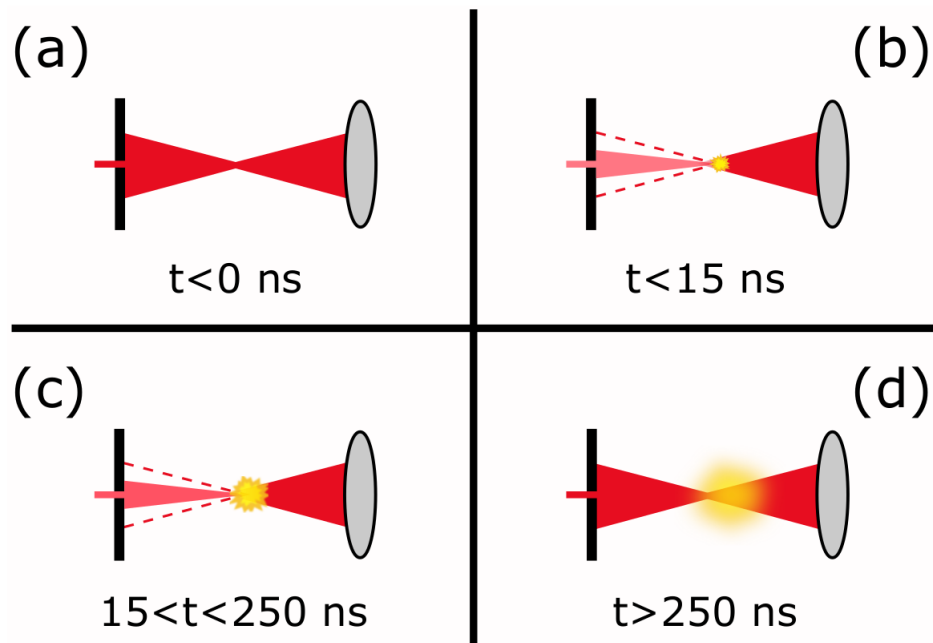


FIGURE 5.4: Schematic illustration of the effect of the LIP on the probe beam, shown at four different stages: (a) before LIP formation, (b) immediately after LIP formation, (c) during LIP expansion, (d) after plasma expansion and cooling. The expected behaviours during each of these stages are described in the main body of the text.

The time-dependent probe beam intensity transmitted through a  $200 \mu\text{m}$  pinhole is shown in Fig. 5.5. Apart from the typical temporal behaviour of the probe beam (red trace), Fig. 5.5 also shows the relative LIP emission intensity (black trace). The relative probe beam intensity in Fig. 5.5 is given as a percentage of the unattenuated beam intensity. In this plot, the four stages in the time-dependence of the LIP formation and evolution illustrated in Fig. 5.4 can be identified (also compare Section 1.3):

- (a) For  $t < 0$  ns (i.e. before LIP formation), the probe beam propagates freely (red area in Fig. 5.5).
- (b) Immediately after LIP formation ( $t < 20$  ns), the LIP absorbs the probe beam, resulting in the initial drop in the measured intensity (blue area in Fig. 5.5). It should be noted that the probe beam diameter is generally larger than the LIP at this early stage, and hence only  $\sim 20\%$  of the light is absorbed.
- (c) As the plasma expands and cools, it becomes more and more transparent, allowing more light to be transmitted through the LIP. However, during this stage the energetic plasma produces a lensing effect, focusing the probe beam to a smaller spot size on the pinhole, increasing the throughput, which is apparent as the significant spike in the detected intensity which coincides with the maximum emission from the LIP (green area in Fig. 5.5).
- (d) Subsequently,  $> 250$  ns after plasma formation, the LIP will have cooled and expanded enough that it becomes essentially transparent, at which point, the probe beam once again propagates freely through the plasma formation region, yielding a return of the measured probe beam intensity to near its measured value prior to LIP formation (yellow area in Fig. 5.5).

### **Lensing by the LIP**

The significant spike in intensity at ca. 30 ns coincides with the maximum emission intensity of the LIP. The spike is interpreted as a result of the lensing effect of the LIP. The lensing effect of the LIP cannot be accurately quantified as this intensity spike is affected by the absorption of the probe beam by the LIP as well. Hence, the absolute intensity of the spike is not truly representative of the lensing effect of the LIP, but merely indicative. However, based upon the relative intensity increase from  $\sim 85$  to  $\sim 125$ , and the unattenuated beam radius at the pinhole, a rough estimate of  $f \approx -3.1$  cm can be determined for the effective focal length of the LIP at the point of maximum intensity, if the simplification that the probe

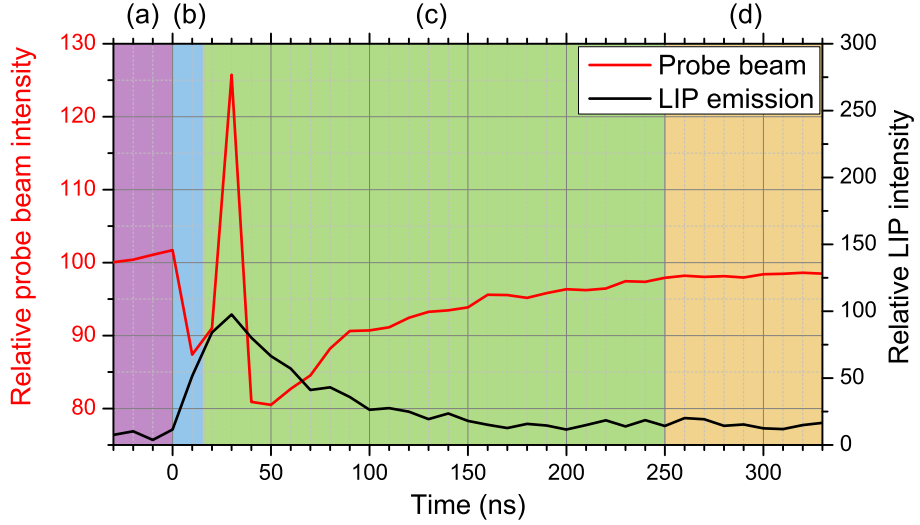


FIGURE 5.5: Red trace: Relative probe beam intensity measured through a  $200\ \mu\text{m}$  pinhole after being focused through an LIP. The spike in intensity is due to the lensing effect of the LIP. Black trace: Scaled time-dependent emission from the LIP. The shaded regions indicate the 4 regimes outlined in the text.

beam intensity at the pinhole is constant across the beam radius is made. In other words, the LIP seems to temporarily act as a negative (concave) lens with a short focal length,  $f$ .

### Absorption by the LIP

The effect of absorption of the probe beam by the LIP is shown in Fig. 5.6 which displays the measured intensity of a *collimated* probe beam passing through the LIP formation region. In this case, the probe beam was not focused, and all of the light from the probe beam is collected (i.e. the pinhole was removed) by the detection system. The probe beam was attenuated by neutral-density filters to reduce its overall intensity. This experiment was done in an effort to circumvent the lensing effect of the LIP in order to determine the duration of the absorption by the LIP. Despite these efforts, there is still the potential for deviation of the probe beam by the LIP which would negatively impact the accuracy of this measurement. The data in Fig. 5.6 suggests that the absorption by the LIP lasts for  $\sim 200$  ns after plasma formation. This is in agreement with the work of Hohreiter et al. [136], although they measured the absorption of an LIP formed by a significantly more energetic laser pulse (pulse energy of 275 mJ, compared to 55 mJ in this study),

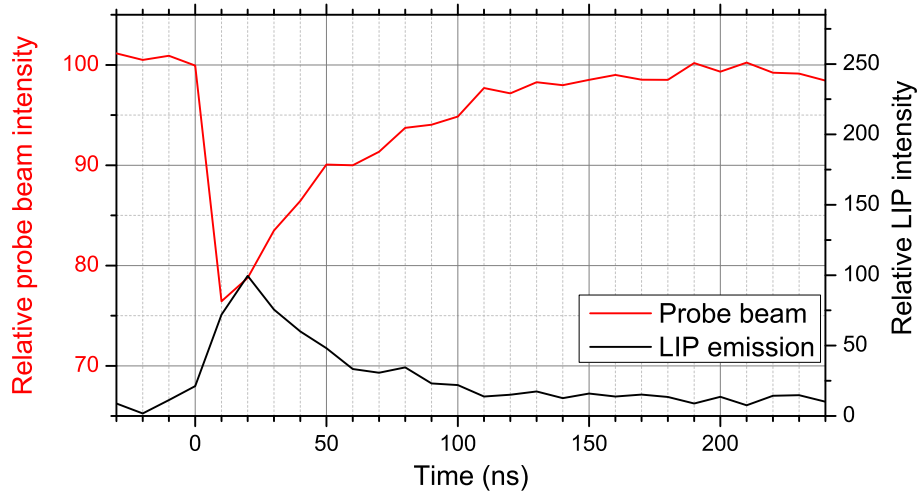


FIGURE 5.6: Relative intensity of a collimated He-Ne probe beam as a percentage of the unattenuated beam intensity (red trace, left-axis) passing through the LIP formation region showing the time-dependent absorption by the LIP. The total (integrated over all accessible wavelengths) emission intensity of the LIP (black trace) is shown for comparison.

which would expectedly yield a longer period of absorption. As before, the probe beam diameter is larger than the plasma dimensions shortly after LIP formation (i.e. when absorbance is highest), which accounts for the  $\sim 75\%$  transmission at the point of maximum absorption.

These lensing and absorption effects of the LIP are the main source of the observations outlined in Section 5.1 for the confocal cavity. The times at which the maxima occur in the cavity output evidently happen much later after LIP formation than the lensing and absorption effects of the LIP. This discrepancy is attributed to some time being required for the perturbed light in the cavity to return to a stable resonance. This aspect will be discussed in Section 5.4.

The following section relates the effects demonstrated to the imaging and stability of optical cavities to address the observed behaviour.

## 5.3 Effects of the LIP on the cavity output intensity

This section provides a discussion of the lensing effect of the LIP and how it influences the propagation of light within optical cavities, yielding the observed time-dependence of the cavity output intensity. First, brief descriptions of how light propagates within both confocal and concentric cavities, in general, will be provided. Then details of how the output from each type of cavity is imaged are outlined, because the lensing effect of the LIP significantly affects the imaging, and thus, the detection conditions. This is also of general interest for maximising the imaging efficiency for this approach to broadband CEAS.

### 5.3.1 Imaging of the cavity output

When comparing confocal and concentric optical cavities, the optical emission from an intra-cavity LIP transmitted through one of the cavity mirrors is imaged differently, depending on the particular cavity geometry. This aspect will be discussed on the basis of geometric optics.

#### Confocal cavity

Fig. 5.7 illustrates the light propagation for a confocal cavity geometry ( $L = r$ ). Light (at a given wavelength) from the LIP formed in the centre of the cavity is first collected by the left-hand (back) mirror and then propagates along a different path within the cavity than light that is first collected by the right-hand (output) mirror, assuming isotropic emission from the LIP. Light first incident upon the back mirror (blue lines in Fig. 5.7) will always travel towards the output mirror parallel to the optical axis, regardless of the number of round trips that the light has made. Hence, the light that is transmitted through the output mirror is also travelling parallel to the optical axis (assuming minimal refraction from the cavity mirror itself), and is imaged by the collecting lens ( $f = 80$  mm) to the focal plane

80 mm away from the lens. Conversely, light that is initially incident upon the output mirror (red lines in Fig. 5.7) will always travel towards the output mirror at an angle that depends on  $L$ . Light transmitted by the output mirror will be focused at a different distance from the collecting lens in comparison to light that travels parallel to the optical axis of the cavity. Based on the cavity length of 40 cm, and a 10 cm separation between the output mirror and the imaging lens, the light will be focused in a plane  $\sim 109$  mm from the lens. This difference in focal positions,  $\Delta f$ , of  $\sim 29$  mm implies that the imaging of the light from the cavity can only be optimised for half of the light that leaks through the cavity output mirror, yielding a reduced overall signal intensity.

This issue with the imaging of light from a confocal cavity is in contrast to the typical CEAS experimental arrangement in which a collimated beam enters the optical cavity through the back mirror, with all light initially travelling parallel to the optical axis. In this case, all of the light leaking through the cavity output mirror is travelling parallel to the optical axis, and is imaged to the same focal plane.

While only shown for one arbitrary wavelength, it can be seen from Fig. 5.7 how chromatic aberrations could manifest in the cavity output due to light of different wavelengths following slightly different paths and being focused to slightly different positions by the collecting lens, further reducing the imaging efficiency. This highlights the importance of employing an achromatic lens for light collection in broadband cavity-based measurements, to minimise these effects.

### **Concentric cavity**

Fig. 5.8 illustrates the propagation of the optical emission from an LIP within an optical cavity in a *concentric* arrangement ( $L = 2r$ ). In this case, light initially incident upon the back mirror, and light incident upon the output mirror both propagate along the same path: passing back and forth through the centre of the cavity. As a result, all of the light that leaks through the output mirror propagates as if it has come from the centre of the cavity (again assuming minimal refraction

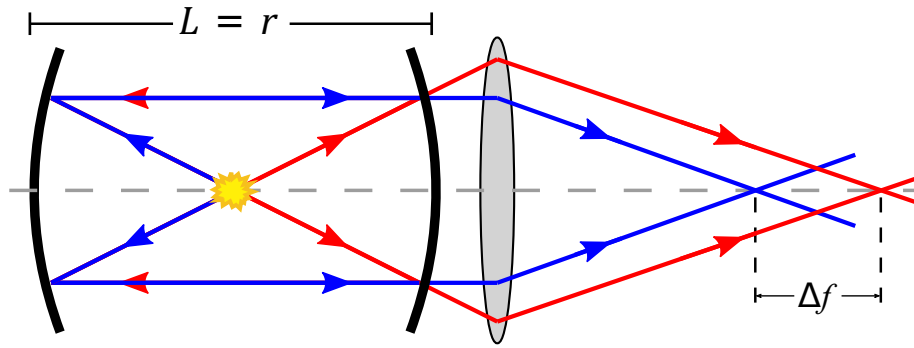


FIGURE 5.7: Illustration (not to scale) of the imaging of the cavity output for the emission from an LIP formed at the centre of a confocal cavity. Blue lines represent the emission from the LIP that initially propagates in the left direction, while red lines represent light travelling to the right. The two different directions yield different focal positions for the imaged light, separated by a distance  $\Delta f$ .

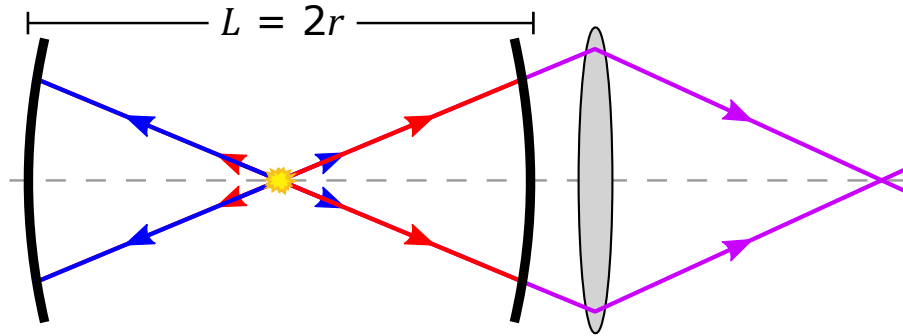


FIGURE 5.8: Illustration (not to scale) of the imaging of the cavity output for an LIP formed at the centre of a concentric cavity. Blue lines represent light emission from the LIP that initially propagates in the left direction, while red lines represent light travelling to the right. The point at which the cavity output is imaged is the same for light travelling in both directions.

from the cavity mirror) and is focused in one and the same focal plane of the collecting lens. With a cavity length of 80 cm, and 10 cm gap between the output mirror and the imaging lens, the resultant focal positions of the cavity output for LIP emission in both directions are coincident at  $\sim 95$  mm from the lens. In this case, the increased imaging efficiency of the output from concentric cavities helps to offset the overall lower collection efficiency of the LIP emission which arises from the increased cavity length (see Eq. 1.9).

For both cases (confocal and concentric), the cavity output imaging efficiency could, in principle, be increased by a factor of 2 by utilising a bifurcated fibre



to simultaneously collect the cavity output from each of the two cavity mirrors. This capability is facilitated by the light injection into the cavity not taking place *through* one of the cavity mirrors; in contrast to standard CEAS approaches (compare Figs. 1.2 and 2.1).

### 5.3.2 Influence of the LIP on optical cavity stability

When considering the propagation of light which is resonant within an optical cavity, the lensing effect of the LIP (see Section 5.2) acts to interfere with the resonant light, yielding an apparent change in the stability parameters of the optical cavity. This leads to increased optical losses and reduced cavity output intensities. The following provides an analysis of these effects, and how they differ between confocal and concentric cavity geometries.

As described in Sections 2.4 and 5.2, the negative lensing effect of the LIP acts to decrease the divergence of the light propagating within the cavity, yielding an apparent mirror separation (cavity length)  $L_{\text{app}} > L$ . In the case of a confocal cavity geometry, this increased cavity length is only applicable to light that is travelling through the LIP region of the cavity, and will therefore only have a significant effect on light that is travelling one direction inside the cavity, while light travelling in the other direction will be largely unaffected (see Fig. 5.7). This results in light travelling e.g. right-to-left experiencing an increase in the apparent cavity length ( $L_{\text{app}}$ ), while the majority of light travelling the opposite direction (parallel to the optical axis) will be largely unaffected by the lensing effects of the LIP, thus experiencing the true cavity length,  $L$ . The LIP at the centre of a cavity hence affects the apparent cavity geometry and therefore also alters its optical stability. In the case of a near-confocal geometry (see Fig. 1.5), the LIP results in an effectively asymmetric resonator (i.e.  $g_1 \neq g_2$ ) and causes the cavity to become temporarily unstable, leading to a significant decrease in output intensity. Hodgson et al. [79] found that confocal resonators are particularly sensitive to deviations in the cavity length, with  $> 1\%$  fluctuations in cavity length resulting in significant losses of output power.

Ref. [137] provides a comprehensive description of optical resonators with internal optical structures. Eq. 5.1, gives the apparent cavity length,  $L_{\text{app}}$ , for a cavity with an internal lens of focal length  $f$ .<sup>5</sup> The corresponding modified  $g$ -parameters,  $G_1$  and  $G_2$ , are provided by Eqs. 5.2a and 5.2b [137]. In Eq. 5.1,  $d_1$  and  $d_2$  represent the respective distances between the internal lens, and the cavity mirrors. In the case of an LIP at the *centre* of the cavity,  $d_1 = d_2 = \frac{L}{2}$ .

$$L_{\text{app}} = d_1 + d_2 - \frac{d_1 d_2}{f} \quad (5.1)$$

$$G_1 = 1 - \frac{L}{r_1} - \frac{d_2}{f} \left(1 - \frac{d_1}{r_1}\right) = g_1 - \frac{d_2}{f} \left(1 - \frac{d_1}{r_1}\right) \quad (5.2a)$$

$$G_2 = 1 - \frac{L}{r_2} - \frac{d_1}{f} \left(1 - \frac{d_2}{r_2}\right) = g_2 - \frac{d_1}{f} \left(1 - \frac{d_2}{r_2}\right) \quad (5.2b)$$

By solving Eq. 5.1 for the current confocal cavity system ( $d_1 = d_2 = 20$  cm), it can be seen that a greater than 1% change in apparent cavity length ( $L_{\text{app}} > 40.4$  cm) would be observed for an effective LIP focal length  $> -1000$  cm. While it was not possible to determine an accurate value for the effective focal length of the LIP from the work in Section 5.2, the rough estimate of  $f \approx -3.1$  cm implies that the LIP represents a much stronger lens than this. Using this estimate for the focal length of the LIP, and assuming that the LIP only affects light travelling one direction in the cavity, yields modified  $g$ -parameters of (3.21, 0). As this cavity is, in principle, on the edge of stability ( $G_1 G_2 = 0$ ), any fluctuation in cavity length (through vibrations, thermal drifts, or otherwise) will result in a temporarily unstable configuration. As the lensing effect of the LIP occurs only over a very short time scale, the cavity returns to a stable condition quite rapidly. Due to this short-lived perturbation, it is expected that the light within the cavity is not totally lost, with a portion of the “perturbed” light (that has not been lost

---

<sup>5</sup> In Eq. 5.1, the sign convention is that a negative value for  $f$  represents a negative (diverging) lens.

through absorption or otherwise) being collected again once the cavity returns to stability. It is this “re-collecting” of light that accounts for the observed maximum in the time-dependent cavity output intensity. Other factors contributing to the observed time-dependence are discussed in Section 5.4 below.

Concentric cavities are generally unaffected by an internal lens at the centre of the cavity as  $\left(1 - \frac{d_i}{r_i}\right) = 0$  in Eqs. 5.2a and 5.2b, thus yielding  $G_i = g_i$ . While in the case of the near-concentric cavity geometry used for the CEAS measurements in Chapter 4 ( $L = 79.3$  cm), the cavity will continue to satisfy the stability criterion ( $0 < G_1 G_2 < 1$ ) provided that the effective focal length of the LIP is less than  $-0.175$  cm which, again, is a reasonable expectation based on the estimate in Section 5.2.

Using the LIP focal length estimate of  $f \approx -3.1$  cm, and assuming that light travelling in both directions interacts with the LIP, yields stability parameters of  $(-0.89, -0.89)$ , which satisfy the cavity stability criterion. As the lensing effect of the LIP does not shift the cavity into an unstable configuration, the initial decrease in the cavity output intensity is due solely to direct absorption of the sustained light by the LIP itself, while the time-dependence seen in the case of a confocal cavity is not observed for a concentric cavity.

## 5.4 Time-dependence of the cavity output intensity

Fig. 5.1 (lower panel) shows the time-dependent cavity output intensity measured for an LIP formed with a ns-pulsed laser, at the centre of a confocal cavity, with a mirror separation of 40 cm. A maximum occurs in the cavity output intensity, similar to that observed in the case of LIP formation with a fs-pulsed laser (Fig. 5.3) [6]. However, in this case the observed increase/decrease of the intensity occurs on a different time-scale (see Fig. 5.3). Potential reasons for this difference are based on the LIP excitation process and will be discussed in Section 5.4.3.

The maximum in the output intensity arises due to the LIP interfering with the propagation of light within the cavity, thus yielding a reduced cavity output intensity during, and for some time after, the LIP's presence within the cavity. Therefore, rather than the LIP producing an increase in the cavity output intensity, it should be regarded as the LIP inducing a decrease in the output intensity, and that this "maximum" is in fact the cavity output returning to the value expected if there were no perturbation from the LIP.

#### 5.4.1 Cavity length dependence

While the reason for the unusual output intensity for near-confocal cavities is due to the effects that the LIP has on the stability of the cavity, the exact timing of the effect is not clearly understood. The cavity output intensity was observed (see Fig. 5.2) to be dependent on the mirror separation. In Fig. 5.2, the intensity maximum shifted significantly from  $\sim 1200$  ns after LIP formation for the confocal cavity ( $L = 40$  cm) to a delay time of  $\sim 400$  ns for the cavity with a length of 40.2 cm. It can thus be concluded that the time at which the maximum occurs is dependent mainly on the cavity geometry. This is further evident in Fig. 5.9 which shows the time at which the maximum in the output intensity occurs measured for a number of cavity lengths from 40 cm to 40.2 cm, showing a clear relationship with the cavity geometry. While the time at which the maximum occurs as a function of the cavity length may be empirically described by an exponential function, it has not been possible to determine an analytical interpretation for this relationship. Possible reasons for this dependence are:

(i) *Cavity alignment*

The observed times are somewhat dependent on the particular alignment of the cavity, with small changes in alignment (e.g. a slight deviation of one of the cavity mirrors) causing the intensity maximum to shift to different delay times. For example, in a number of independent measurements using a confocal cavity, the intensity maxima occurred in the range of 900 – 1700 ns after LIP formation.

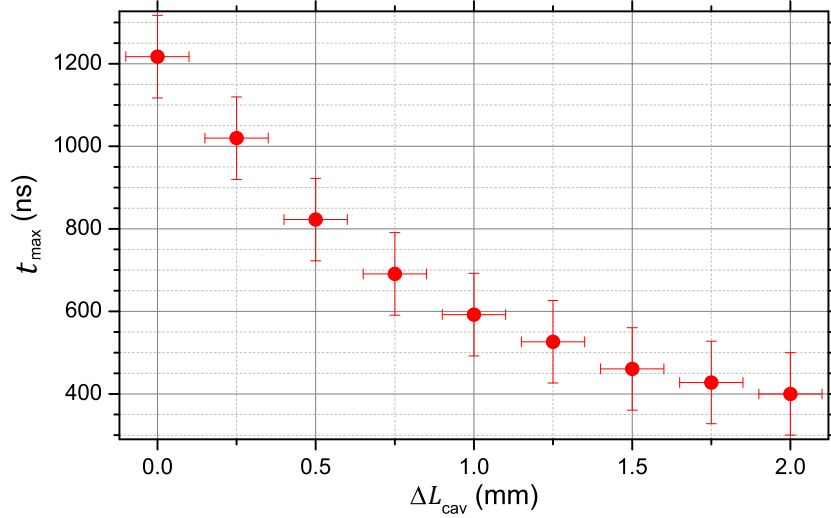


FIGURE 5.9: Time at which the maximum occurs in the cavity output intensity as a function of the mirror separation for near-confocal arrangements ( $L \geq 40$  cm), measured for an LIP generated with a ns-pulsed laser.

The only variable between these measurements was the “quality” of the cavity alignment.

(ii) *LIP position and shape*

The LIP not being exactly at the centre of the cavity may have some influence. However, other tests have shown that small movements of the LIP position have little effect on the time-dependence of the cavity output intensity. The anisotropy of the LIP may make some contribution, but it has not been possible to characterise this effect.

(iii) *Effects on cavity stability*

As the cavity length is increased, the perturbation from the LIP has a diminishing effect on the stability of the cavity, resulting in the cavity returning to stability at a faster rate. Based on this, Eqs. 5.2a and 5.2b can be solved, assuming  $f = -3.1$  cm, to show that the lensing effects of the LIP will no longer yield an unstable cavity for  $L > 67.6$  cm.

## 5.4.2 Time at which maxima occur in cavity output

As for why the intensity maxima are observed after delay times of the order of  $1 \mu\text{s}$  while the lensing effects of the LIP only occur over tens of nanoseconds (see Fig. 5.5), the presumption is that this is due to the perturbed light within the cavity requiring some time to return to a stable resonance after the effects of the LIP have ceased. From Fig. 5.1, it can be seen that the initial steep decrease in intensity, which arises due to direct absorption of light by the LIP, occurs over the first few hundred nanoseconds after plasma formation, which is consistent with the absorption time-scale observed in Fig. 5.6. After this point, light is propagating freely within the cavity, and the lensing effects of the LIP have long since ceased. Hence the light within the cavity can be considered to be returning to a stable  $E$ -field distribution. The remainder of the delay time until the maximum occurs is attributed to the time required for the perturbed light within the cavity to “relax” to a stable resonance, during which time the measured cavity output intensity is diminished.

Fig. 5.10 shows a simulation of how the beam diameter of light within a quasi-confocal cavity varies in time after light is injected into the cavity. The data was generated using the beam propagation method of Fox and Li [138, 139], which computes the mode structure of a resonator by iteratively propagating the wavefront, in small steps, through the cavity, between the cavity mirrors (LASCAD [140]). For this simulation, the beam propagation was simulated for 108 round-trips of the cavity, with a simulation step-size of 5 mm. While this treatment is not totally analogous to the current situation, it is assumed that light affected by the LIP will undergo similar behaviour. From Fig. 5.10 it can be seen that the light takes  $\sim 200 \text{ ns}$  to relax to a stable mode of propagation. As the values in this simulation are only relative, no absolute value has been attributed to the intra-cavity beam diameter.

The lensing effect and the absorption of light by the LIP, as well as the relaxation time of perturbed light have all been identified as contributory factors to the

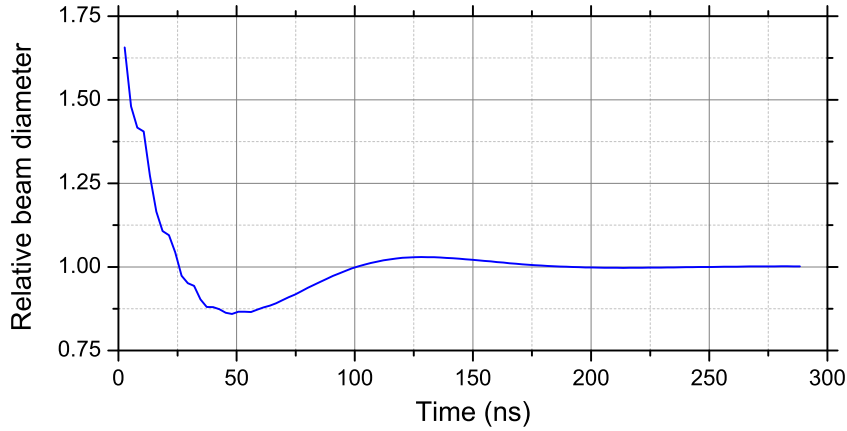


FIGURE 5.10: Simulation of the intra-cavity beam diameter of light propagating (5 mm step-size) within a quasi-confocal cavity showing the time required for light to reach a stable mode of propagation.

observed time-delays. Since a combination of these factors does not fully account for the observed time-delays, it is expected that some other unidentified processes are also involved in the observed time-dependence. These unidentified factors may also contribute to the cavity geometry dependence of the output intensity.

### 5.4.3 Difference in time-dependence between fs-, and ns-generated LIPs

The typical time-dependence of the cavity output for an LIP generated at the centre of a confocal cavity by a fs-pulsed laser is generally similar to that of an LIP generated by a ns-pulsed laser, albeit occurring over a longer time (output maximum at  $\sim 3.6 \mu\text{s}$ , compared to  $\sim 1.2 \mu\text{s}$  for a ns-LIP, see Fig. 5.3). The reasons for this difference are not immediately clear, although it is likely that it is a consequence of the lensing effects described above being more pronounced in the case of a fs-LIP.

In the case of LIP formation with a fs-pulsed laser, the expected plasma temperature is lower due to less absorption of laser light by the LIP, arising from the much shorter pulse duration, i.e. the laser pulse duration is of a similar order of magnitude as the plasma formation process, leading to minimal absorption of

laser radiation after the LIP becomes opaque [141, 142]. Through use of the Boltzmann plot method (see Section 3.2.1), the temperature of an LIP generated by the 200 fs Nd:glass laser described in Section 2.1.1.1 was determined to be merely  $52100 \pm 22000$  K immediately after plasma formation. Fig. 5.11 shows the emission spectra used to determine the temperature of the fs-LIP. The LIP emission in Fig. 5.11 decays much faster than that of the ns-LIP ( $\tau \sim 20$  ns, compared to  $\sim 70$  ns in the ns-LIP case). The temperature of the LIP can be compared to the value of  $63500 \pm 24000$  K obtained for the ns-LIP temperature. While the temperature of the LIP is lower, the short pulse duration yields a significantly increased power density of  $\sim 1.8 \times 10^{15}$  W/cm<sup>2</sup> (compared to  $7.8 \times 10^{11}$  W/cm<sup>2</sup> for the ns laser) which could, in principle, lead to a more energetic LIP with an increased population of higher ionisation states. This LIP may in turn produce a comparatively stronger electric field in the vicinity of LIP, leading to a more significant non-linear refractive index change (lensing effect), thus accounting for the observed increase in delay times between LIP formation and the maxima in the cavity output.



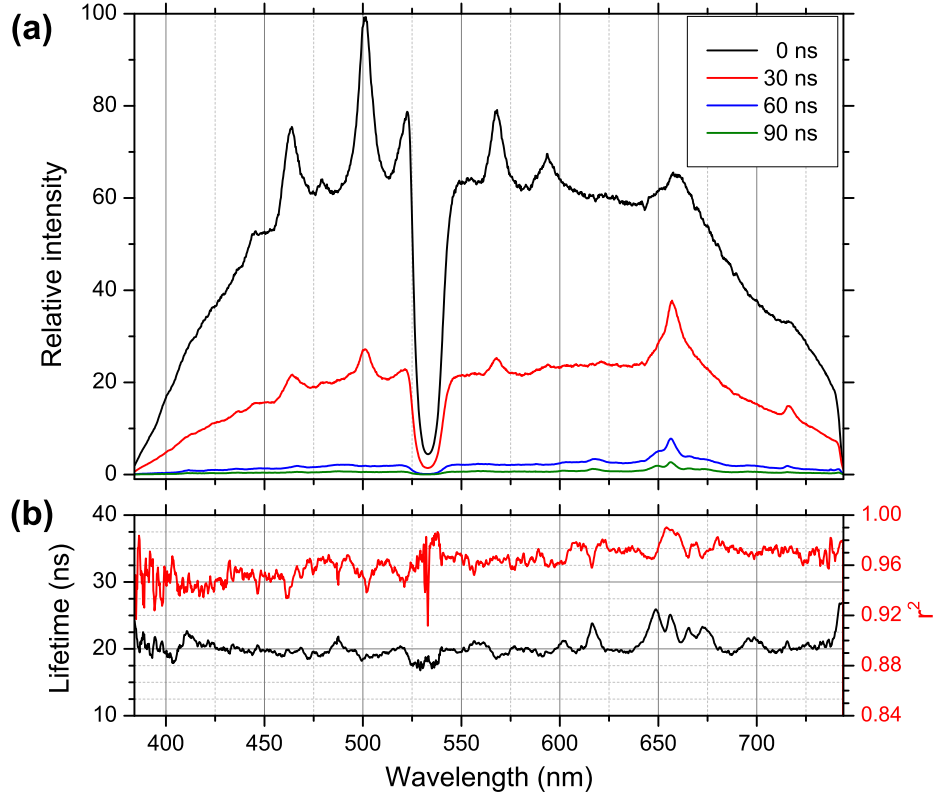


FIGURE 5.11: **(a)** Emission spectrum from an LIP generated by a fs-pulsed laser, measured in steps of 30 ns from immediately after plasma formation. The dip at  $\sim 535$  nm is due to a notch filter to filter out stray laser light. **(b)** Black: LIP emission decay lifetime determined from a mono-exponential fit to the measured spectra. Red:  $r^2$  values for the mono-exponential fit.

## 5.5 Conclusion

The time-dependence of the cavity output intensity was observed to be dependent on both the cavity geometry (mirror separation), and the LIP formation laser pulse length. This dependence arises from a localised non-linear refractive index change (lensing effect) induced by the LIP and absorption of light by the LIP, which act to interfere with the propagation of light within optical cavities. It was demonstrated that the lensing effect of the LIP occurs within the first  $\sim 40$  ns after LIP formation, and was found to take the form of a strong negative lens ( $f \approx -3.1$  cm). The plasma absorbs light for  $\sim 200$  ns.

These effects yield the observed behaviour of the cavity output by affecting both the effective stability of the cavity, and the imaging of the light that is output

from the cavity. As the cavity length is varied, the effects on the cavity stability are also varied in turn, which accounts for the observed cavity length dependence. It was shown that for *near-concentric* cavities, the lensing effect of the LIP does not result in an apparent unstable configuration, thus accounting for the lack of an observed maximum in the time-dependence of the cavity output in these cases.

For LIPs formed at the centre of *near-confocal* cavities, the time-dependence of the cavity output is observed to differ between LIPs formed by fs-, and ns-pulsed lasers. In these experiments, the intensity maxima were observed at  $\sim 1.2 \mu\text{s}$  for a ns-pulsed laser, and  $\sim 3.6 \mu\text{s}$  in the case of a fs-pulsed laser. This difference is attributed mainly to the significantly larger electric field associated with the fs-laser case arising from the more energetic LIP. This is a consequence of the increased power density of the laser formation laser ( $\sim 1.8 \times 10^{15} \text{ W/cm}^2$ , compared to  $\sim 7.8 \times 10^{11} \text{ W/cm}^2$  for the ns-laser). However, as of yet unidentified factors may also contribute.

# Chapter 6

## Summary and conclusion

### 6.1 Summary

In this thesis, the use of laser-induced plasmas as intra-cavity light sources for cavity-enhanced absorption spectroscopy was investigated. The work was motivated by the objective of finding a way to increase the coupling of incoherent light to high-finesse optical cavities by generating a broadband pulse of light, in the form of a laser-induced plasma, at the centre of an optical cavity for cavity-enhanced absorption spectroscopy measurements. While proof of concept experiments utilised an LIP generated by a fs-pulsed laser [6], this work focused on the use of a ns-pulsed laser, which would expectedly produce a far larger LIP, with a substantially increased emission intensity. The use of the ns-LIP as an intra-cavity light source was demonstrated for both cavity ring-down spectroscopy and incoherent broadband cavity-enhanced absorption spectroscopy. The increased emission intensity of LIPs generated with ns-pulsed lasers contributed to a significant improvement in the signal-to-noise ratio of measured spectra when compared to the previous experiments [6] that utilised a fs-LIP.

The LIP generated with a ns-pulsed laser was characterised in terms of its temporal behaviour and emission stability to confirm its suitability as a light source

for CEAS measurements, as presented in *Chapter 2*. During typical operation, the focused pulses from the ns-laser corresponded to a power density of  $\sim 7.8 \times 10^{11} \text{ W/cm}^2$  which compared favourably with literature values for the breakdown threshold of air. Descriptions of the experimental approaches to applying the LIP to the two different CEAS techniques were also provided, along with a description of the experimental setup used to investigate the time-varying effects of the LIP on the propagation of light.

*Chapter 3* further expanded on the suitability of the LIP generated by the ns-pulsed laser, focusing on the properties of the broadband continuum emission from the LIP. The temporal evolution of the broadband continuum emission from the LIP at short delay times ( $t < 200 \text{ ns}$ ) was found to differ from that at longer delay times. For short and long delay times, the LIP emission had decayed with  $\tau \approx 70 \text{ ns}$  and  $\tau \approx 600 \text{ ns}$ , respectively. This difference was attributed to the rapid expansion of the LIP that occurs immediately after plasma formation contributing to a faster decay of the LIP emission, while at longer delay times the plasma decay is solely due to radiative cooling. The thermal evolution of the LIP yields a wavelength-dependence in the temporal evolution of the LIP emission spectra. During cooling of the LIP, the emission maximum of the (blackbody) LIP shifts to longer wavelengths, as described by Wien's law. As a result, the emission appears to decay at a slower rate towards longer wavelengths. The Boltzmann plot method for determining the plasma temperature based on the relative intensities of a number of the atomic and ionic emission lines which are overlaid upon the broadband LIP continuum emission was also outlined in this chapter. This was used to calculate the LIP temperature from 0 to 1250 ns after plasma formation, during which time it decayed from an initial temperature of  $63500 \pm 24000 \text{ K}$  to  $6600 \pm 900 \text{ K}$ . The decay of the LIP temperature was adequately described by a mono-exponential decay with a decay constant of  $440 \pm 45 \text{ ns}$ .

The results of the experiments which utilised the LIP as an intra-cavity light source for CEAS to measure the absorption spectrum of gaseous azulene in ambient air were outlined in *Chapter 4*. Despite the optical losses posed by the LIP, light was found to be sustained in the cavity for more than  $12 \mu\text{s}$ ; sufficiently long for

CEAS measurements. The broadband ring-down time of the light within the cavity ( $\tau \approx 4 \mu\text{s}$ ) provides a simple means of calibrating effective mirror reflectivities *in situ*, thus facilitating absolute absorption measurements via IBBCEAS. The measured ring-down times corresponded to a mirror reflectivity of  $\sim 0.9994$ .

The use of the LIP was successfully applied to broadband CRDS measurements of gaseous azulene, in which the time-dependent cavity output spectrum was measured through a number of independent measurements. This approach to CRDS was inhibited by the requirement to measure the decaying spectra in a stepwise approach, which contributed to excessive measurement times ( $\sim 16$  mins), and increased noise levels due to the relatively short integration time ( $250 \mu\text{s}$ ) per step. The CRDS measurement achieved an SNR of 51 with a minimum detectable absorption coefficient of  $7.4 \times 10^{-8} \text{ cm}^{-1}$ . The corresponding noise equivalent absorption was  $2.3 \times 10^{-6} \text{ cm}^{-1} \text{ Hz}^{-\frac{1}{2}}$ .

Also demonstrated was the use of the LIP for IBBCEAS measurements, in which the cavity output was integrated to produce an absorption spectrum. When compared to the CRDS approach, this intensity-dependent CEAS method provided a significant improvement in terms of measurement time, with a total measurement time of 52 s, along with an increased integration time of 4.5 ms. This yielded an increased SNR of 104, and hence a decreased minimum detectable absorption coefficient of  $4.7 \times 10^{-8} \text{ cm}^{-1}$ . This yielded a noise equivalent absorption of  $3.4 \times 10^{-7} \text{ cm}^{-1} \text{ Hz}^{-\frac{1}{2}}$ .

An inherent flaw to the IBBCEAS approach is the need to wait a not insignificant length of time between LIP formation and the commencement of data collection. This delay is necessitated by the non-Lambert-Beer conditions immediately after LIP formation. During this delay time, the light that is resident within the cavity interacts with the absorbing species which introduces an offset into IBBCEAS spectra that are measured via this approach. In contrast, as the CRDS approach is independent of the cavity output intensity it does not exhibit any offset in the measured spectra and hence can be considered to provide a better measure of the true

absorption coefficient values. With this in mind, a correction procedure was outlined which used the fitting parameters (decay constant and  $y$ -intercept) obtained from the cavity mirror reflectivity calibration to extrapolate values for the integrated cavity output intensities during the delay time between LIP formation and data collection. These integrated values represent that which would be expected if the cavity output was to decay mono-exponentially from immediately after LIP formation. While this procedure does not provide a perfect correction to the data, it does greatly reduce the measurement offset, bringing the measured absorption more in line with the true value. With this correction procedure, calibration of the effective mirror reflectivity facilitates absolute absorption measurements with the much faster, and more sensitive, IBBCEAS approach.

In CEAS experiments which utilise intra-cavity LIPs, the time-dependence of the cavity output intensity exhibited a peculiar behaviour which was observed to be dependent on both the cavity geometry and the pulse length of the LIP formation laser. This behaviour was attributed to the effects of the LIP on the propagation of light within the cavity. In *Chapter 5*, the results of experiments which were used to demonstrate the effect that the presence of an LIP has on the propagation of light through or near the plasma formation region were outlined. The effects of the LIP take the form of both a lensing effect that occurs within the first  $\sim 40$  ns after LIP formation, and direct absorption by the LIP that lasts for  $\sim 200$  ns. The lensing effect arises due to a localised non-linear refractive index change induced by the high temperatures and strong electric fields associated with the LIP formation. The LIP was found to be equivalent to a negative (concave) lens with a focal length  $f \approx -3.1$  cm.

The effects from the LIP temporarily affect both the stability of the optical cavity and the imaging of the light that is output from the cavity. These two aspects are both in turn dependent on the cavity geometry, which yields the observed changes in the cavity output temporal behaviour as the cavity length is varied. The lensing effect of the LIP does not result in an apparent unstable configuration for near-concentric cavities, thus accounting for the lack of an observed maximum in the time-dependent output from these cavities.

A significant difference was observed in the cavity output from near-confocal cavities with LIPs generated with fs-, and ns-pulsed lasers. In the case of a fs-pulsed laser, a maximum was observed in the output  $\sim 3.6 \mu\text{s}$  after plasma formation [6], while it was observed at  $\sim 1.2 \mu\text{s}$  in the case of a ns-pulsed laser. This is likely a consequence of the significantly increased electric field in the fs-laser case, arising from the  $\sim 3$  orders of magnitude increase in the power density of the LIP formation pulse ( $\sim 1.8 \times 10^{15} \text{ W/cm}^2$ , compared to  $\sim 7.8 \times 10^{11} \text{ W/cm}^2$  for the ns-pulsed laser), thus resulting in a more significant lensing effect from the LIP.

From the work in Chapter 5 it is clear that these effects from the LIP, and hence the required delay between LIP formation and data collection arising due to the time-dependence of the cavity output, are unavoidable complications of this approach to CEAS. However, the use of a *ns-pulsed* laser for LIP formation, and a *near-concentric* cavity geometry provide a marked reduction in the required delay time compared to the previous work with a fs-pulsed laser [6], thus reducing the negative impact of the delay.

## 6.2 Conclusion

The use of nanosecond laser-induced plasmas as intra-cavity light sources for cavity-enhanced absorption spectroscopy measurements has been demonstrated. The significant increase in brightness of the nanosecond-LIP provides a marked increase in the SNR values when compared to previous absorption measurements which utilised an LIP generated by a femtosecond laser pulse. Additionally, the use of a ns-pulsed laser with a *near-concentric* cavity geometry greatly reduced the necessary delay time between LIP formation and data collection, thus increasing the overall amount of usable light and, in turn, the achievable SNR values.

Based on the absorption of gaseous azulene it was demonstrated that both broadband intensity-dependent (IBBCEAS), and time-dependent (CRDS), measurement schemes can be implemented with the LIP approach. While the IBBCEAS implementation appears to be superior in comparison to the CRDS owing to the

achievable SNR and reduced measurement times, it is hampered by the need to first calibrate cavity mirror reflectivities and the presence of an offset in measured absorption values that must be accounted for. The CRDS capabilities of this approach enable the calibration of the effective cavity mirror reflectivities in situ, which in turn facilitates absolute absorption measurements with the faster, and less prone to noise, IBBCEAS implementation. Thus, a combination of both the IBBCEAS and CRDS implementations provides the best overall performance for this approach to CEAS.

While this approach to IBBCEAS has not exceeded other more established IBBCEAS implementations in terms of performance, the achievable detection limits, combined with the simple means of calibrating mirror reflectivities in situ, make LIP-based cavity-enhanced absorption measurements a useful alternative to other methodologies.



# Bibliography

- [1] S. E. Fiedler, A. Hese, and A. A. Ruth, “Incoherent broad-band cavity-enhanced absorption spectroscopy,” *Chem. Phys. Lett.* **371**, 284–294 (2003).
- [2] S. E. Fiedler, A. Hese, and A. A. Ruth, “Incoherent broad-band cavity-enhanced absorption spectroscopy of liquids,” *Rev. Sci. Instrum.* **76**, 023107 (2005).
- [3] J. Orphal and A. A. Ruth, “High-resolution Fourier-transform cavity-enhanced absorption spectroscopy in the near-infrared using an incoherent broad-band light source,” *Opt. Express* **16**, 19232–19243 (2008).
- [4] A. A. Ruth and K. T. Lynch, “Incoherent broadband cavity-enhanced total internal reflection spectroscopy of surface-adsorbed metallo-porphyrins.” *Phys. Chem. Chem. Phys.* **10**, 7098–7108 (2008).
- [5] A. A. Ruth, S. Dixneuf, and R. Raghunandan, “Broadband Cavity-Enhanced Absorption Spectroscopy with Incoherent Light,” in *Cavity-Enhanced Spectroscopy and Sensing*, G. Gagliardi and H. Loock, eds. (Springer, Berlin, Heidelberg, 2014).
- [6] A. A. Ruth, S. Dixneuf, and J. Orphal, “Laser-induced plasmas in ambient air for incoherent broadband cavity-enhanced absorption spectroscopy,” *Opt. Express* **23**, 6092–6101 (2015).
- [7] A. O’Keefe and D. A. G. Deacon, “Cavity ring-down optical spectrometer for absorption measurements using pulsed laser sources,” *Rev. Sci. Instrum.* **59**, 2544–2551 (1988).

- [8] M. Snee, S. Hannemann, E. J. van Duijn, and W. Ubachs, “Deep-ultraviolet cavity ringdown spectroscopy,” *Opt. Lett.* **29**, 1378–1380 (2004).
- [9] R. Engeln, E. van den Berg, G. Meijer, L. Lin, G. M. H. Knippels, and A. F. G. van der Meer, “Cavity ring down spectroscopy with a free-electron laser,” *Chem. Phys. Lett.* **269**, 293–297 (1997).
- [10] T. Yu and M. C. Lin, “Kinetics of phenyl radical reactions studied by the cavity-ring-down method,” *J. Am. Chem. Soc.* **115**, 4371–4372 (1993).
- [11] S. M. Ball, I. M. Povey, E. G. Norton, and R. L. Jones, “Broadband cavity ringdown spectroscopy of the  $\text{NO}_3$  radical,” *Chem. Phys. Lett.* **342**, 113–120 (2001).
- [12] S. Spuler, M. Linne, A. Sappey, and S. Snyder, “Development of a cavity ringdown laser absorption spectrometer for detection of trace levels of mercury,” *Appl. Opt.* **39**, 2480–2486 (2000).
- [13] H. Linnartz, T. Motylewski, and J. P. Maier, “The  $^2\Pi \leftarrow X^2\Pi$  electronic spectra of  $\text{C}_8\text{H}$  and  $\text{C}_{10}\text{H}$  in the gas phase,” *J. Chem. Phys.* **109**, 3819–3823 (1998).
- [14] T. Motylewski and H. Linnartz, “Cavity ring down spectroscopy on radicals in a supersonic slit nozzle discharge,” *Rev. Sci. Instrum.* **70**, 1305–1312 (1999).
- [15] H. Dahnke, D. Kleine, P. Hering, and M. Mürtz, “Real-time monitoring of ethane in human breath using mid-infrared cavity leak-out spectroscopy,” *App. Phys. B* **72**, 971–975 (2001).
- [16] G. Meijer, M. G. H. Boogaarts, R. T. Jongma, D. H. Parker, and A. M. Wodtke, “Coherent cavity ring down spectroscopy,” *Chem. Phys. Lett.* **217**, 112–116 (1994).
- [17] A. D. Sappey, E. S. Hill, T. Settersten, and M. A. Linne, “Fixed-frequency cavity ringdown diagnostic for atmospheric particulate matter,” *Opt. Lett.* **23**, 954–956 (1998).

- [18] G. P. Miller and C. B. Winstead, “Inductively coupled plasma cavity ring-down spectrometry,” *J. Anal. At. Spectrom.* **12**, 907–912 (1997).
- [19] P. Birza, T. Motylewski, D. Khoroshev, A. Chirokolava, H. Linnartz, and J. P. Maier, “Cw cavity ring down spectroscopy in a pulsed planar plasma expansion,” *Chem. Phys.* **283**, 119–124 (2002).
- [20] R. Engeln, G. von Helden, A. J. A. van Roij, and G. Meijer, “Cavity ring down spectroscopy on solid C<sub>60</sub>,” *J. Chem. Phys.* **110**, 2732–2733 (1999).
- [21] A. J. Hallock, E. S. Berman, and R. N. Zare, “Direct monitoring of absorption in solution by cavity ring-down spectroscopy,” *Anal. Chem.* **74**, 1741–1743 (2002).
- [22] D. Romanini, A. A. Kachanov, N. Sadeghi, and F. Stoeckel, “CW cavity ring down spectroscopy,” *Chem. Phys. Lett.* **264**, 316–322 (1997).
- [23] J. W. Hahn, Y. S. Yoo, J. Y. Lee, J. W. Kim, and H.-W. Lee, “Cavity ringdown spectroscopy with a continuous-wave laser: calculation of coupling efficiency and a new spectrometer design,” *Appl. Opt.* **38**, 1859–1866 (1999).
- [24] Y. He and B. J. Orr, “Ringdown and cavity-enhanced absorption spectroscopy using a continuous-wave tunable diode laser and a rapidly swept optical cavity,” *Chem. Phys. Lett.* **319**, 131–137 (2000).
- [25] J. J. Scherer, J. B. Paul, H. Jiao, and A. O’Keefe, “Broadband ringdown spectral photography,” *Appl. Opt.* **40**, 6725–6732 (2001).
- [26] R. Engeln and G. Meijer, “A Fourier transform cavity ring down spectrometer,” *Rev. Sci. Instrum.* **67**, 2708–2713 (1996).
- [27] A. Czyżewski, S. Chudzyński, K. Ernst, G. Karasiński, L. Kilianek, A. Pietruczuk, W. Skubiszak, T. Stacewicz, K. Stelmaszczyk, B. Koch, and P. Rairoux, “Cavity ring-down spectrography,” *Opt. Commun.* **191**, 271–275 (2001).

- [28] K. K. Lehmann, G. Berden, and R. Engeln, in *Cavity Ring-Down Spectroscopy: Techniques and Applications*, G. Berden and R. Engeln, eds. (John Wiley & Sons, Chichester, UK, 2009), chap. 1.
- [29] T. Gherman and D. Romanini, “Mode-locked cavity-enhanced absorption spectroscopy,” *Opt. Express* **10**, 1033–1042 (2002).
- [30] A. O’Keefe, “Integrated cavity output analysis of ultra-weak absorption,” *Chem. Phys. Lett.* **293**, 331–336 (1998).
- [31] J. E. Thompson and H. D. Spangler, “Tungsten source integrated cavity output spectroscopy for the determination of ambient atmospheric extinction coefficient,” *Appl. Opt.* **45**, 2465–2473 (2006).
- [32] T. Gherman, D. S. Venables, S. Vaughan, J. Orphal, and A. A. Ruth, “Incoherent broadband cavity-enhanced absorption spectroscopy in the near-ultraviolet: Application to HONO and NO<sub>2</sub>,” *Environ. Sci. Technol.* **42**, 890–895 (2008).
- [33] J. M. Langridge, T. Laurila, R. S. Watt, R. L. Jones, C. F. Kaminski, and J. Hult, “Cavity enhanced absorption spectroscopy of multiple trace gas species using a supercontinuum radiation source,” *Opt. Express* **16**, 10178–10188 (2008).
- [34] J. U. White, “Long optical paths of large aperture,” *J. Opt. Soc. Am.* **32**, 285–288 (1942).
- [35] D. R. Herriott and H. J. Schulte, “Folded optical delay lines,” *Appl. Opt.* **4**, 883–889 (1965).
- [36] J. U. White, “Very long optical paths in air,” *J. Opt. Soc. Am.* **66**, 411–416 (1976).
- [37] D. S. Venables, T. Gherman, J. Orphal, J. C. Wenger, and A. A. Ruth, “High sensitivity in situ monitoring of NO<sub>3</sub> in an atmospheric simulation chamber using incoherent broadband cavity-enhanced absorption spectroscopy,” *Environ. Sci. Technol.* **40**, 6758–6763 (2006).

- [38] J. M. Langridge, S. M. Ball, and R. L. Jones, “A compact broadband cavity enhanced absorption spectrometer for detection of atmospheric NO<sub>2</sub> using light emitting diodes,” *Analyst* **131**, 916–922 (2006).
- [39] G. Schmidl, W. Paa, W. Triebel, S. Schippel, and H. Heyer, “Spectrally resolved cavity ring down measurement of high reflectivity mirrors using a supercontinuum laser source,” *Appl. Opt.* **48**, 6754–6759 (2009).
- [40] K. Stelmaszczyk, M. Fechner, P. Rohwetter, M. Queißer, A. Czyżewski, T. Stacewicz, and L. Wöste, “Towards supercontinuum cavity ring-down spectroscopy,” *Appl. Phys. B* **94**, 369–373 (2009).
- [41] R. A. Washenfelder, A. O. Langford, H. Fuchs, and S. S. Brown, “Measurement of glyoxal using an incoherent broadband cavity enhanced absorption spectrometer,” *Atmos. Chem. Phys.* **8**, 7779–7793 (2008).
- [42] N. Jordan, C. Z. Ye, S. Ghosh, R. A. Washenfelder, S. S. Brown, and H. D. Osthoff, “A broadband cavity-enhanced spectrometer for atmospheric trace gas measurements and Rayleigh scattering cross sections in the cyan region (470 – 540 nm),” *Atmos. Meas. Tech.* **12**, 1277–1293 (2019).
- [43] A. A. Ruth, J. Orphal, and S. E. Fiedler, “Fourier-transform cavity-enhanced absorption spectroscopy using an incoherent broad-band light source,” *Appl. Opt.* **46**, 3611–3616 (2007).
- [44] W. Denzer, G. Hancock, M. Islam, C. E. Langley, R. Peverall, G. A. D. Ritchie, and D. Taylor, “Trace species detection in the near infrared using Fourier transform broadband cavity enhanced absorption spectroscopy: Initial studies on potential breath analytes,” *Analyst* **136**, 801–806 (2011).
- [45] M. Schnippering, P. R. Unwin, J. Hult, T. Laurila, C. F. Kaminski, J. M. Langridge, R. L. Jones, M. Mazurenka, and S. R. Mackenzie, “Evanescent wave broadband cavity enhanced absorption spectroscopy using supercontinuum radiation: A new probe of electrochemical processes,” *Electrochem. Commun.* **10**, 1827–1830 (2008).

- [46] F. Brech and L. Cross, "Optical microemission stimulated by a ruby MASER," *Appl. Spectrosc.* **16**, 59 (1962).
- [47] T. H. Maiman, "Stimulated optical radiation in ruby," *Nature* **187**, 493–494 (1960).
- [48] E. K. Damon and R. G. Tomlinson, "Observation of ionization of gases by a ruby laser," *Appl. Opt.* **2**, 546–547 (1963).
- [49] E. B. Belyaev, A. P. Godlevskii, and Y. D. Kopytin, "Laser spectrochemical analysis of aerosols," *Sov. J. Quant. Electro.* **8**, 1459–1463 (1978).
- [50] T. R. Loree and L. J. Radziemski, "Laser-induced breakdown spectroscopy: Time-integrated applications," *Plasma Chem. Plasma Process.* **1**, 271–279 (1981).
- [51] D. A. Cremers and L. J. Radziemski, "Direct detection of beryllium on filters using the laser spark." *Appl. Spectrosc.* **39**, 57–63 (1985).
- [52] D. A. Cremers, "The analysis of metals at a distance using laser-induced breakdown spectroscopy," *Appl. Spectrosc.* **41**, 572–579 (1987).
- [53] K. J. Grant, G. L. Paul, and J. A. O'Neill, "Quantitative elemental analysis of iron ore by laser-induced breakdown spectroscopy," *Appl. Spectrosc.* **45**, 701–705 (1991).
- [54] D. A. Cremers, L. J. Radziemski, and T. R. Loree, "Spectrochemical analysis of liquids using the laser spark," *Appl. Spectrosc.* **38**, 721–729 (1984).
- [55] L. J. Radziemski, D. A. Cremers, and T. R. Loree, "Detection of beryllium by laser-induced-breakdown spectroscopy," *Spectrochim. Acta B* **38**, 349–355 (1983).
- [56] J. Stricker and J. Parker, "Experimental investigation of electrical breakdown in nitrogen and oxygen induced by focused laser radiation at 1.064  $\mu\text{m}$ ," *J. Appl. Phys.* **53**, 851–855 (1982).

- [57] P. K. Kennedy, S. A. Boppart, D. X. Hammer, B. A. Rockwell, G. D. Noojin, and W. P. Roach, “A first-order model for computation of laser-induced breakdown thresholds in ocular and aqueous media: Part II – Comparison to experiment,” *IEEE J. Quant. Elec.* **31**, 2250–2257 (1995).
- [58] A. Semerok, B. Sallé, J.-F. Wagner, and G. Petite, “Femtosecond, picosecond, and nanosecond laser microablation: Laser plasma and crater investigation,” *Laser Part. Beams* **20**, 67–72 (2002).
- [59] Y.-L. Chen, J. W. L. Lewis, and C. Parigger, “Spatial and temporal profiles of pulsed laser-induced air plasma emissions,” *J. Quant. Spectrosc. Radiat. Trans.* **67**, 91–103 (2000).
- [60] L. J. Radziemski, T. R. Loree, D. A. Cremers, and N. M. Hoffman, “Time-resolved laser-induced breakdown spectrometry of aerosols,” *Anal. Chem.* **55**, 1246–1252 (1983).
- [61] H. P. Graf and F. K. Kneubühl, “Temporal and spatial evolution of the laser-induced plasma in methane,” *Appl. Phys. B* **31**, 53–61 (1983).
- [62] N. Kawahara, J. L. Beduneau, T. Nakayama, E. Tomita, and Y. Ikeda, “Spatially, temporally, and spectrally resolved measurement of laser-induced plasma in air,” *Appl. Phys. B* **86**, 605–614 (2007).
- [63] I. B. Gornushkin, L. A. King, B. W. Smith, N. Omenetto, and J. D. Winefordner, “Line broadening mechanisms in the low pressure laser-induced plasma,” *Spectrochim. Acta B* **54**, 1207–1217 (1999).
- [64] B. C. Castle, K. Talabardon, B. W. Smith, and J. D. Winefordner, “Variables influencing the precision of laser-induced breakdown spectroscopy measurements,” *Appl. Spectrosc.* **52**, 649–657 (1998).
- [65] Ş. Yalçın, D. Crosley, G. Smith, and G. Faris, “Influence of ambient conditions on the laser air spark,” *Appl. Phys. B* **68**, 121–130 (1999).

- [66] V. Hohreiter, A. J. Ball, and D. W. Hahn, “Effects of aerosols and laser cavity seeding on spectral and temporal stability of laser-induced plasmas: Applications to LIBS,” *J. Anal. At. Spectrom.* **19**, 1289–1294 (2004).
- [67] A. E. Siegman, *Lasers* (University Science Books, California, USA, 1990).
- [68] N. Hodgson and H. Weber, *Optical Resonators: Fundamentals, Advanced Concepts and Applications* (Springer, London, UK, 1997).
- [69] A. Yariv and P. Yeh, *Photonics: Optical Electronics in Modern Communications* (Oxford University Press, New York, USA, 1997).
- [70] S. Vaughan, T. Gherman, A. A. Ruth, and J. Orphal, “Incoherent broadband cavity-enhanced absorption spectroscopy of the marine boundary layer species I<sub>2</sub>, IO and OIO,” *Phys. Chem. Chem. Phys.* **10**, 4471–4477 (2008).
- [71] S. Dixneuf, A. A. Ruth, S. Vaughan, R. M. Varma, and J. Orphal, “The time dependence of molecular iodine emission from *Laminaria digitata*,” *Atmos. Chem. Phys.* **9**, 823–829 (2009).
- [72] A. Walsh, D. Zhao, and H. Linnartz, “Cavity enhanced plasma self-absorption spectroscopy,” *Appl. Phys. Lett.* **101**, 091111 (2012).
- [73] P. S. Johnston and K. K. Lehmann, “Cavity enhanced absorption spectroscopy using a broadband prism cavity and a supercontinuum source,” *Opt. Express* **16**, 15013–15023 (2008).
- [74] M. Schnippering, S. R. T. Neil, S. R. Mackenzie, and P. R. Unwin, “Evanescent wave cavity-based spectroscopic techniques as probes of interfacial processes,” *Chem. Soc. Rev.* **40**, 207–220 (2011).
- [75] C. Petermann and P. Fischer, “Actively coupled cavity ringdown spectroscopy with low-power broadband sources,” *Opt. Express* **19**, 10164–10173 (2011).
- [76] A. L. Gomez, R. F. Renzi, J. A. Fruetel, and R. P. Bambha, “Integrated fiber optic incoherent broadband cavity enhanced absorption spectroscopy



- detector for near-IR absorption measurements of nanoliter samples,” *Appl. Opt.* **51**, 2532–2540 (2012).
- [77] Y. Yao, J. Yao, V. K. Narasimhan, Z. Ruan, C. Xie, S. Fan, and Y. Cui, “Broadband light management using low-Q whispering gallery modes in spherical nanoshells,” *Nat. Commun.* **3**, 664 (2012).
- [78] J. C. Galas, C. Peroz, Q. Kou, and Y. Chen, “Microfluidic dye laser intracavity absorption,” *Appl. Phys. Lett.* **89**, 224101 (2006).
- [79] N. Hodgson, B. Ozygus, F. Schabert, and H. Weber, “Degenerated confocal resonator,” *Appl. Opt.* **32**, 3190–3200 (1993).
- [80] S. E. Fiedler, A. Hese, and U. Heitmann, “Influence of the cavity parameters on the output intensity in incoherent broadband cavity-enhanced absorption spectroscopy,” *Rev. Sci. Instrum.* **78**, 073104 (2007).
- [81] V. M. Baev, T. Latz, and P. E. Toschek, “Laser intracavity absorption spectroscopy,” *Appl. Phys. B* **69**, 171–202 (1999).
- [82] A. J. Walsh, D. Zhao, and H. Linnartz, “Note: Cavity enhanced self-absorption spectroscopy: A new diagnostic tool for light emitting matter,” *Rev. Sci. Instrum.* **84**, 026108 (2013).
- [83] A. Borghese and S. S. Merola, “Time-resolved spectral and spatial description of laser-induced breakdown in air as a pulsed, bright, and broadband ultraviolet-visible light source.” *Appl. Opt.* **37**, 3977–3983 (1998).
- [84] S. S. Merola, G. Gambi, C. Allouis, F. Beretta, A. Borghese, and A. D’Alessio, “Analysis of exhausts emitted by i.c. engines and stationary burners, by means of u.v. extinction and fluorescence spectroscopy,” *Chemosphere* **42**, 827–834 (2001).
- [85] M. Kurz, A. D’Anna, A. D’Alessio, S. S. Merola, and A. Borghese, “UV-broadband light scattering measurements during metallic particle formation in a combustion-like environment,” *Part. Part. Syst. Charact.* **16**, 77–84 (1999).

- [86] C. Lazzari, M. De Rosa, S. Rastelli, A. Ciucci, V. Palleschi, and A. Salvetti, “Detection of mercury in air by time-resolved laser-induced breakdown spectroscopy technique,” *Laser Part. Beams* **12**, 525–530 (1994).
- [87] E. D. McNaghten, A. M. Parkes, B. C. Griffiths, A. I. Whitehouse, and S. Palanco, “Detection of trace concentrations of helium and argon in gas mixtures by laser-induced breakdown spectroscopy,” *Spectrochim. Acta B* **64**, 1111–1118 (2009).
- [88] J. Xie, B. A. Paldus, E. H. Wahl, J. Martin, T. G. Owano, C. H. Kruger, J. S. Harris, and R. N. Zare, “Near-infrared cavity ringdown spectroscopy of water vapor in an atmospheric flame,” *Chem. Phys. Lett.* **284**, 387–395 (1998).
- [89] S. Spuler and M. Linne, “Numerical analysis of beam propagation in pulsed cavity ring-down spectroscopy,” *Appl. Opt.* **41**, 2858–2868 (2002).
- [90] R. Evertsen, J. A. Van Oijen, R. T. E. Hermanns, L. P. H. De Goey, and J. J. Ter Meulen, “Measurements of absolute concentrations of CH in a premixed atmospheric flat flame by cavity ring-down spectroscopy,” *Combust. Flame* **132**, 34–42 (2003).
- [91] A. Dragomir, J. G. McInerney, D. N. Nikogosyan, and A. A. Ruth, “Two-photon absorption coefficients of several liquids at 264 nm,” *IEEE J. Quantum Electron.* **38**, 31–36 (2002).
- [92] A. Dragomir, J. G. McInerney, and D. N. Nikogosyan, “Femtosecond measurements of two-photon absorption coefficients at  $\lambda = 264$  nm in glasses, crystals, and liquids,” *Appl. Opt.* **41**, 4365–4376 (2002).
- [93] M. Czerny and A. F. Turner, “Über den Astigmatismus bei Spiegelspektrometern,” *Z. Physik* **61**, 792–797 (1930).
- [94] A. A. Istratov and O. F. Vyvenko, “Exponential analysis in physical phenomena,” *Rev. Sci. Instrum.* **70**, 1233–1257 (1999).

- [95] P. Pořízka, B. Klessen, J. Kaiser, I. Gornushkin, U. Panne, and J. Riedel, “High repetition rate laser-induced breakdown spectroscopy using acousto-optically gated detection,” *Rev. Sci. Instrum.* **85**, 073104 (2014).
- [96] A. Gold and H. B. Bebb, “Theory of multiphoton ionization,” *Phys. Rev. Lett.* **14**, 60–63 (1965).
- [97] N. Kroll and K. M. Watson, “Theoretical study of ionization of air by intense laser pulses,” *Phys. Rev. A* **5**, 1883–1905 (1972).
- [98] C. H. Chan, C. D. Moody, and W. B. McKnight, “Significant loss mechanisms in gas breakdown at 10.6  $\mu$ ,” *J. Appl. Phys.* **44**, 1179–1188 (1973).
- [99] F. V. Bunkin and A. M. Prokhorov, “Some features of the interaction between short laser radiation pulses and matter,” *Sov. Phys. JETP* **25**, 1072–1075 (1967).
- [100] I. K. Krasnyuk, P. P. Pashinin, and A. M. Prokhorov, “Investigation of breakdown in N<sub>2</sub> under the influence of a picosecond ruby-laser pulse,” *JETP Lett.* **9**, 354–356 (1969).
- [101] I. K. Krasnyuk, P. P. Pashinin, and A. M. Prokhorov, “Investigation of breakdown in argon and helium produced by a picosecond ruby laser light pulse,” *Sov. Phys. JETP* **31**, 860–861 (1970).
- [102] D. C. Smith and R. G. Meyerand Jr, in *Principles of Laser Plasmas*, G. Bekefi, ed. (John Wiley & Sons, New York, USA, 1976), chap. 11.
- [103] D. C. Smith and R. G. Meyerand Jr, in *Principles of Laser Plasmas*, G. Bekefi, ed. (John Wiley & Sons, New York, USA, 1976), chap. 11, p. 466.
- [104] J. B. Simeonsson and A. W. Miziolek, “Spectroscopic studies of laser-produced plasmas formed in CO and CO<sub>2</sub> using 193, 266, 355, 532 and 1064 nm laser radiation,” *Appl. Phys. B* **59**, 1–9 (1994).

- [105] J. P. Davis, A. L. Smith, C. Giranda, and M. Squicciarini, “Laser-induced plasma formation in Xe, Ar, N<sub>2</sub>, and O<sub>2</sub> at the first four Nd:YAG harmonics,” *Appl. Opt.* **30**, 4358–4364 (1991).
- [106] R. A. Armstrong, R. A. Lucht, and W. T. Rawlins, “Spectroscopic investigation of laser-initiated low-pressure plasmas in atmospheric gases,” *Appl. Opt.* **22**, 1573–1577 (1983).
- [107] R. Tambay and R. K. Thareja, “Laser-induced breakdown studies of laboratory air at 0.266, 0.355, 0.532, and 1.06  $\mu\text{m}$ ,” *J. Appl. Phys.* **70**, 2890–2892 (1991).
- [108] S. S. Harilal, B. E. Brumfield, and M. C. Phillips, “Lifecycle of laser-produced air sparks,” *Phys. Plasmas* **22**, 063301 (2015).
- [109] D. W. Allan, “Statistics of atomic frequency standards,” *Proc. IEEE* **54**, 221–230 (1966).
- [110] P. Werle, R. Mücke, and F. Slemr, “The limits of signal averaging in atmospheric trace-gas monitoring by tunable diode-laser absorption spectroscopy (TDLAS),” *Appl. Phys. B* **57**, 131–139 (1993).
- [111] E. Heidecker, J. H. Schäfer, J. Uhlenbusch, and W. Viöl, “Time-resolved study of a laser-induced surface plasma by means of a beam-deflection technique,” *J. Appl. Phys.* **64**, 2291–2297 (1988).
- [112] R. Navarro-González and M. Villagrán-Muniz, “Effect of beam waist on shock properties of laser-induced plasmas in air by the photoacoustic probe beam deflection method,” *Anal. Sci.* **17**, s118–121 (2001).
- [113] M. Villagrán-Muniz, H. Sobral, and R. Navarro-González, “Shock and thermal wave study of laser-induced plasmas in air by the probe beam deflection technique,” *Meas. Sci. Technol.* **14**, 614–618 (2003).
- [114] J. A. Aguilera and C. Aragón, “Characterization of laser-induced plasma during its expansion in air by optical emission spectroscopy: Observation

- of strong explosion self-similar behavior,” *Spectrochim. Acta B* **97**, 86–93 (2014).
- [115] M. Sabsabi and P. Cielo, “Quantitative analysis of aluminum alloys by laser-induced breakdown spectroscopy and plasma characterization,” *Appl. Spectrosc.* **49**, 499–507 (1995).
- [116] A. Kramida, Yu. Ralchenko, J. Reader, and NIST ASD Team, NIST Atomic Spectra Database (ver. 5.6.1), [Online]. Available: <https://physics.nist.gov/asd>. National Institute of Standards and Technology, Gaithersburg, MD. (2018).
- [117] L. St-Onge, M. Sabsabi, and P. Cielo, “Quantitative analysis of additives in solid zinc alloys by laser-induced plasma spectrometry,” *J. Anal. At. Spectrom.* **12**, 997–1004 (1997).
- [118] B. P. Keary and A. A. Ruth, “Time- and intensity-dependent broadband cavity-enhanced absorption spectroscopy with pulsed intra-cavity laser-induced plasmas,” *Opt. Express* **27**, 36864–36874 (2019).
- [119] D. Huppert, J. Jortner, and P. M. Rentzepis, “Laser excited emission spectroscopy of azulene in the gas phase,” *J. Chem. Phys.* **56**, 4826–4833 (1972).
- [120] Y. Hirata and E. C. Lim, “Radiationless transitions in azulene: Evidence for the ultrafast  $S_2 \rightarrow S_0$  internal conversion,” *J. Chem. Phys.* **69**, 3292–3296 (1978).
- [121] G. D. Gillispie and E. C. Lim, “Vibrational analysis of the  $S_2 \rightarrow S_1$  fluorescence of azulene in a naphthalene mixed crystal at 4.2 K,” *J. Chem. Phys.* **68**, 4578–4586 (1978).
- [122] M. Beer and H. C. Longuet-Higgins, “Anomalous light emission of azulene,” *J. Chem. Phys.* **23**, 1390–1391 (1955).
- [123] G. Viswanath and M. Kasha, “Confirmation of the anomalous fluorescence of azulene,” *J. Chem. Phys.* **24**, 574–577 (1956).

- [124] G. R. Hunt and I. G. Ross, "Spectrum of azulene. Part II. The 7000-A and 3500-A absorption systems," *J. Mol. Spectrosc.* **9**, 50–78 (1962).
- [125] A. Amirav and J. Jortner, "Spectroscopic manifestation of intramolecular relaxation of azulene in supersonic jets," *J. Chem. Phys.* **81**, 4200–4205 (1984).
- [126] A. A. Ruth, E. -K. Kim, and A. Hese, "The  $S_0 \rightarrow S_1$  cavity ring-down absorption spectrum of jet-cooled azulene: Dependence of internal conversion on the excess energy," *Phys. Chem. Chem. Phys.* **1**, 5121–5128 (1999).
- [127] S. E. Fiedler, G. Hoheisel, A. A. Ruth, and A. Hese, "Incoherent broadband cavity-enhanced absorption spectroscopy of azulene in a supersonic jet," *Chem. Phys. Lett.* **382**, 447–453 (2003).
- [128] A. Bauder and Hs. H. Günthard, "Dampfdruck von Azulen," *Helv. Chim. Acta* **45**, 1698–1702 (1962).
- [129] S. Hassoon, D. L. Snavely, and I. Oref, "Two-photon photodissociation of gaseous azulene at 325 nm," *J. Chem. Phys.* **97**, 9081–9085 (1992).
- [130] M. Triki, P. Cermak, G. Méjean, and D. Romanini, "Cavity-enhanced absorption spectroscopy with a red LED source for  $\text{NO}_x$  trace analysis," *Appl. Phys. B* **91**, 195–201 (2008).
- [131] G. Mallocci, G. Mulas, and C. Joblin, "Electronic absorption spectra of PAHs up to vacuum UV," *Astron. Astrophys.* **426**, 105–117 (2004).
- [132] G. Mallocci, G. Mulas, G. Cappellini, V. Fiorentini, and I. Porceddu, "Theoretical electron affinities of PAHs and electronic absorption spectra of their mono-anions," *Astron. Astrophys.* **432**, 585–594 (2005).
- [133] G. Mallocci, C. Joblin, and G. Mulas, "On-line database of the spectral properties of polycyclic aromatic hydrocarbons," *Chem. Phys.* **332**, 353–359 (2007).
- [134] T. Nozoe, S. Seto, S. Matsumura, and Y. Murase, "The synthesis of azulene derivatives from troponoids," *Bull. Chem. Soc. Jpn.* **35**, 1179–1188 (1962).

- [135] H. Keller-Rudek, G. K. Moortgat, R. Sander, and R. Sørensen, “The MPI-Mainz UV/VIS spectral atlas of gaseous molecules of atmospheric interest,” *Earth Syst. Sci. Data* **5**, 365–373 (2013).
- [136] V. Hohreiter, J. E. Carranza, and D. W. Hahn, “Temporal analysis of laser-induced plasma properties as related to laser-induced breakdown spectroscopy,” *Spectrochim. Acta B* **59**, 327–333 (2004).
- [137] H. Kogelnik, “Imaging of optical modes – Resonators with internal lenses,” *Bell Syst. Tech. J.* **44**, 455–494 (1965).
- [138] A. G. Fox and T. Li, “Resonant modes in a maser interferometer,” *Bell Syst. Tech. J.* **40**, 453–488 (1961).
- [139] A. G. Fox and T. Li, “Modes in a maser interferometer with curved and tilted mirrors,” *Proc. IEEE* **51**, 80–89 (1963).
- [140] LAS-CAD GmbH, “Lascad,” <https://www.las-cad.com>. Accessed: 06-10-2019.
- [141] B. Le Drogoff, J. Margot, F. Vidal, S. Laville, M. Chaker, M. Sabsabi, T. W. Johnston, and O. Barthélémy, “Influence of the laser pulse duration on laser-produced plasma properties,” *Plasma Sources Sci. Technol.* **13**, 223–230 (2004).
- [142] A. Elhassan, A. Giakoumaki, D. Anglos, G. M. Ingo, L. Robbiola, and M. A. Harith, “Nanosecond and femtosecond laser induced breakdown spectroscopic analysis of bronze alloys,” *Spectrochim. Acta B* **63**, 504–511 (2008).